공학박사학위논문

The influences of pulse and pulse-reverse electrodeposition on the properties of Cu thin films and superfilling for the fabrication of Cu interconnection

펄스 및 펄스-리벌스 전해 도금이 구리 박막 및 수퍼필링 특성에 미치는 영향

2013년   2월

서울대학교 대학원

화학생물공학부

김 명 준

The influences of pulse and pulse-reverse electrodeposition on the properties of Cu thin films and superfilling for the fabrication of Cu interconnection

펄스 및 펄스-리벌스 전해 도금이 구리 박막 및 수퍼필링 특성에 미치는 영향

지도교수 김 재 정

이 논문을 공학박사 학위논문으로 제출함
2012 년 11 월

서울대학교 대학원
화학생물공학부
김 명 준

김명준의 공학박사 학위논문을 인준함
2012 년 12 월

위 원 장 _____

부위원장 _____

위   원 _____

위   원 _____

위   원 _____

Abstract

The scale-down of Cu interconnection raises the issues such as the reduction of interconnection property and the difficulty in superfilling using electrodeposition. In the aspect of the interconnection property, the electrical resistivity and the electromigration resistance are the major concerns. In this study, it was attempted to improve the properties of Cu by means of pulse and pulse-reverse electrodeposition. For the purpose of enhancing the superfilling performance, the pulse-reverse electrodeposition was employed.

Pulse electrodeposition consisted of on-time during which Cu reduction takes place and off-time where open circuit potential is applied. The peak potential and the lengths of on- and off-times were the important variables determining the film properties. In the results of experiments with varying the off-time, it was confirmed that the grain growth took place during the off-time, resulting in the enhancement of crystallinity and the reduction of resistivity as well. This grain growth seemed to be related to the differences of energies originated from the crystal orientation and grain size. With the enough off-time, Cu film deposited by pulse electrodeposition exhibited 68% higher Cu (111) peak intensity and 22% lower resistivity as compared to constant potential

deposition when the film thickness was 260 nm including 60 nm Cu seed layer.

However, when the organic additives generally used for Cu superfilling, the grain

growth during the off-time was significantly retarded because the organic additives,

which strongly adsorbed on Cu surface, changed the energy differences related to the

orientation and grain size. Therefore, it was decided to additionally apply the anodic

step to pulse electrodeposition, i.e. pulse-reverse electrodeposition, in order to further

improve the properties of Cu films.

Pulse-reverse electrodeposition was performed without and with organic additives to

clarify the impacts of anodic step and organic additives on the film properties. From

the variation in the film property according to the anodic conditions in the absence of

organic additives, it was observed that the selective dissolution took place, originated

from the energy differences related to the orientation and grain size. The selectivity of

dissolution depended on the anodic potential which determined the rate of change in

the film properties. That is, the application of more positive anodic potential reduced

the selectivity, and it slowly increased the grain size and surface roughness. Regarding

the electrical resistivity, the impacts of surface roughness and grain size competed with

each other, and it resulted in the optimum anodic charge showing the lowest resistivity.

As compared to the pulse electrodeposition, pulse-reverse electrodeposition reduced

9% of resistivity in the absence of additives. On the contrary, when the organic additives used for Cu superfilling are introduced, the selectivity of dissolution was determined by the species of the adsorbates. It was found that Cu covered by SPS was much easily dissolved compared to that covered by PEG-Cl$^-$. In this case, the resistivity was found to be strongly determined by the surface roughness, which also exhibited the optimum point at the relatively low dissolution ratio. Pulse-reverse electrodeposition in the presence of organic additives also showed the advantage on the electrical resistivity, which reduced 14% of resistivity compared to the pulse electrodeposition. Therefore, it can be concluded that the pulse-reverse electrodeposition has the merit in the aspect of electrical conductivity.

Superfilling performance was strongly determined by the adsorption of organic additives and their accumulation at the trench bottom produced by the area reduction. Prior to applying the pulse-reverse electrodeposition to superfilling, the impact of anodic step on the competitive adsorption between SPS and PEG-Cl$^-$ was investigated. As the results, it was clarified that the anodic step accelerated the displacement of preadsorbed PEG-Cl$^-$ by SPS, and the extent of displacement was increased with longer reverse time and more positive anodic potential. This acceleration of displacement has the potential to affect the superfilling, therefore, superfilling

performance was assessed with various anodic conditions. As compared to the gap-filling result of constant potential deposition, the pulse-reverse electrodeposition exhibited better bottom-up performance at the trench with 55 nm of width and 300 nm of depth. At the corner of low-aspect-ratio trench, the rapid growth of Cu was observed with pulse-reverse electrodeposition, implying more accumulation of SPS at the corner. These results were understood by the acceleration of displacement with the anodic step.

Considering the improvement of film properties as well as the superfilling performance, the modification of potential waveform, i.e. pulse and pulse-reverse electrodeposition, can be a candidate for resolving the current issues. This enables us to achieve Cu interconnection in the electronic devices with high speed and superior reliability.

Keywords: Cu, interconnection, pulse electrodeposition, pulse-reverse electrodeposition, thin film property, superfilling

Student number: 2007-21174

Content

List of Tables

List of Figures

CHAPTER I

Introduction

1-1. Cu interconnection and Damascene process

Cu has been widely used as the material for metal interconnection in the electronic devices, replacing the Al interconnection.[1] In order to improve the operation speed, increase in the chip integrity, and reduce the production cost, the size of device continuously shrinks. This implies that the dimensions of both transistor and conductor in the device are reduced.[2-4] Until the late 1990's, the total speed of the microprocessor was determined by the signal delay at the gate of transistor related to the time from applying the input signal to transistor and obtaining the output signal.[5] When the gate delay is dominated the total speed of devices, the speed of signal transduction through Al interconnection is enough to maintain the total performance. However, the resistance-capacitance delay, related to the electrical resistivity of interconnection and the capacitance of dielectrics, became more important compared to gate delay as the width of metal interconnection was reduced to below 250 nm.[5] In addition to that, the interconnection has been also lengthened with the increase in the number of metal level.

That is, the total speed of microprocessors was strongly determined by the electrical property of metal interconnection. In accordance, it was decided to replace Al to Cu, which exhibits 1.7 times higher electrical conductivity of bulk (Al: 3.5×10^7 S/m, Cu: 5.96×10^7 S/m at 20°C). In addition, the resistance against the failure formation originated from the electromigration was also improved when Cu is employed as the interconnection material.[6,7] Nowadays, the microprocessor consisted of more than ten layers of Cu interconnection, and the flash memory also contained more than two layers (Fig. 1.1).[4]

The strategy for achieving high speed is to stack the metal layers with the appropriate design. In the case of Al, this was obtained by the dry etch of Al thin film and the filling of dielectric between patterned Al as shown in Fig. 1.2. After the dielectric deposition, the planarization step was applied to expose Al in sublayer to form the metal contact. The iteration of this step enabled to get multi-level Al interconnection. However, when this method is adopted to the fabrication of Cu interconnection, the dry etch step could not be applied because the residue of Cu-Cl complex caused a problem in the following steps. From this issue, Damascene process was determined to be introduced which consisted of the deposition and patterning of dielectric, the deposition of diffusion barrier and Cu seed layers, the gap-filling of Cu in various

trenches and vias, and chemical mechanical planarization of overdeposited Cu.[1,9] The

schematic diagram of Damascene process for fabricating Cu interconnection is

described in Fig. 1.3. The gap-filling of Cu in the pattern was newly adopted, and it

brought Cu electrodeposition into the one of steps for the metallization of electronic

devices.
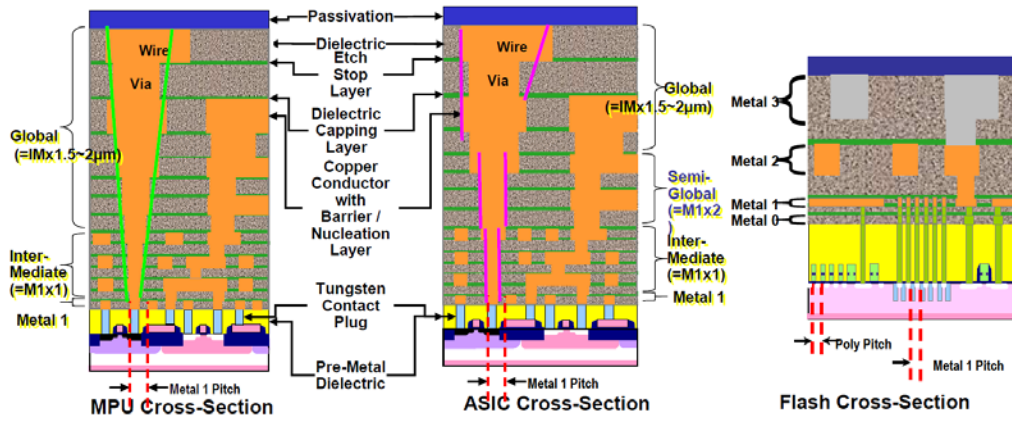
Fig. 1.1. The representative cross-sectional images of microprocessor (left), application-specific integrated circuit (middle), and flash memory (right) from Ref. 4.

(a) Diffusion barrier deposition

(b) Al sputtering

(c) Patterning (dry etch)

(d) Dielectric gap fill
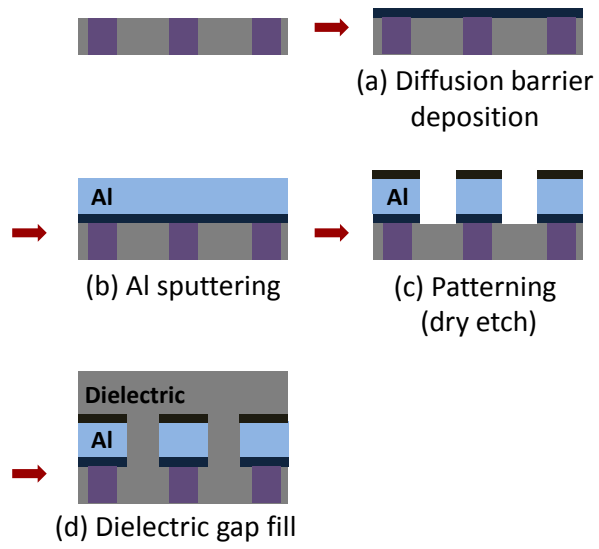
Fig. 1.2. The schematic diagram of the fabrication for Al interconnection.

Dielectric

(a) Dielectric deposition

(b) Patterning

(c) Barrier and Cu seed layer deposition

Cu

(d) Cu electrodeposition

(e) Chemical mechanical planarization
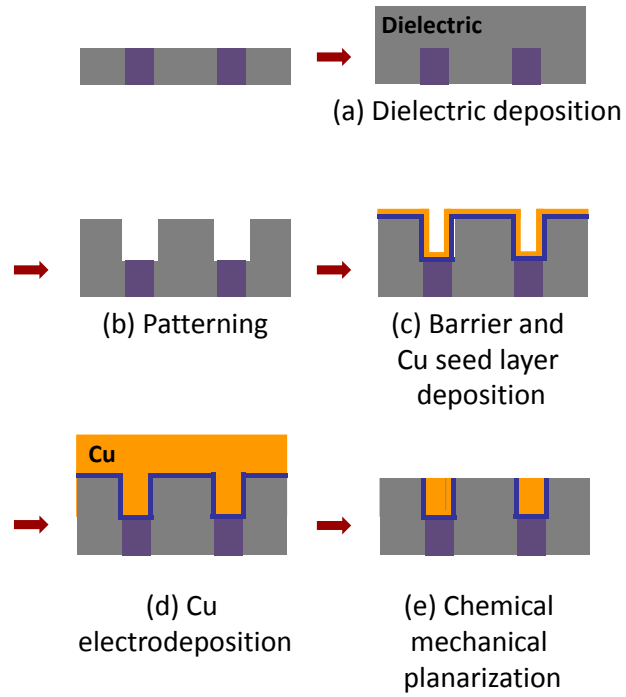
Fig. 1.3. Damascene process for the fabrication of Cu interconnection.

1-2. Cu electrodeposition and superfilling

The deposition of Cu was enabled by means of physical vapor deposition (PVD), chemical vapor deposition (CVD), atomic layer deposition (ALD), electrodeposition, and electroless deposition. Among these methods, electrodeposition was superior because the electrodeposition process is cheap and fast, forming Cu films with excellent properties. Additionally, it is important to note that the most significant advantage is feasible to obtain the defect-free filling at the patterns.

Electrodeposition is the one of metal or metal oxide plating techniques, using the externally supplied electrons to reduce the metal ions in the electrolyte. The system of electrodeposition consisted of the electrolyte, the electrodes, and the external power supply as described in Fig. 1.4. In the three-electrode system, the working electrode (i.e. cathode), the counter electrode (i.e. anode), and the reference electrode are employed, and the desired material is deposited on the surface of working electrode. The oxidation reaction with identical amount of reduction reaction on the cathode surface takes place at the counter electrode. The electrolyte is usually composed of the metal ions, supporting electrolyte reducing the solution resistance, and the organic additives adsorbing on the metal surface and affecting the film properties as well as the evolution

7

of deposit profile. In the Cu electrodeposition, various electrolytes have been employed for many applications, and the representative electrolytes are listed up in Table 1.1 Among them, the combination of Cu sulfate ($CuSO_4$) and sulfuric acid (H_2SO_4) has been the most widely used as the basic electrolytes.

As mentioned above, the patterned substrates should be filled with Cu by electrodeposition, therefore, the additional technique is needed to control the local deposition rate with considering the geometric effect of trenches or vias. The representative profiles of Cu deposit at the trench are shown in Fig. 1.5. The deposition at the trench could be separated into three profiles; (i) subconformal, (ii) conformal, and (iii) superconformal.[1] The subconformal profile is represented by the void formation inside the trench, which resulted from the concentrated deposition of Cu at the top corner of the trench. This is usually obtained under the mass-transport limited condition of Cu ions. The conformal deposition means the constant electrodeposition rate regardless of the position in the trench. The seam is an inevitable result of conformal deposition. The superconformal deposition, which is also called superfilling and bottom-up filling, is represented by the formation of the bumps at the top of deposits without any voids or seams inside the trench. It can be achieved by the local enhancement of deposition rate only at the bottom of trench. Since the formation of

seam or void inside the interconnection results in the increase in the electrical resistivity and the reduction in electromigration resistance, the superfilling of Cu without defect formation is necessary to fabricate high speed and reliable interconnection.

The superfilling of Cu is achieved by the addition of organic additives which adsorb on the Cu surface and affect the deposition rate as well as the film morphology.[10-15] The organic additives can be categorized into the accelerator and suppressor based on the changes in the deposition rate. The accelerators, which usually contains disulfide bonds (-S-S-) or mercapto functional groups (-S-H), enhance the deposition rate.[16-24] The representative accelerators are listed in Table. 1.2. The rate determining step of Cu electrodeposition is the reduction of Cu^{2+} to Cu^{+}. The accelerators make a complex with Cu^{2+} forming Cu^{+}, and it results in the enhancement of deposition rate. On the contrary, the suppressors reduce the electrodeposition rate, and the representative suppressor is the combination of polyether and halide ion.[25-30] In addition to that, the leveler, which contains nitrogen atoms and strongly adsorbs on the Cu surface, also suppressing the deposition of Cu. The various suppressors are shown in Table 1.3. The representative combination of accelerator and suppressor for Cu superfilling is polyethylene glycol (PEG), chloride ion (Cl^{-}), and bis(3-sulfopropyl) disulfide (SPS).

The superfilling of Cu with PEG-Cl⁻-SPS has been explained by curvature enhanced accelerator coverage (CEAC) model proposed by T. P. Moffat and D. Josell.[31-33] The schematic diagram of Cu superfilling in the trench is exhibited in the Fig. 1.6. At first, when the substrate with the trench is dip into the electrolyte, the relatively large amount of suppressor (PEG-Cl⁻) rapidly adsorbs on the surface. Since the concentration of suppressor (i.e. surfactant) is considerably high at the interface between the electrolyte and atmosphere, the suppressor adsorption is dominant than the accelerator when the substrate passes through this interface. After that, the displacement between preadsorbed PEG-Cl⁻ layer and SPS takes place, because the adsorption strength of accelerator is higher than that of suppressor and the application of negative potential reduces the stability of preadsorbed PEG-Cl⁻ layer. This displacement between suppressor and accelerator is easily confirmed by the chronoamperometry with the planar electrode, revealing that the current is increased as the deposition progressed.[34-36] The current behavior according to the cathodic potential is shown in Fig. 1.7. Above the sufficient concentration level of accelerator, it affects the deposition profile. As the electrodeposition progresses, the deposition area is significantly reduced at the bottom corner of the trench (i.e. negative surface curvature). The area reduction at the bottom results in the accumulation of accelerator, and it follows the local acceleration of

electrodeposition. This enables to achieve predominant growth of Cu at the bottom, which named this process bottom-up filling. After the gap-filling, the accumulated accelerator on the top of deposit continues to enhance the deposition rate, therefore, the convex profile (i.e. bump) is observed, which is considered as the significant evidence of Cu superfilling with the trench dimension below few hundred nanometers.

 CEAC model for Cu superfilling provides the accurate prediction of deposition profile evolution during the electrodeposition. It deals with the competitive adsorption between accelerator and suppressor and the accumulation of adsorbed accelerator according to the area reduction. The surface coverage change of adsorbed accelerator is described in the following equation,[33]

$$\frac{d\theta_{SPS}}{dt} = k_{ads}(1 - \theta_{SPS})C_{SPS} - k_{inc}(\theta_{SPS})^q - v\kappa\theta_{SPS} + D\frac{\partial^2\theta_{SPS}}{\partial S^2} \qquad (1.1)$$

where θ_{SPS} is the surface coverage of adsorbed SPS, k_{ads} is the rate constant of SPS adsorption, C_{SPS} is the bulk concentration of SPS, k_{inc} is the rate constant of SPS incorporation, v is the deposition rate which is normal to the surface, κ is the surface curvature, D is the diffusivity of adsorbed SPS along with the surface. The first term in right implies the adsorption of SPS, and it is related to aforementioned displacement

between preadsorbed PEG-Cl$^-$ layer and SPS. The second term means the deactivation

of adsorbed SPS through the incorporation, and q is experimentally determined. The

third term deals with the accumulation or deaccumulation of adsorbed accelerator

according to the surface curvature, which named this model "curvature enhanced

accelerator coverage". When the electrodeposition progresses on the surface with

negative curvature (i.e. bottom of trench), the adsorbed accelerator is accumulated by

the area reduction. Since the deposition rate is linearly dependent on the surface

coverage of accelerator, the accumulated accelerator at the bottom of trench implies the

local enhancement of Cu electrodeposition. The last term treats the diffusion of SPS

along with the surface. The surface diffusion of adsorbed accelerator also significantly

affects the superfilling performance because it is related to the maintenance of

accumulated accelerators by the area reduction. That is, the superfilling becomes more

difficult when the surface diffusion of accelerator is considerably fast because the

accumulated accelerators spread out through the diffusion along the surface. On the

basis of this equation, the dimensionless factor, $D/(wv_0)$ can characterize the

superfilling performance where w is the width of the trench and v_0 is the deposition

rate with the initial surface coverage of SPS.[33] The CEAC predictions according to this

dimensionless number are represented in Fig. 1.8 revealing that the superfilling can be

achieved with the lower dimensionless number. In the case of Cu superfilling, the

surface diffusion rate is relatively low compared to the deposition rate, therefore, the

surface diffusion is not significantly considered.

Table 1.1. The Representative Electrolytes for Cu Electrodeposition

Electrolytes	Sulfuric acid	Pyrophosphate	MSA	Cyanide
Basic components	$CuSO_4$, H_2SO_4	$CuSO_4$, $K_4P_2O_7$	$CuSO_4$, CH_3SO_3H (MSA)	CuCN, KCN
Application	Superfilling TSV filling	Seed repairing	Superfilling, TSV filling	Cu-Ag deposition

Table 1.2. The Representative Accelerators for Cu Electrodeposition
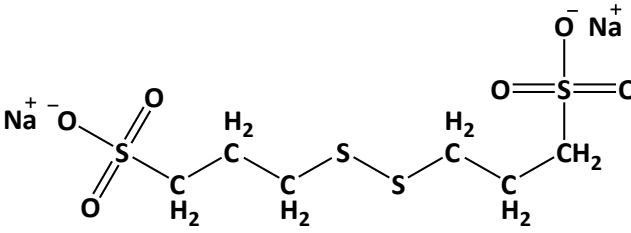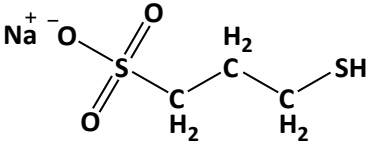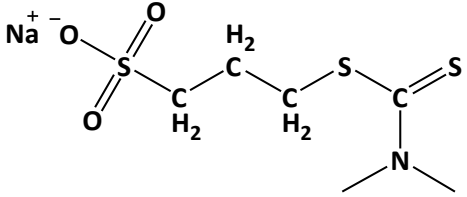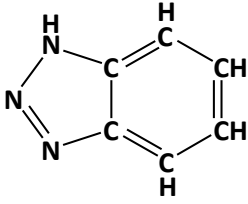
Representative accelerators	Molecular structure
Bis(3-sulfopropyl) disulfide (SPS)	
3-mercapto-1-propanesulfonic acid (MPSA)	
3-N,N-dimethylamonodithiocarbamoy -1-propanesulfonic acid (DPS)	

Table 1.3. The Representative Suppressors for Cu Electrodeposition

Representative suppressors	*Molecular structure*
Polyethylene glycol (PEG)	$HO-[CH_2-CH_2-O]_x-H$
Polypropylene glycol (PPG)	$HO-[CH_2-CH(CH_3)-O]_x-CH_3$
Polyethyleneimine (PEI)	$H_3C-[N(H)-CH_2-CH_2]_x-[N(CH_2CH_2NH_2)-CH_2-CH_2]_y-CH_3$
Thiourea	$H_2N-C(=S)-NH_2$
Benzotriazole (BTA)	benzotriazole

Fig. 1.4. The schematic diagram of Cu electrodeposition.
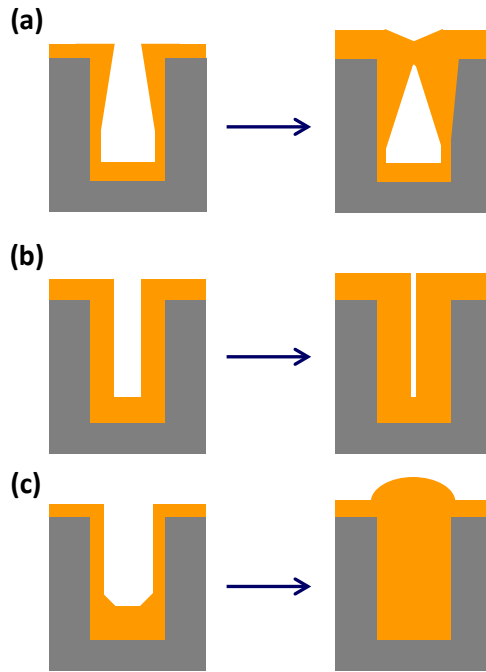
Fig. 1.5. The evolution of Cu deposits with (a) subconformal, (b) conformal, and (c) superconformal profiles.
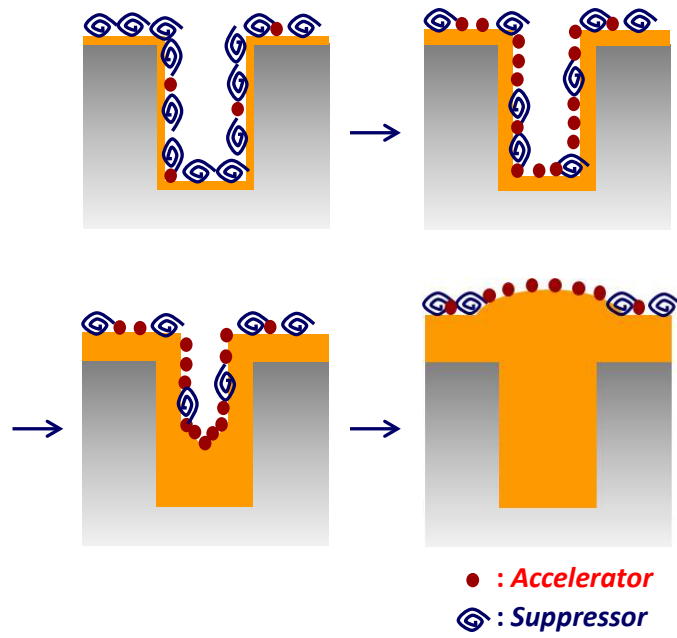
Fig. 1.6. The schematic diagram of Cu superfilling with the accelerator and suppressor

predicted with CEAC model.
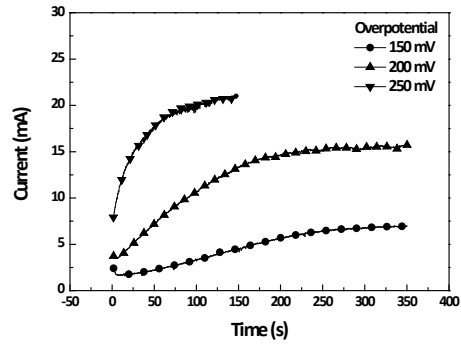
Fig. 1.7. The current behavior of Cu electrodeposition during the chronoamperometry

with various cathodic potential.
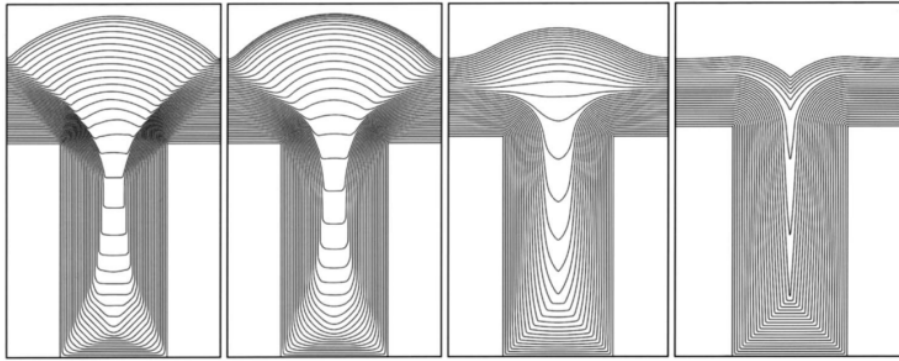
Fig. 1.8. The CEAC predictions with 0.01, 0.1, 1, and 10 of $D/(wv_0)$ values (left to right, Ref. 33)

1-3. Current issues and possible solutions

As addressed above, the size of electronic devices has been rapidly reduced, and the interconnection has also shrunk to improve the integrity and speed. In the interconnect part of international technology roadmap for semiconductor (ITRS), it is announced that the metal pitch in the microprocessor is now 32 nm, and it is expected that the dimension will be continuously reduced to 17 nm and 9 nm by the year 2017 and 2022.[4] Therefore, the issues related to the significant scaling of the interconnection are now addressed in ITRS, and they are listed up in Tables 1.4 and 1.5.[4] The challenges are classified into the near term (> 16 nm, before 2017) and long term (< 16 nm, after 2018). The five most critical challenges in the interconnection field with the dimension over 16 nm are (i) development of new material with the consideration of conductivity and dielectric permittivity, (ii) development of more manufacturable integration, (iii) improvement of reliability, (iv) three-dimensional fabrication of interconnect features, and (v) reduction of cost. In the dimension below 16 nm, 3D approach and the mitigation of the problems from the size effect are predicted. In the aspect of Cu electrodeposition, the main concerns are the improvement of interconnection properties and superfilling, such as (i) the electrical conductivity and (ii) the resistance against the

electromigration and (iii) the enhancement of superfilling performance. The details of these issues are explained in the followings.

As announced by ITRS in 2007, the electrical resistivity of Cu interconnection will be significantly increased as the line width is reduced to below few tens of nanometers (Fig. 1.9).[2] The electrical resistivity of metal is determined by the scattering probability of electrons when the electrons pass through the metal. When the dimension of metal is reduced below micrometer scale, the impacts of the additional electron scattering related to the grain boundary and surface roughness become more significant. That is, the electrical resistivity is determined by four kinds of electron scattering; (i) phonon, (ii) grain boundary, (iii) surface roughness, and (iv) impurities.[37-50] The phonon scattering is related to the intrinsic property of metal and it depends on the temperature. The reason why the bulk resistivity of Cu and Ag is different can be found from the phonon scattering. The scattering at the grain boundary was dealt by Mayadas-Shatzkes model, and it predicted the increasing tendency of the resistivity with the reduction of grain size.[37,38] The relationship of grain size and the resistivity is described by the following equations,

$$\frac{\rho_g}{\rho_b} = \left\{ 3 \left[\frac{1}{3} - \frac{1}{2}\alpha + \alpha^2 - \ln\left(1 + \frac{1}{\alpha}\right) \right] \right\}^{-1} \tag{1.2}$$

2 3

where $\alpha = \dfrac{\lambda}{d}\dfrac{R}{1-R}$ (1.3)

where ρ_g/ρ_b is the grain boundary contribution on the resistivity, λ is the mean free path of electrons in bulk at the room temperature, d is the average grain size, and R is the reflection coefficient of grain boundary. The contribution of surface roughness on the resistivity was investigated by S. M. Rossnagel and T. S. Kuan, and it was predicted that the impact of surface roughness becomes more significant in the size effect regime and the surface roughness of film tends to increase the resistivity.[39] The relationship between the roughness and the resistivity is shown in the following equation,[39]

$$\frac{\rho_s}{\rho_b} = 1 + 0.375(1-p)\frac{S\lambda}{t} \qquad\qquad\qquad (1.4)$$

where ρ_s/ρ_b is the contribution of surface roughness on the resistivity, p is the scattering parameter in the range from 0 to 1, S is the roughness factor, and t is the thickness of film. It tells us that the impact of the roughness is negligible when the film is relatively thick. The both contributions of grain size and surface roughness were also combined by T. S. Kuhn, and the following equation describes the result.[39]

$$\frac{\rho}{\rho_b} = 1 + 0.375(1-p)\frac{S\lambda}{t} + 1.5\frac{R}{1-R}\frac{\lambda}{d} \tag{1.5}$$

The impurities also provide the additional probability of electron scattering. In the case of electrodeposited films which showed the low level of impurity, the linear relationship between the resistivity and the concentration of impurity was reported.[51] However, the concentration of impurity is too low to dominate the film resistivity, therefore, it was usually treated as the minor factor compared to the grain size and surface roughness.

Electromigration of Cu caused by the electrical current stressing is the one of the most critical failure, determining the chip life time. The mean time to failure (MTTF) of Cu interconnection can be predicted by Black's equation, as shown in the following equations,[52]

$$\text{MTTF} = Aj^{-n}exp\left(\frac{A}{k_bT}\right) \tag{1.6}$$

where A is the constant, j is the current density, n is the model parameter, E_a is the activation energy for the electromigration, k_b is Boltzmann constant, and T is the temperature. As shown in Fig. 1.10(a),[4] the current density will be rapidly increased by

the reduction of cross-sectional area of interconnection. It accelerates the electromigration of Cu and leads to the reduction of chip life time as displayed in Fig. 1.10(b).[4] Since the structure of Cu interconnection is polycrystalline, the electromigration occurs along the grain boundaries. Therefore, the control of grain size and structure is possible to improve the electromigration resistance. The impacts of crystallinity and grain size on MTTF are described in the following equation,[53,54]

$$\text{MTTF} \propto \frac{d}{\sigma^2} \log \left[\frac{I_{111}}{I_{200}}\right]^3 \tag{1.7}$$

where σ is the standard deviation of grain sizes and I_{xyz} is the peak intensity of xyz orientation measured by X-ray diffraction. It can be expected that larger grain size, smaller standard deviation of grain size, and more development of Cu (111) orientation improve the life time of Cu interconnection.

Regarding the gap-filling, the continuous scaling of interconnection causes the reduction of deposition time and the increase in the probability to close the top of the trench originated from the roughness. When the trench with 24 nm width pattern is filled under the condition used for Cu superfilling at the trench width over 100 nm, the voids were frequently observed, as displayed in Fig. 1.11.

There are few candidates for resolving these issues related to conductivity, electromigration resistance, and the superfilling. First one is the modification of additives. The organic additives, adsorbing on Cu surface, exert superfilling as well as significantly affect the properties of Cu. The grain size should be increased to improve the conductivity and the electromigration resistance, therefore, the appropriate organic additives should be found, which form the Cu film with relatively large grains without reduction of superfilling performance. Second candidate is to apply pulse and pulse-reverse electrodeposition instead of direct current (DC) or constant potential deposition. The changes in the waveform of current or potential have the possibility for improving the properties as well as the superfilling performance. The final is to find new materials to meet the requirements of conductivity, electromigration resistance, and superfilling performance. Bimetallic interconnection based on Cu has been reported as the material having the higher electromigration resistance compared to pure Cu, however the deterioration of electrical conductivity is an inevitable corollary.[55-57] Graphene or Carbon nanotubes are issued as the new materials, however, the investigations on facile alignment, selective growth, and the contact formation are needed to improve the practicability of carbon-based materials.[4]

In this study, among these candidates, the impacts of pulse and pulse-reverse

electrodeposition on both the properties and superfilling performance were investigated.

The detail introduction of pulse and pulse-reverse electrodeposition is in the following

section.

Table 1.4. The Most Significant Issues in Cu Interconnection with the Dimension over 16 nm (Ref. 4)

Five Most Critical Challenges	Summary of Issues
Material Introduction of new materials to meet conductivity requirements and reduce the dielectric permittivity	The rapid introductions of new materials/processes that are necessary to meet conductivity requirements and reduce the dielectric permittivity create integration and material characterization challenges.
Manufacturable Integration Engineering manufacturable interconnect structures, processes and new materials	Integration complexity, CMP damage, resist poisoning, dielectric constant degradation. Lack of interconnect/packaging architecture design optimization tool
Metrology Achieving necessary reliability	New materials, structures, and processes create new chip reliability (electrical, thermal, and mechanical) exposure. Detecting, testing, modeling, and control of failure mechanisms will be key.
Metrology Three-dimensional control of interconnect features (with its associated metrology) is required to achieve necessary circuit performance and reliability	Line edge roughness, trench depth and profile, via shape, etch bias, thining due to cleaning CMP effects. The multiplicity of levels combined with new materials, reduced feature size, and pattern dependent processes create this challenge.
Cost & Yield for Manufacturability Manufacturability and defect management that meet overall cost/performance requirements	As feature sizes shrink, interconnect processes must be compatible with device roadmaps and meet manufacturing targets at the specified wafer size. Plasma damage, contamination, thermal budgets, cleaning of high A/R features, defect tolerant processes, elimination/reduction of control wafers are key concerns. Where appropriate, global wiring and packaging concerns will be addressed in an integrated fashion

Table 1.5. The Most Significant Issues in Cu Interconnection with the Dimension below 16 nm (Ref. 4)

Five Most Critical Challenges	Summary of Issues
Material Mitigate impact of size effects in interconnect structures	Line and via sidewall roughness, intersection of porous low-k voids with side wall, barrier roughness, and copper surface roughness will all adversely affect electron scattering in copper lines and cause increases in resistivity
Metrology Three-dimensional control of interconnect features (with it's associated metrology) is required	Line edge roughness, trench depth and profile, via shape, etch bias, thinning due to cleaning, CMP effects. The multiplicity of levels, combined with new materials, reduced feature size and pattern dependent processes, use of alternative memories, optical and RF interconnect, continues to challenge.
Process Patterning, cleaning, and filling at nano dimensions	As features shrink, etching, cleaning, and filling high aspect ratio structures will be challenging, especially for low-k dual damascene metal structures and DRAM at nano-dimensions.
Complexity Integration of new processes and structures, including interconnects for emerging devices	Combinations of materials and processes used to fabricate new structures create integration complexity. The increased number of levels exacerbate thermomechanical effects. Novel/active devices may be incorporated into the interconnect.
Practical Approach for 3D Identify solutions which address 3D structures and other packaging issues	3 dimensional chip stacking circumvents the deficiencies of traditional interconnect scaling by providing enhanced functional diversity. Engineering manufacturable solutions that meet cost targets for this technology is a key interconnect challenge.
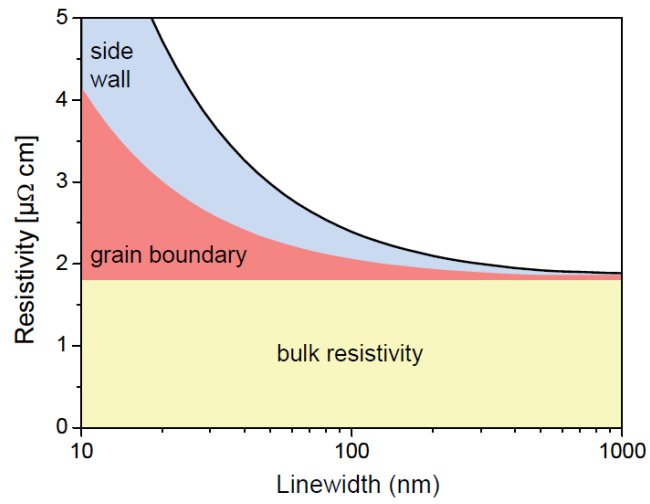
Fig. 1.9. The expected resistivity of Cu interconnection according to the line width (Ref. 2).

(a)
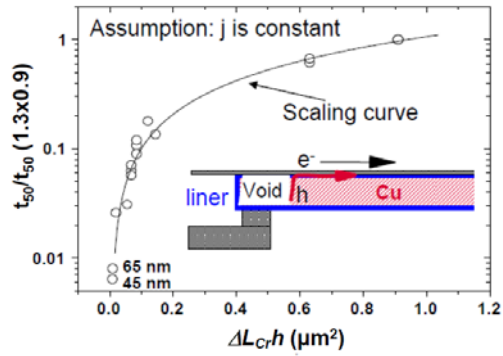
(b)
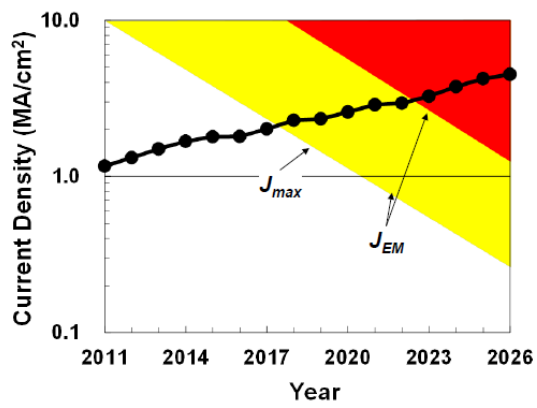
Fig. 1.10. (a) The life time of Cu interconnection according to the interconnection geometry (Ref. 4) and (b) the predicted current density passing through the interconnection (Ref. 4).
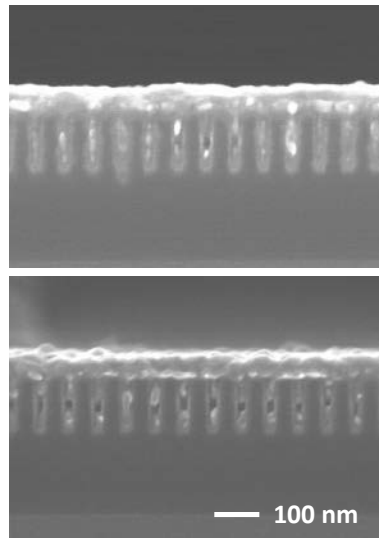
Fig. 1.11. The failure of Cu superfilling at the trench having 24 nm width and 120 nm

depth.

1-4. Pulse and pulse-reverse electrodeposition

DC or constant potential deposition which is to apply the constant current or potential has been generally used for Cu electrodeposition. However, as addressed before, the properties of Cu interconnection and superfilling performance should be improved, and the pulse and pulse-reverse electrodeposition can be a solution for resolving these issues.

Pulse electrodeposition consists of iterations of deposition and relaxation, the periods of which are called on- and off-times, respectively.[58-68] The representative waveform of pulse electrodeposition is exhibited in Fig. 1. 12(a). Cu ions are consumed during on-time by the reduction and replenished from the bulk electrolyte during off-time. This replenishment of Cu ions during off-time enables to apply a relatively high current (or potential) compared to DC deposition, meaning that the extension of the applicable range of current for Cu electrodeposition. This improves the filling performance when the mass-transport of Cu ions governs the electrodeposition system. Moreover, pulse electrodeposition has many advantages in the aspect of film properties like the reduction of the film roughness, the formation of uniform grains, and the promotion of nucleation on the heterogeneous substrate.[60-65] In addition, it was reported that pulse

electrodeposition with the addition of thiourea enhances the formation of twin

boundaries, which improves the mechanical strength even with the increase in the

ductility.[66-68] Pulse electrodeposition can be described by the duty cycle, frequency, and

the average current density. The following equations are the definitions of duty cycle,

frequency, and the average current density,

$$\text{Duty cycle } (\%) = \frac{t_{on}}{t_{on} + t_{off}} \times 100 \tag{1.8}$$

$$\text{Frequency (Hz)} = \frac{1}{t_{on} + t_{off}} \tag{1.9}$$

$$\text{Average current density } (\text{mA}/cm^2)$$

$$= \frac{i_{peak} \times t_{on}}{t_{on} + t_{off}} \text{ for galvanostatic electrodeposition}$$

$$= \frac{C_{on}}{t_{on} + t_{off}} \text{ for potentiostatic electrodeposition} \tag{1.10}$$

where t_{on} and t_{off} are the length of on- and off-time, i_{peak} is applied peak current

density, and C_{on} is the amount of passed electrons during on-time per unit area. In

many previous reports, it was attempted to characterize the pulse electrodeposition

using these terms.

The anodic step, where an anodic potential (positive potential with respect to the open

circuit potential (OCP)) or anodic current is applied, is occasionally added to pulse electrodeposition and the resulting process is referred to as pulse-reverse electrodeposition.[69-78] The representative waveform of pulse-reverse electrodeposition is displayed in Fig. 1. 12(b). The time to apply the anodic potential is called to reverse time. It has been reported that pulse-reveres electrodeposition is adopted for through silicon via (TSV) filling and the formation of alloy films. Furthermore, the protrusions formed on the Cu surface and at the side wall of the trench or via can be selectively dissolved during the anodic step in pulse-reverse electrodeposition, resulting in the enhancement of the superfilling performance and a reduction of the surface roughness.

  Similar to the pulse electrodeposition, the frequency and average current density could be defined as described in the following,

$$\text{Frequency (Hz)} = \frac{1}{t_{on} + t_{off} + t_{reverse}} \qquad (1.11)$$

Average current density (mA/cm^2)

$$= \frac{i_{cathodic} \times t_{on} - i_{anodic} \times t_{reverse}}{t_{on} + t_{off} + t_{reverse}} \text{ for galvanostatic electrodeposition}$$

$$= \frac{C_{cathodic} - C_{anodic}}{t_{on} + t_{off} + t_{reverse}} \text{ for potentiostatic electrodeposition} \qquad (1.12)$$

where $t_{reverse}$ is the reverse time, $i_{cathodic}$ (same to i_{peak} in pulse electrodeposition) and i_{anodic} are the current density at on- and reverse time, and $C_{cathodic}$ and C_{anodic} are the amount of passed electrons during on- and reverse time per unit area. In addition to that, the dissolution ratio can be defined as the ratio between the amounts of deposition and dissolution as shown in the following equation.[79]

$$\text{Dissolution ratio (\%)} = \frac{C_{anodic}}{C_{cathodic}} \times 100 \qquad (1.13)$$

In this study, the impacts of pulse and pulse-reverse electrodeposition on the properties of Cu thin films such as the crystallinity, grain size, surface roughness, and resistivity. Especially, the influences of off-time in pulse electrodeposition and the anodic step in pulse-reverse electrodeposition were intensively investigated. In Chapter III, the film property changes by pulse electrodeposition are introduced. In Chapter IV, the influences of pulse-reveres electrodeposition are explained in detail. In Chapter V, the impacts of anodic step in the pulse-reverse electrodeposition on the competitive adsorption of organic additives and superfilling performance are shown.

(a)

(b)
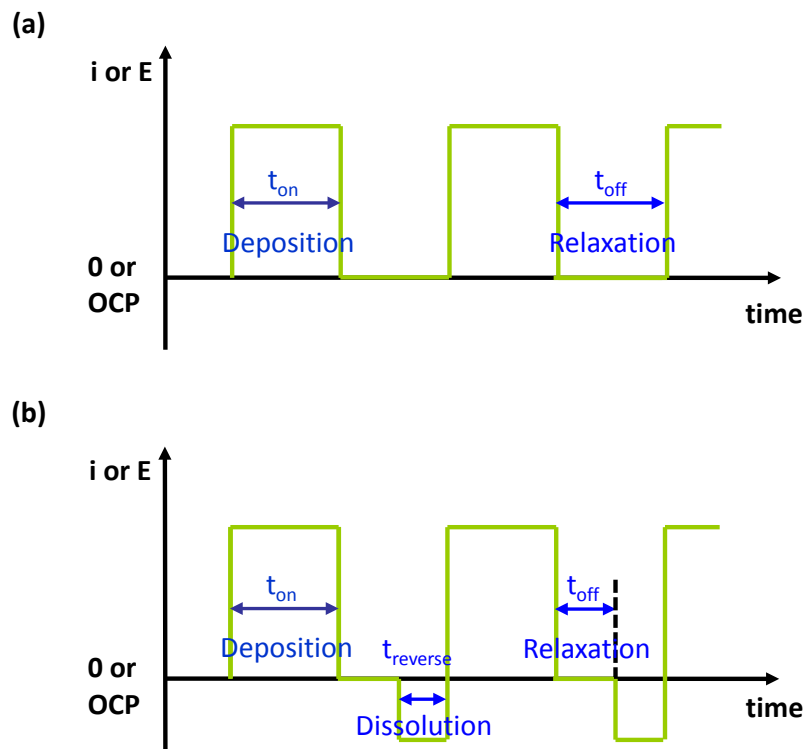
Fig. 1.12. The representative waveforms of (a) pulse and (b) pulse-reverse electrodeposition.

CHAPTER II

Experimental

2-1. Electrolyte, organic additives, and electrodeposition system

The basic electrolytes consisted of 0.25 M $CuSO_4$ and 1.0 M H_2SO_4. In order to investigate the effects of organic additives, 88 μM of polyethylene glycol (PEG, Mw=3,400), 1 mM NaCl, and 50 μM of bis(3-sulfopropyl) disulfide (SPS) were added into the electrolyte, which were generally used for Cu superfilling. The temperature of electrolyte was precisely maintained at 30°C by a thermostat.

Electrodeposition was enabled using a PAR 273A potentiostat (EG&G Princeton Applied Research Corporation). In the research with galvanostatic deposition, the potential was varied over a wide range using both DC and pulse electrodeposition.[80] The differences in the response potential between deposition modes were usually sufficient to mask the effects of waveforms. For this reason, the potentiostatic electrodeposition was employed for pulse and pulse-reverse electrodeposition, in which the cathodic and anodic potentials were controlled, to clarify the effects of the variables in pulse and pulse-reverse electrodeposition.

Electrodeposition was performed in a three-electrode system. The counter and two reference electrodes were a 99.9% Cu wire, saturated calomel electrode (SCE), Ag/AgCl (KCl saturated) electrode, respectively. The working electrodes were Cu blanket wafer for Cu film deposition, Cu patterned wafer for superfilling, and Cu rotating disk electrode (RDE) having 0.196 cm^2 of active area for electrochemical analyses. In Chapter III, Cu blanket wafer with a structure of Cu seed layer (60 nm, PVD) / Ta (7.5 nm, PVD) / TaN (7.5 nm, PVD) / SiO$_2$ was used for pulse electrodeposition. In Chapter IV, the blanket wafer with a structure of Cu seed layer (40 nm, PVD) / Ta (7.5 nm, PVD) / SiO$_2$ was employed for pulse-reverse electrodeposition. In Chapter V, two kinds of patterned wafer were used, of which structures were (i) Cu seed layer (7.5 nm, PVD)/Ta (6 nm, PVD)/TaN (1.5 nm, PVD)/Si with 300 nm of depth and 55 nm of width, and (ii) Cu seed layer (30 nm, PVD)/Ta (7 nm, PVD)/Si with various widths and 240 nm of depth. The wafer was loaded in a Teflon holder and 1 cm^2 of geometric area was exposed to the stationary electrolyte.

In order to maintain the consistent state of Cu seed layer, the pretreatment for Cu blanket and patterned wafers was carried out prior to the electrodeposition by dipping into an aqueous solution composed of 0.020 M citric acid and 0.034 M KOH for 2 min.

For the patterned wafer with the structure of 300 nm depth and 55 nm width, the dipping time was reduced to 30 s because the seed layer was much thinner than the others.

2-2. Pulse electrodeposition for Cu film deposition

In Chapter III, the constant potential deposition and pulse electrodeposition were performed with the cathodic potentials of -100, -200, and -400 mV with respect to open circuit potential (OCP) to deposit Cu films and compare the film properties achieved with different cathodic potentials. The reasons for applying this potential with respect to the OCP were to control the exact overpotential that is a driving force for electrodeposition and to derive a current density of 0 mA/cm^2 for 0 mV of cathodic potential during the off-time. The duty cycle of pulse electrodeposition was varied over the range from 25% to 75%, and the frequency was fixed at 1 Hz. Fig. 2.1 shows the potential as a function of time for the constant potential deposition and pulse electrodeposition processes. In addition, pulse electrodeposition was conducted while varying the on- and off-times with a fixed peak potential of -200 mV to clarify the detail effect of the on- and off-times. When the identical cathodic potentials in constant

potential and pulse electrodeposition modes were applied, the on- and off-times could be treated as the only variable affecting the film properties. The thickness of Cu was restricted to 260 nm ± 5%, including the seed layer.

2-3. Pulse-reverse electrodeposition for Cu film deposition

In Chapter IV, pulse-reverse electrodeposition was carried out potentiostatically to precisely control the driving force of Cu reduction and dissolution. A waveform of pulse-reverse electrodeposition is represented in Fig. 2.2. The cathodic potential ($E_{cathodic}$), on-time, and off-time were fixed at -200 mV (vs. OCP), 0.25 s, and 1.0 s, respectively. These conditions were identical to the optimum of pulse electrodeposition determined in Chapter III, which were obtained with the consideration of Cu (111) peak intensity measured from XRD and the electrical resistivity. The anodic potential (E_{anodic}) was varied from 25 to 150 mV (vs. OCP), and the reverse time was changed from 0.025 to 0.5 s. Pulse electrodeposition under the optimum conditions was also performed as a criterion for the pulse-reverse electrodeposition.

The film thickness including the Cu seed layer was restricted to 150 nm (±5%) by controlling the total deposition charge to rule out the effect of thickness on the film

properties. Comparing Chapter III, the thickness of Cu film including Cu seed layer was reduced from 260 nm to 150 nm in order to reflect the continuous reduction of the Cu interconnection dimensions.

In the experiments with organic additives, the electrochemical behavior of Cu dissolution should be investigated prior to the film deposition. Therefore, linear sweep voltammetry (LSV) was performed to compare the influences of the additive adsorption during the anodic step. The potential was swept from - 300 to 300 mV with respect to an Ag/AgCl electrode, and the scan rate was fixed to 10 mV/s. A Cu rotating disk electrode (RDE) with an active area of 0.196 cm^2 was employed as a working electrode and was rotated at a constant speed of 300 rpm. A 99.9% Cu rod and an Ag/AgCl electrode were also used as counter and reference electrodes, respectively.

2-4. Pulse-reverse electrodeposition for Cu superfilling

In Chapter V, potentiostatic pulse-reverse electrodeposition only consisting of the cathodic and anodic steps were used as displayed in Fig. 2.3. The potential was applied with respect to initial OCP to exactly control the driving forces for the cathodic and anodic reactions. The cathodic potential was varied from -100 mV to -200 mV (vs.

OCP) with fixed on-time of 0.25 s. The anodic potential and reverse time were ranged between 25 mV and 100 mV, and 0.05 s and 0.5 s, respectively. The constant potential deposition was performed with various cathodic potentials in various electrolytes to compare the adsorption state to pulse-reverse electrodeposition. From the current transitions from various conditions, the displacement rates of PEG-Cl$^-$ by SPS, the saturation time, and the saturation current were compared to each other. Processing of current profiles and the definitions of initial displacement rate, saturation time, the saturation current will be introduced in next section.

The electrochemical analyses were additionally performed to clarify the detail influences of anodic step on the competitive adsorption between PEG-Cl$^-$ and SPS, such as potential step chronoamperometries in the electrolyte containing PEG-Cl$^-$-SPS, the chronoamperometries after PEG-Cl$^-$ derivatization, LSV in the electrolyte only containing PEG-Cl$^-$. More information and the meaning of each electrochemical analysis will be explained in Chapter V.

In order to investigate the superfilling performance based on the electrochemical behavior, pulse-reverse electrodeposition was performed with -200 mV (vs. OCP) of cathodic potential and 0.25 s of on-time. The anodic potential and reverse time were changed from 25 mV to 100 mV and from 0.025 s to 0.5 s, respectively. The constant

potential deposition with -200 mV of overpotential was also carried out as a criterion for the pulse-reverse electrodeposition.

2-5. Analyses of film properties and deposition profiles

The thickness of Cu film and the deposition profiles at various trenches were observed by field emission scanning electron microscopy (FESEM, (i) S-4800, Hitachi, and (ii) JSM-6701F, JEOL). The resistivity of Cu film was calculated from the thickness and sheet resistance measured by a four-point probe (CMT-SR1000N, Chang Min Tech Co.). The film orientation was assessed from the Cu (111) peak intensity obtained by X-ray diffraction (XRD, D8 Advance, Bruker). The grain size was estimated by the full width at half maximum (FWHM) of the Cu (111) peak from the XRD patterns and transmission electron microscopy (TEM, JEM-3000F, JEOL). In addition, the grain size at the surface was measured using the FESEM (SUPRA 55VP, Carl Zeiss) back-scattering electron (BSE) detector. Atomic force microscopy (AFM, XE-150, Park Systems) was used to measure the film roughness. To minimize the effect of self-annealing, the samples were analyzed exactly 5 days after the deposition.
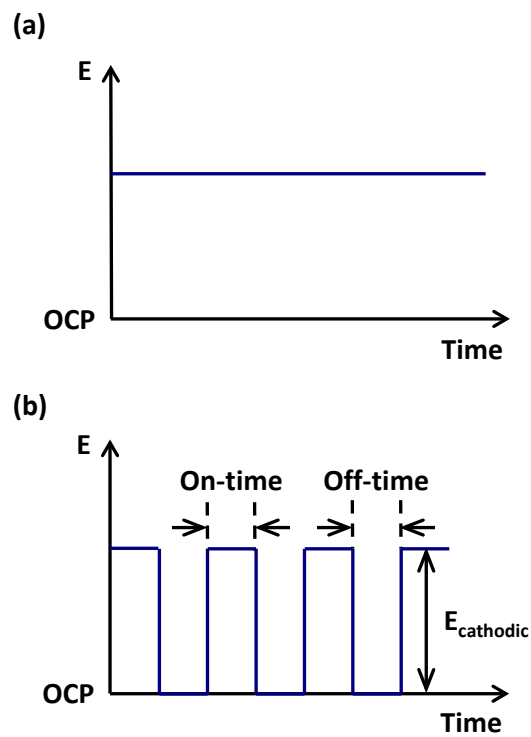
Fig. 2.1. The waveforms of (a) constant potential deposition and (b) pulse electrodeposition with the definitions of cathodic potential, on- and off-times (Chapter III).
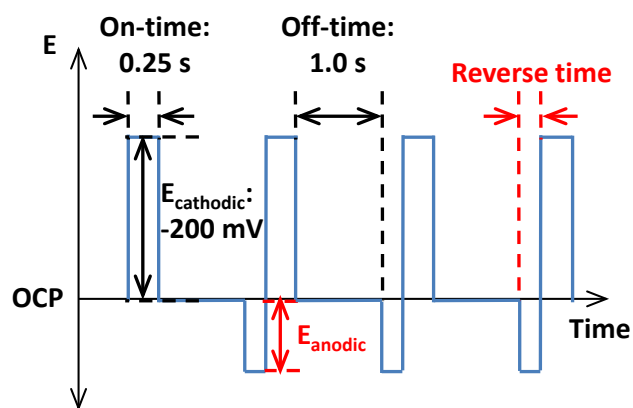
Fig. 2.2. The waveform of potentiostatic pulse-reverse electrodeposition with the definitions of anodic potential and reverse time (Chapter IV).
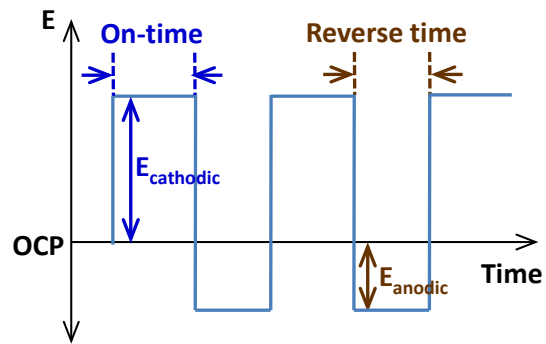
Fig. 2.3. The waveform of potentiostatic pulse-reverse electrodeposition consisted of cathodic and anodic steps (Chapter V).

CHAPTER III

The characteristics of Cu films deposited by pulse electrodeposition

3-1. Pulse electrodeposited Cu films in the absence of additives

 Fig. 3.1(a) shows the Cu (111) peak intensities of Cu films deposited by constant potential deposition and pulse electrodeposition with various cathodic potentials and duty cycles, which were measured by XRD. Peaks other than (111) did not appear because the Cu seed layer used in this investigation had a well-developed (111) orientation, and the thickness of deposited Cu films was about 250 nm, which was not enough to develop the other orientations. Since the differences of thickness were controlled within 5%, the intensity of Cu (111) implied the amount of Cu (111) plane. Both deposition modes showed a decreasing tendency of Cu (111) intensity as the cathodic potential became more negative. Increasing the cathodic potential means the application of a higher driving force for Cu reduction. It was reported by Rashkov et al. that the cathodic potential had an influence on film orientation based on the calculation of the work of formation for particular planes.[81] High cathodic potential, and thus a

high driving force for Cu electrodeposition and fast deposition rate, promote the formation of orientations other than (111). The (200) peak was not observed in this investigation, and therefore, the decrease in Cu (111) intensity under high cathodic potential was due to the increase in the amount of random orientation in the deposited film. In addition, an increase in cathodic potential also decreased the grain size, and reduced the Cu (111) intensity. It is significant that the Cu (111) intensity increased as the duty cycle decreased, i.e., a decrease in the on-time and an increase in the off-time. The significance of these observations is described below. The average current density has been used for describing the characteristics of pulse electrodeposition. Fig. 3.1(b) shows the dependence of peak intensity on the average current density as the x-axis. The average current density was calculated with the equation (1.10). The Cu (111) intensity seemed to be well related to the average current density, but the deviations from this curve came from changes in on- and off-times. Even though identical average current density was applied, shorter on- and longer off-times enhanced the Cu (111) intensity. The cathodic potential governed the crystallinity of the electrodeposited Cu film, as explained above, and higher potential usually shows lower Cu (111) intensity.

The surface morphologies of Cu films are represented in Fig. 3.2. It was observed that the application of more negative potential reduced the surface roughness regardless of

deposition modes or duty cycles. It was widely reported that the Cu film deposited with higher overpotential or relatively fast deposition rate showed more smooth film with fine grains. Interestingly, it seemed that the duty cycle could not strongly affect the surface roughness. From these Cu films, the root-mean-square roughness was measured, and the results are displayed in Fig. 3.3. Dissimilar to the Cu (111) peak intensity, little difference of surface roughness was observed between the results of constant potential and pulse electrodeposition modes. Fig. 3.3(a) shows the decrease in roughness corresponding to the increase in the cathodic potential. AFM observations showed that the cathodic potential strongly affected the surface roughness, whereas the duty cycle did not that much. The relationship between average current density and surface roughness was also considered in Fig. 3.3(b). Similar to Fig 3.1(b), the average current density was not sufficient to accurately describe the changes in surface roughness. Generally, higher average current densities smoothen Cu film because of the enhancement of nucleation. However, applied average current densities varied from 6 to 38 mA/cm^2 showed similar surface roughness.

Fig. 3.4(a) shows the resistivity as a function of the deposition conditions; a slight reduction in resistivity occurred as the cathodic potential increased. The resistivity was 10% - 30% less with pulse electrodeposition than with constant potential deposition,

and the resistivity also decreased as the duty cycle decreased. In general, several major

factors affect the film resistivity, including phonon scattering, grain boundary

scattering, surface-induced scattering, and scattering at impurity atoms.[37-50] In this

investigation, the effect of changes in the phonon scattering was negligible because the

phonon scattering was strongly related to the temperature and kinds of material. The

influence of roughness on the resistivity was also negligible because the degree of film

roughness was almost identical for the same cathodic potential in both deposition

modes. The amount of impurities was assumed to be almost constant because the film

was deposited in the same aqueous electrolyte without any additives. Therefore, any

differences in resistivity between constant potential deposition and pulse

electrodeposition could be attributed to scattering at the grain boundary. In order to

confirm the dependency of resistivity on the average current density, the results were

re-plotted with the average current as the x-axis (Fig. 3.4(b)). Similar to Cu (111)

intensity and surface roughness, the film resistivity could not be explained fully by the

average current density. On the basis of these results, the characterization of pulse

electrodeposition using the average current density was not sufficient, and the each

effect of on- and off-times should be separately considered.

To clarify the details of pulse electrodeposition such as the effects of on- and off-

times, the experiments were performed with a fixed peak potential of -200 mV with respect to the OCP and various on- and off-times. The on- and off-times were varied while the peak potential was kept constant to examine the effects of these parameters on the film properties. The film properties as a function of the off-time were measured with a peak potential of -200 mV and on-times of 0.25, 0.5, and 1.0 s. Figs. 3.5(a) and (b) show the Cu (111) intensity and resistivity, respectively. All results indicated that the pulse electrodeposition resulted in a higher Cu (111) intensity and lower resistivity than with constant potential deposition. Of particular note, the film properties were improved by increasing the off-time up to 1.0 s and were not affected by off-times greater than 1.0 s. This indicates that the peculiar change during the off-time progressed continuously up to 1.0 s and was almost complete at that off-time. After that, no further change occurred, and therefore, the film properties were saturated.

Generally, the pulse electrodeposition is well-known to have an advantage of mass transport during the off-time. To confirm the effect of mass transport, the identical experiments were conducted using a rotating cell with speed of 500 rpm. The exact values of Cu (111) peak intensity could not be compared because of the modification of XRD detector, therefore, the experiments without and with rotating were performed at the same time. The tendency and saturation according to the on- and off-times were

also observed in Fig. 3.6. Consequently, it can be concluded that the changes in the Cu

ion concentration at the surface during the off-time was not a major factor to determine

the film properties.

 In addition, judging from the change of film properties as a function of the on-time, it

is clear that the amount of as-deposited Cu in a unit cycle of pulse electrodeposition

was a significant variable that affected the film properties because the results with

various duty cycles (Fig. 3.2 to 3.4) were originated from the summation of on- and

off-time impacts. To investigate the effect of the on-time which determined the amount

of deposition per unit cycle at a fixed peak potential, various on-times were tested for a

fixed off-time of 1.0 s, which was considered sufficient to change the deposited Cu in

the unit cycle. Fig. 3.7 illustrates these results with the reciprocal of the on-time on the

x-axis. This figure shows that the film properties were improved by decreasing the on-

time from 1.0 to 0.25 s, but were not improved for on-times of less than 0.25 s. An on-

time of 0.25 s corresponded to 2.0 nm of deposited Cu per unit cycle. This amount of

deposited Cu should be the maximum thickness that can be fully changed during 1.0 s

of off-time in the electrolyte. For an on-time, greater than 0.25 s, not all of the

deposited Cu could be changed because the amount of Cu deposit was greater than 2.0

nm. Admittedly, the improvement in the film properties achieved by decreasing the on-

time was due to the increase in the fraction of changed Cu during the off-time. In contrast, the film properties were saturated for an on-time of less than 0.25 s because the off-time was sufficient to change the deposited Cu fully. Consequently, the change during the off-time took place at the surface, and the maximum thickness that could be improved was about 2.0 nm.

  As discussed above, the quality of the deposited Cu was improved during the off-time through an increase in Cu (111) intensity and decrease in the resistivity. To clarify the nature of the change occurring during the off-time, the grain sizes and distribution were estimated by TEM. Additionally, it is assumed that the effect of each pulse is not much different and the summation of unit pulse determines the whole film property, and the changes during the off-time were deduced from the results of grain size. Constant potential deposition was compared with pulse electrodeposition for different off-times while the peak potential and the on-time were fixed at 0.25 s. Figs. 3.8 and 3.9 show representative TEM images captured for each condition and the distributions of grain sizes estimated from more than 200 individual grains. The average grain sizes were 54.0, 63.0, and 72.9 nm for constant potential deposition, pulse electrodeposition with an off-time of 0.3 s, and pulse electrodeposition with an off-time of 1.0 s, respectively. These results indicate that the grain growth took place during the off-time. The

improvements in film properties with increased off-time were well-explained by the grain growth.

Electrodeposited Cu film experiences grain growth after deposition in a process referred to as self-annealing.[82-88] The incubation time for the start of self-annealing increases as the Cu film becomes thinner, and may be several tens or hundreds of hours.[86-88] The grain growth during the off-time observed in this research was significantly different from self-annealing because it was almost complete after 1.0 s of off-time. In addition, the grain growth occurred without the addition of additives, whereas self-annealing takes place with incorporated additives, especially bis(3-sulfopropyl) disulfide (SPS).[89] Another difference is that grain growth occurred in contact with the electrolyte, whereas self-annealing takes place under atmospheric conditions. This suggests the possibility of various processes for grain growth during the off-time.

In the case of Cu, the (111)-oriented plane has the lowest surface energy; however, electrodeposition progresses with the distribution of energy and does not necessarily mean a thermodynamically stable state. The total energy of Cu grains is the surface energy related to orientation and the grain boundary energy. The change during the off-time should take place in the direction of decreasing total energy of the

electrodeposited Cu. Specifically, the grains or nuclei with a lower energy grew during the off-time to reduce the total energy, resulting in an increased Cu (111) intensity and decreased film resistivity. In other words, the driving force for grain growth during the off-time was originated from the reduction of total energy. Although dynamic equilibrium between electrode and electrolyte was maintained during the off-time, the grains having lower energy could grow and the grains having higher energy could be dissolved spontaneously, where total current density was zero. The candidate mechanism for this grain growth might be ripening through electrolyte and recrystallization. In the initial stage of electrodeposition, in particular, the nuclei that were not (111)-oriented or relatively small in size could combine with (111)-oriented or large-sized nuclei. It was clear from the above results that this process occurred in a second while in contact with the electrolyte, not under atmospheric conditions. The process seemed to be completed in a second could be found in Fig. 3.5, which was the film properties were saturated over 1.0 s of off-time. It implied that any other changes did not occur after 1.0 s of off-time, even though 2.0 or 3.0 s of off-time was applied. However, determining which process had a greater influence on the grain growth is difficult.

Fig. 3.10 shows the schematic diagrams of constant potential deposition and pulse

electrodeposition which were based on the results described in Fig. 3.5. The constant

potential deposition caused the Cu to accumulate continuously without providing any

chance for grain growth or recrystallization, and it thus produced a Cu film that could

be thermodynamically unstable compared to Cu deposited by pulse electrodeposition.

With pulse electrodeposition, on the other hand, the nuclei or grains deposited during

the unit cycle experienced grain growth and recrystallization that reduced the total

energy. Off-times of less than 1.0 s were not sufficient to complete the changes for

deposited Cu during a unit cycle. Consequently, the Cu deposited during the following

pulse covered the relatively unstable surface. Similarly, on-times of more than 0.25 s

deposited Cu too thick, which cannot be improved fully even though enough off-time

applies. On the other hand, an off-time of 1.0 s was sufficient to change all the

deposited Cu during the unit cycle, and, therefore, using a succession of pulses, the

whole film was in the thermodynamically most stable state that could be obtained in

the electrolyte. As a result, for off-times greater than 1.0 s, the film properties were

saturated because the film to be changed had already experienced grain growth and

recrystallization. Additionally, the improvement of film properties by grain growth was

not affected by the whole film thickness. The total film properties were determined by

the summation of each effect in unit pulse, and it was confirmed with film with 600 nm.
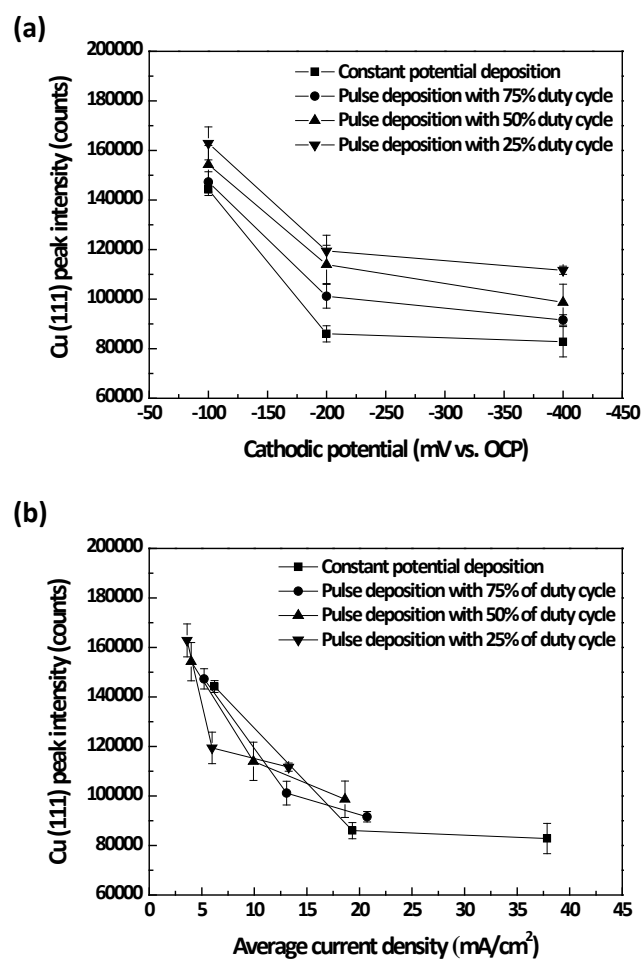
Fig. 3.1. (a) The Cu (111) peak intensities measured from XRD according to the cathodic potentials and duty cycles, and (b) re-plotted results with the average current density as the x-axis; the points in the each line represent the -100, -200, and -400 mV (vs. OCP) in sequence from left to right.
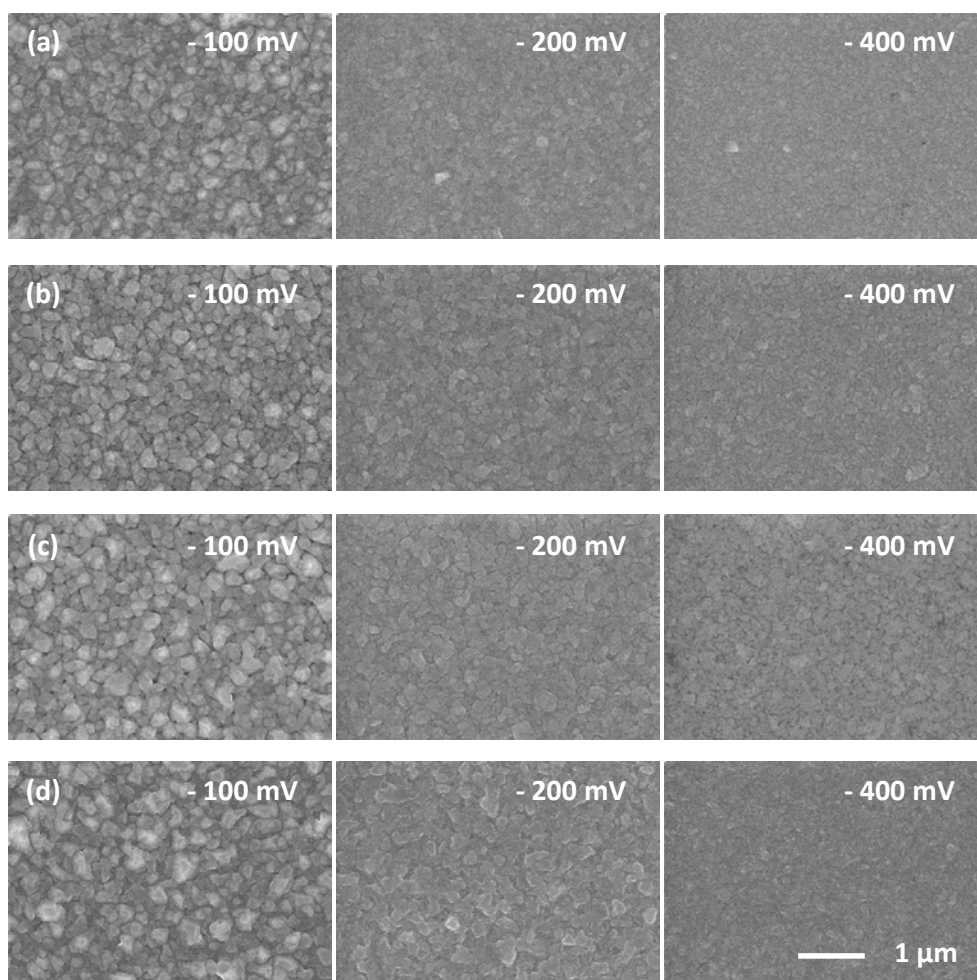
Fig. 3.2. Surface morphologies of Cu films deposited by means of (a) constant potential deposition, and pulse electrodeposition with (b) 75%, (c) 50%, and (d) 25% of duty cycles. The cathodic potentials were exhibited at the upper left corner of each image.
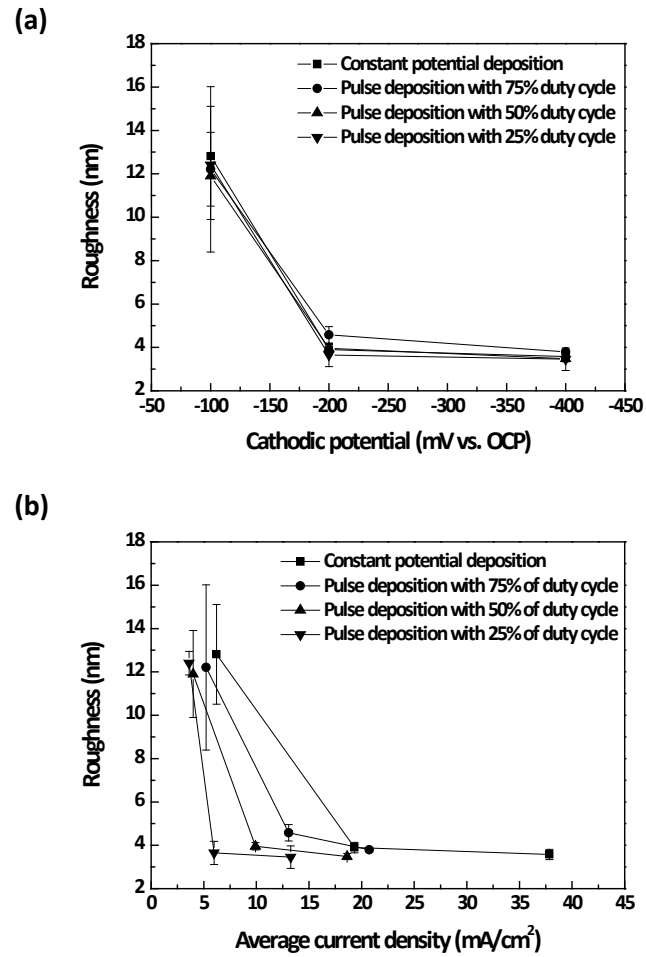
Fig. 3.3. (a) RMS roughness of Cu films exhibited in Fig. 2.3, and (b) re-plotted results

with the average current density as the x-axis.

(a)

(b)
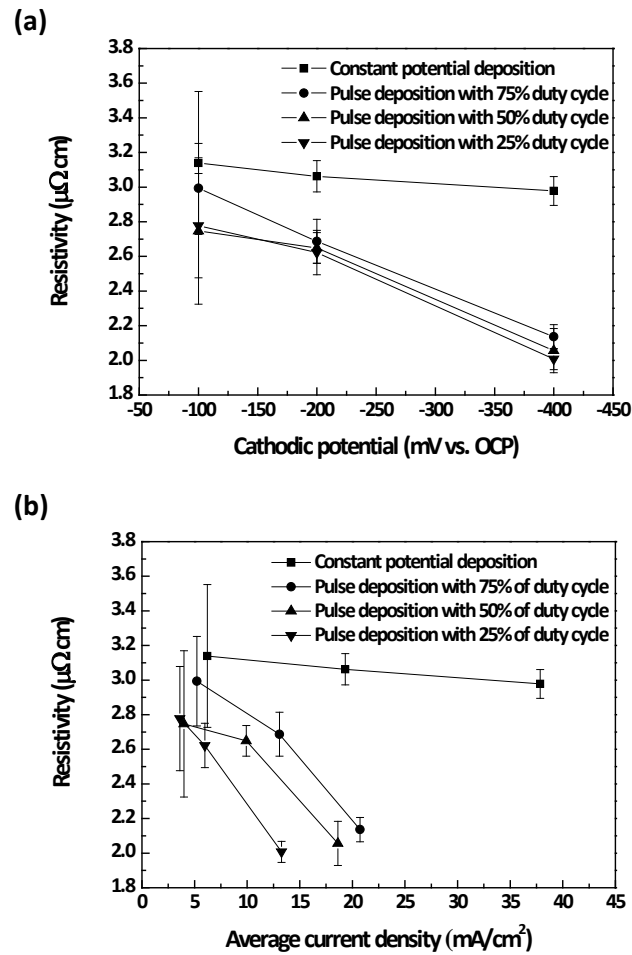
Fig. 3.4. (a) The electrical resistivity of Cu films according to the cathodic potentials

and duty cycles, and (b) re-plotted results with the average current density as the x-axis.

(a)

(b)
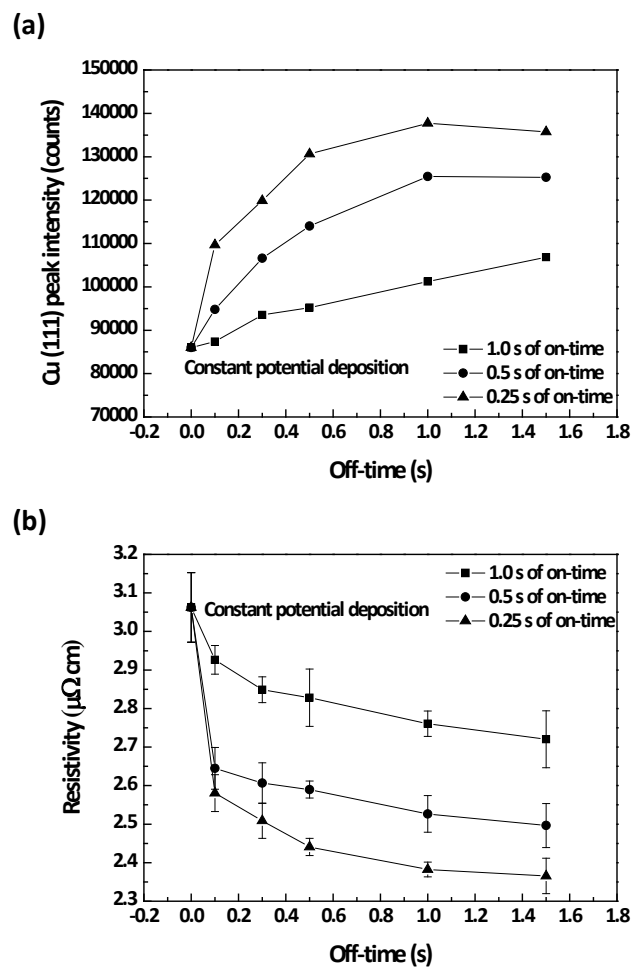
Fig. 3.5. The behaviors of (a) Cu (111) peak intensity from XRD and (b) the electrical

resistivity according to the on- and off-times.
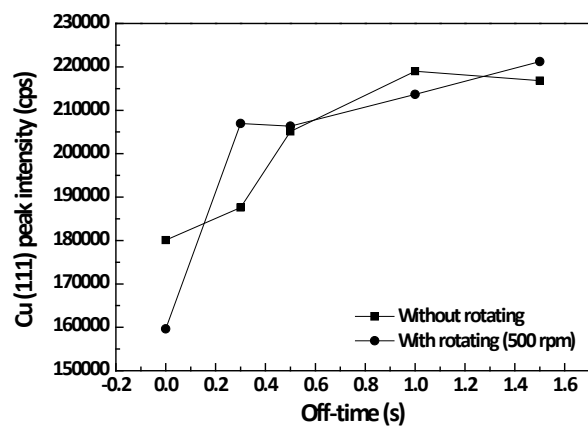
Fig. 3.6. Cu (111) peak intensities with and without rotating of substrates during the electrodeposition.

(a)

(b)
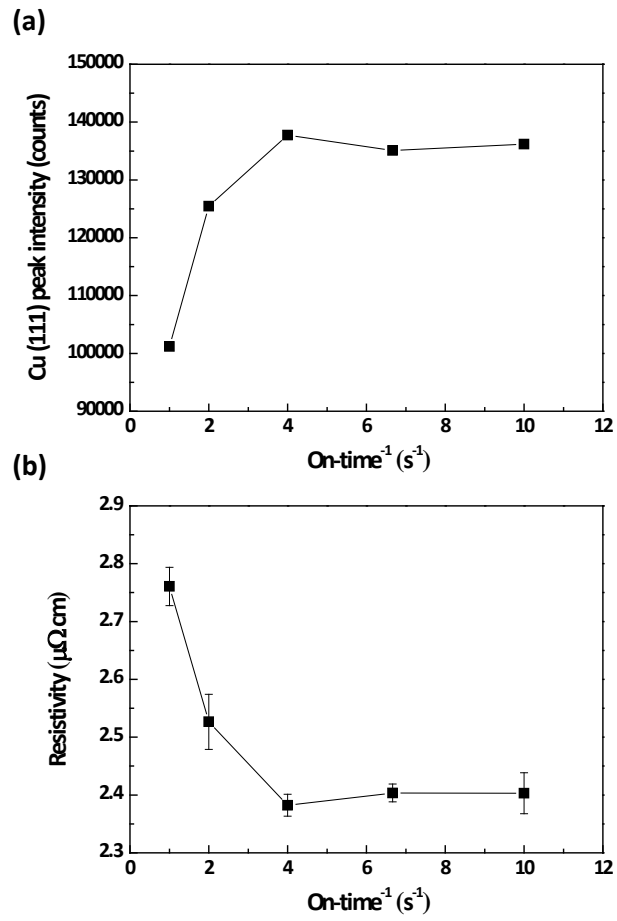
Fig. 3.7. The behaviors of (a) Cu (111) peak intensity and (b) the electrical resistivity according to the on-time with a constant off-time of 1.0 s.
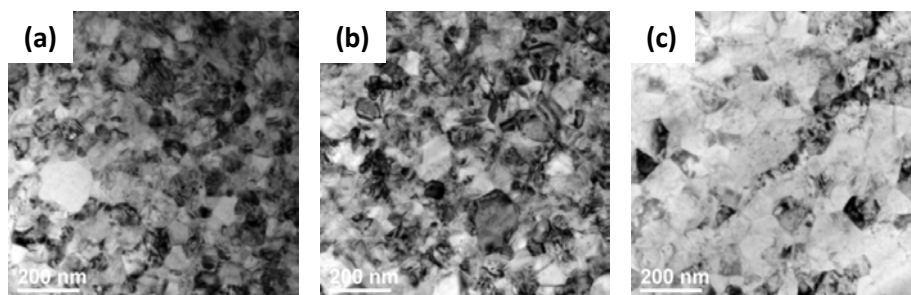
Fig. 3.8. TEM images of Cu films deposited by means of (a) constant potential deposition, and pulse electrodeposition with an off-time of (b) 0.3 s and (c) 1.0 s.
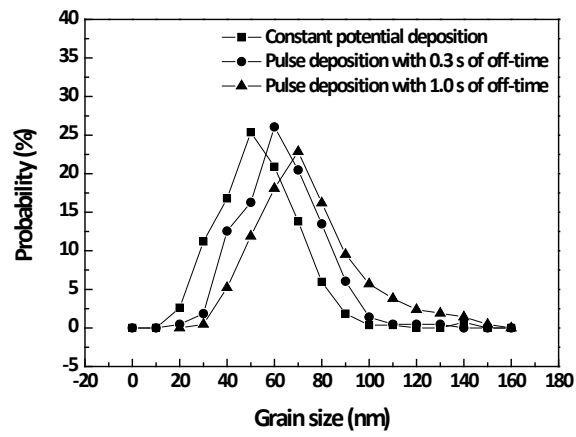
Fig. 3.9. The distributions of grain size measured from Fig. 3.8.
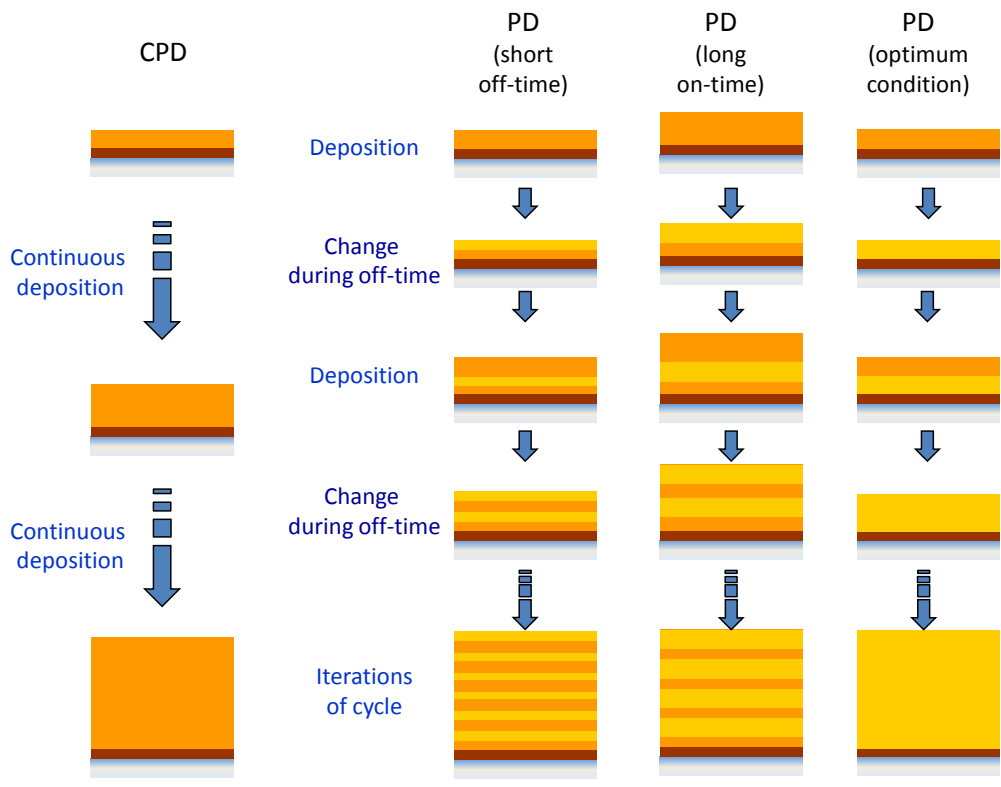
Fig. 3.10. Schematic diagrams of constant potential and pulse electrodeposition explaining the changes in the film property according to the on- and off-times.

3-2. Pulse electrodeposited Cu films in the presence of additives

As mentioned above, the optimum conditions of pulse electrodeposition was found to be 0.25 s of on-time and 1.0 s of off-time with -200 mV (vs. OCP) of cathodic potential. This was obtained from the electrolyte without any organic additives employed for Cu superfilling. The organic additives such as Cl⁻, PEG, SPS, and JGB easily adsorbed on Cu surface, and it has the potential to retard the changes during the off-time. At first, pulse electrodeposition in the electrolyte only containing Cl⁻ was performed with various off-times. The behaviors of Cu (111) peak intensity and resistivity are represented in Fig. 3.11. It was exhibited that the dependency of film properties on off-time was exactly identical to the results without additives in the aspect of the saturation off-time and the direction of film property changes according to the off-time. The resistivity and the Cu (111) peak intensity were increased with the off-time below 1.0 s, followed by the saturation. This implied that the chloride ion could not strongly affect the grain growth during the off-time.

On the other hand, the application of PEG, SPS, and JGB retarded this grain growth during the off-time. The peak intensities of Cu (111) with various combinations of organic additives from constant potential deposition and pulse electrodeposition are

displayed in Fig. 3.12. The optimum conditions of pulse electrodeposition determined by the results without additives were used for this experiment. Comparing the values of Cu (111) intensities, it can be found that the addition of organic additives into the electrolyte reduced the advantage of pulse electrodeposition. The increments of crystallinity resulted from the grain growth during the off-time were 68% without additives, 8.9%, 6.5%, and 4.2% with PEG-Cl$^-$, PEG-Cl$^-$-SPS, and PEG-Cl$^-$-SPS-JGB, respectively. The strong adsorption of organic additives on Cu surface reduced the impacts of energy differences, resulting in the retardation of grain growth.

Similar to the Cu (111) peak intensity, the behavior of resistivity was also affected by the organic additives. Fig. 3.13 represents the resistivities of Cu films deposited by constant potential deposition and pulse electrodeposition with various combinations of organic additives. It was observed that the reduction of resistivity with pulse electrodeposition was offset by the organic additives, of which degree was in order of PEG-Cl$^-$ < PEG-Cl$^-$-SPS < PEG-Cl$^-$-SPS-JGB. The decreases in the resistivity were 22% without additives, 6.9%, 4.2%, and 0.4% with PEG-Cl$^-$, PEG-Cl$^-$-SPS, and PEG-Cl$^-$-SPS-JGB, respectively. This tendency of resistivity was also identical to the results of Cu (111) peak intensity, which implied that the strong adsorption of organic additives reduced the grain growth during the off-time.

On the basis of these results, the introduction of organic additives used for Cu metallization reduced the degree of grain growth during the off-time by the strong adsorption on Cu surface. Since it implied that the pulse electrodeposition was not sufficient to remarkably improve the electrical resistivity with the organic additives, the additional modification of waveform was needed to reduce the resistivity. Therefore, in this study, pulse-reverse electrodeposition was employed to achieve further improvement of electrical properties with the organic additives. In the following chapter, the characteristics of Cu film deposited by pulse-reverse electrodeposition in the absence and presence of organic additives are introduced.

(a)

(b)
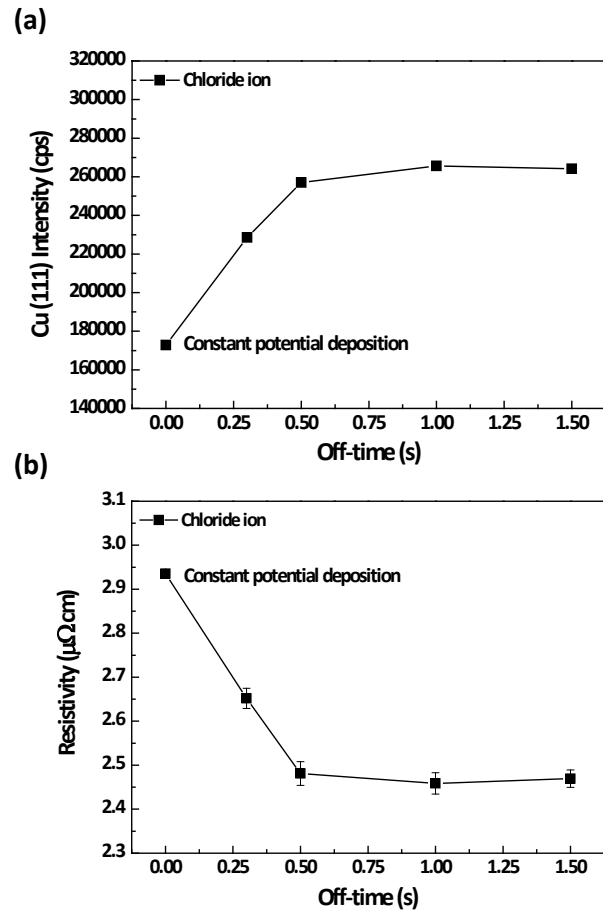
Fig. 3.11. The changes of (a) Cu (111) peak intensity and (b) the resistivity of Cu films

deposited with the addition of Cl⁻.
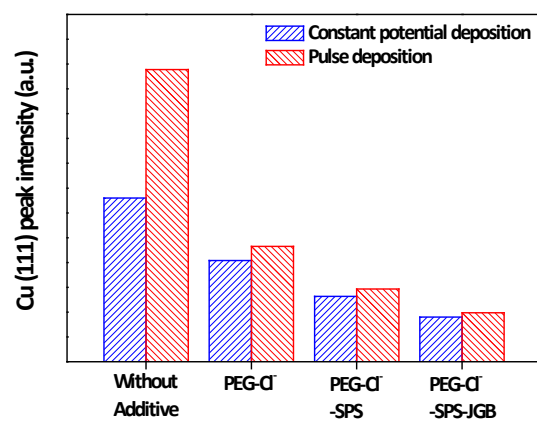
Fig. 3.12. The Cu (111) peak intensities of Cu films deposited by means of constant

potential and pulse electrodeposition with various combinations of organic additives.
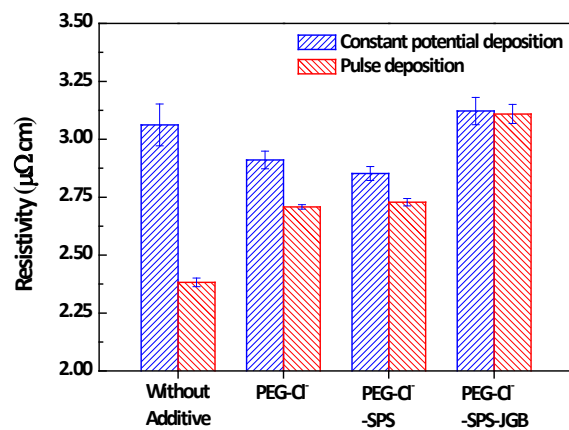
Fig. 3.13. The electrical resistivity of Cu films deposited by means of constant potential and pulse electrodeposition with various combinations of organic additives.

CHAPTER IV

The characteristics of Cu films deposited by pulse-reverse electrodeposition

4-1. Pulse-reverse electrodeposited Cu films in the absence of additives

The anodic charge per unit cycle and dissolution ratio could be used for characterizing pulse-reverse electrodeposition with the ensemble cathodic conditions. The anodic charge is defined as the total amount of passed electrons during the unit anodic step and the dissolution ratio is designated as the ratio between the amounts of the anodic and cathodic charges. Fig. 4.1 depicts the representative current and charge profiles of potentiostatic pulse-reverse electrodeposition as well as the definitions of the amounts of the cathodic and anodic charges. In the absence of organic additives, the amount of cathodic charge under an identical cathodic potential and on-time is nearly constant. Hence, the tendency of the anodic charge and the dissolution ratio are completely identical. Thus, the anodic charge was used to compare the film properties. The anodic charges as functions of the anodic potential and time are exhibited in Fig.

4.2, demonstrating an increasing anodic charge as the reverse time and anodic potential increased. The properties of the Cu film were plotted with not only the anodic potential and reverse time but also the anodic charge to verify the effects of the anodic step.

The crystallographic orientations of Cu films deposited with various anodic potentials and times were evaluated by XRD. The Cu films were composed of (111) only, as shown in the XRD patterns (Fig. 4.3). Similar to the results of pulse electrodeposition, this result was ascribed to the highly (111)-oriented Cu seed layer and relatively thin Cu films. The peak intensity corresponds to the amount of the (111)-oriented planes at an identical thickness. It is important to note that the peak intensity of Cu (111) was obviously affected by the anodic potential and reverse time. More details on the variation of the peak intensity are displayed in Fig. 4.4(a). It is clear that the anodic step enhanced the development of the Cu (111) orientation. However, regardless of the anodic potential, similarity in the overall increment according to the reverse time was observed. Therefore, the intensity was re-plotted as a function of the anodic charge instead of the reverse time in order to clarify the potential dependency and the results are presented in Fig. 4.4(b). This led to conclude that a higher anodic potential was less efficient in developing the (111)-oriented Cu. This can be explained by the 'selectivity' of the anodic step. The Cu deposits could have various energy states originating from

the crystallographic orientation and grain size. The much higher anodic potential, which implies a higher driving force for Cu dissolution, could dominate the energy difference. Therefore, it induced relatively regular dissolution and can be called 'uniform'. In contrast to this behavior, a lower anodic potential preferentially dissolved only the Cu with higher energy, which is referred to as 'selective'. On the basis of the alteration of the peak intensity, it could be deduced that there was selectivity in the anodic step, and the anodic potential played a crucial role in determining the selectivity.

The resistivity of the Cu films was also affected by the anodic potential and time, as shown in Fig. 4.5(a). It was observed that the initial decrease in the resistivity was followed by a reascent as the reverse time increased. No potential dependency of the resistivity was observed analogous to Fig. 4.4(a), and the optimum reverse time showing the lowest resistivity was only apparent within the range from 0.05 to 0.1 s, regardless of the anodic potential. Similar to the Cu (111) peak intensity, the anodic charge enabled the determination of the potential dependency of the resistivity, as displayed in Fig. 4.5(b). The resistivity change was considerably slowed down by the higher anodic potential. This also provides a clear evidence for the selectivity of Cu dissolution. The change rate of the resistivity corresponds to the selectivity determined by the anodic potential. In addition to this, it is important to highlight the fact that the

higher anodic potential shifted the optimum anodic charge towards a larger value. It was also dominated by the selectivity of Cu dissolution, which will be clearly explained in the following section.

Similar to Chapter III, the impacts of phonons, grain boundaries, surfaces, and impurities should be considered to understand the behavior of electrical resistivity.[37-50] For Cu films deposited in a $CuSO_4$ and H_2SO_4-based electrolyte without any organic additives, as in this experiment, the influences of phonons and impurities could be ruled out as major factors. Therefore, the contributions of the grain size and surface roughness should be taken into account in order to clarify the behaviors of the resistivity. Subsequent analyses were performed in an attempt to evaluate these factors.

The peak broadening in the XRD patterns is mainly attributed to the grain size so that Scherrer's equation was used to calculate the relative grain size from the FWHM values.[90,91] It can be predicted that the much smaller grains resulted in a larger value of FWHM. Fig. 4.6(a) shows the changes in the FWHM as functions of the anodic potential and reverse time, clearly indicating the gradual enlargement of grains with increasing anodic charge. No anodic potential dependency was similarly observed with the reverse time, therefore, the anodic charge was employed again instead of the reverse time. It was also revealed that the lower anodic potential was considerably

more efficient in increasing the grain size. This could be associated with the selectivity of the anodic step. As a result of the lower anodic potential, the selectivity of the Cu dissolution was enhanced and the Cu grains thereby significantly increased in size. To complement this experiment, the sizes of grains at the surface were evaluated by BSE and the images are displayed in Figs. 4.7(a)-(d). The results are in agreement with the estimated grain size obtained from the FWHM, revealing gradual enlargement of the grains. The average grain size of Cu deposited by pulse electrodeposition was 97.8 nm, and that from pulse-reverse electrodeposition with reverse times of 0.05, 0.1, and 0.2 s were 110.1, 121.8, and 135.8 nm, respectively. Their size distributions are exhibited in Fig. 4.7(e). On the basis of grain size, it is logical to suggest that the initial reduction in the resistivity, as presented in Fig. 4.5(b), can be explained by the monotonic increment of the grain size. From the viewpoint of the change rates, the similarity in behaviors of the grain size and resistivity also supports that.

  In addition to the grain size, there is also a contribution from the surface roughness to the resistivity. The surface morphologies obtained with different reverse times with an anodic potential of 100 mV are represented in Fig. 4.8. The size of surface protrusions continuously increased due to the anodic charge. This was attributed to selective dissolution during the anodic step in analogy to the enlargement of the grains. The root

mean square (RMS) roughness results are depicted in Fig. 4.9, which clearly indicates

surface roughening by the anodic step. The steeper increment of surface roughness

with the lower anodic potential was ascribed to the more selective dissolution of Cu. It

is interesting to note that the behaviors of the grain size and surface roughness were

similar in regards to their change rate. It can be concluded that this is owing to the

selectivity of the anodic step, which is determined by the anodic potential. Regarding

the resistivity, higher surface roughness, which causes additional electron scattering,

accompanies the increase in the resistivity. Therefore, this led us to deduce that the

reascension of the resistivity above the optimum anodic charge is attributable to the

surface roughness. This was also supported by the similar tendency of the change rate

as a function of the anodic potential.

 On the basis of the grain size and surface roughness, it is more natural to deduce that

the resistivity behavior was dominated completely by the conflict between these factors.

In other words, at the optimum anodic charge revealing the lowest resistivity, their

influences on the increment of the resistivity were minimized. It is important to

accentuate that the surface roughness at the optimum anodic charge was about 4 - 5 nm

regardless of the anodic potential, which suggests that the surface roughness influences

the resistivity considerably more when it is over 5 nm. This was only valid for a film

thickness of about 150 nm because the effect of surface roughness is influenced by the thickness. The change rate of the resistivity shown in Fig. 4.5(b) can also be explained by the grain size and surface roughness. To complement the qualitative explanation, a theoretical approach was attempted to understand the behavior of resistivity in terms of the grain size and surface roughness. This approach used Kuan's formalism, presented in the following equation,[39]

$$\frac{\rho}{\rho_0} \approx 1 + 0.375(1-p)\frac{S\lambda}{t} + 1.5\left(\frac{R}{1-R}\right)\frac{\lambda}{d} \tag{3.1}$$

where ρ is the film resistivity, ρ_0 is the bulk resistivity, p is a scattering parameter between 0 and 1, S is a roughness factor greater than 1, λ is the electron mean free path (39 nm for Cu), t is the thickness of the film, R is the scattering coefficient for the grain boundary (approximately 0.3 for Cu), and d is the average grain size. Note that the surface roughness affects the values of p and S, however, it is hard to experimentally assess their effects.[39,92] Hence, this formalism can be applied to these results with three methods: (1) changing S with constant p, (2) changing p with constant S, and (3) changing both p and S. To simplify the simulation, it was also assumed that the inverse of FWHM and surface roughness were linearly dependent on the dissolution amount.

Fig. 4.10 represents the change rate of surface roughness and the inverse of FWHM according to the anodic potentials measured from Figs. 4.6 and 4.9. In this approach, the resistivity from pulse electrodeposition (initial resistivity in Figs. 4.5 and 4.11) was first matched to the calculated value for finding the appropriate the values of p and S, and the curve from the formalism was matched to the experimental results at 150 mV by determining the appropriate change rate of S. It was followed by substitution of the change rates according to the anodic potential shown in Fig. 4.10. Regardless of the aforementioned methods in the simulation, the simulated curves greatly predicted the behaviors including the optimum anodic charge and the change rate of resistivity, however, the ranges of p and S were only varied according to the methods. The representative results obtained with methods (1) and (2) are shown in Fig. 4.11. Since the only variables are the change rates of the grain size and surface roughness depending on the anodic charge and potential, it can be concluded that the resistivity variation was originated from the conflict between the effects of the grain size and surface roughness.

In brief, pulse-reverse electrodeposition led to a 9% reduction of the resistivity and 50% enhancement of Cu (111) formation at the optimum amount of anodic charge. The anodic step gave rise to enlargement of the Cu grains and enhanced the development of

Cu (111). It was deduced that the anodic potential determined the selectivity of the anodic step, resulting in much steeper changes in the film properties with a lower anodic potential. It was revealed that the lowest resistivity at the optimum anodic charge was originated from the conflict between the effects of grain size and surface roughness, which was also supported by the results of the theoretical approach. Based on this, the pulse-reverse electrodeposition in the presence of PEG-Cl$^-$-SPS was performed, and the results are introduced in the next section.
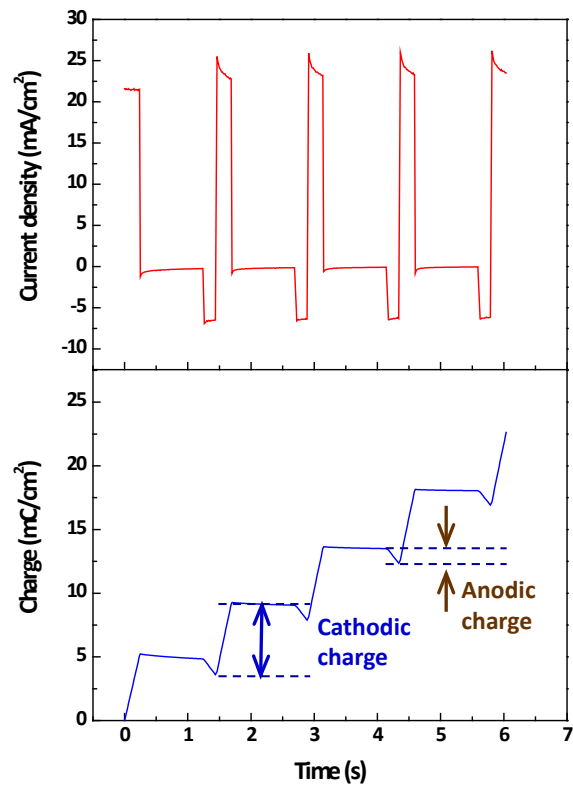
Fig. 4.1. The representative profiles of current density and charge during the potentiostatic pulse-reverse electrodeposition, and the definitions of cathodic and anodic charge per unit cycle.
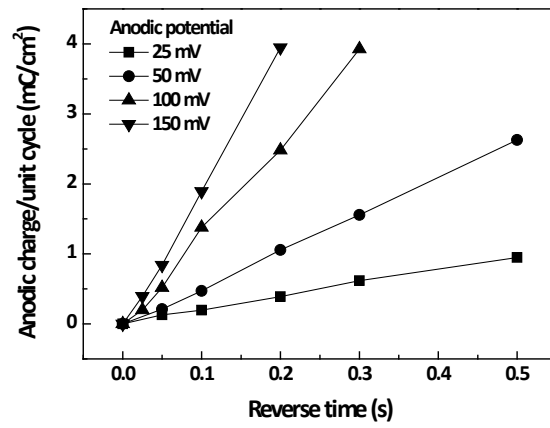
Fig. 4.2. The anodic charges according to the anodic potentials and reverse times.
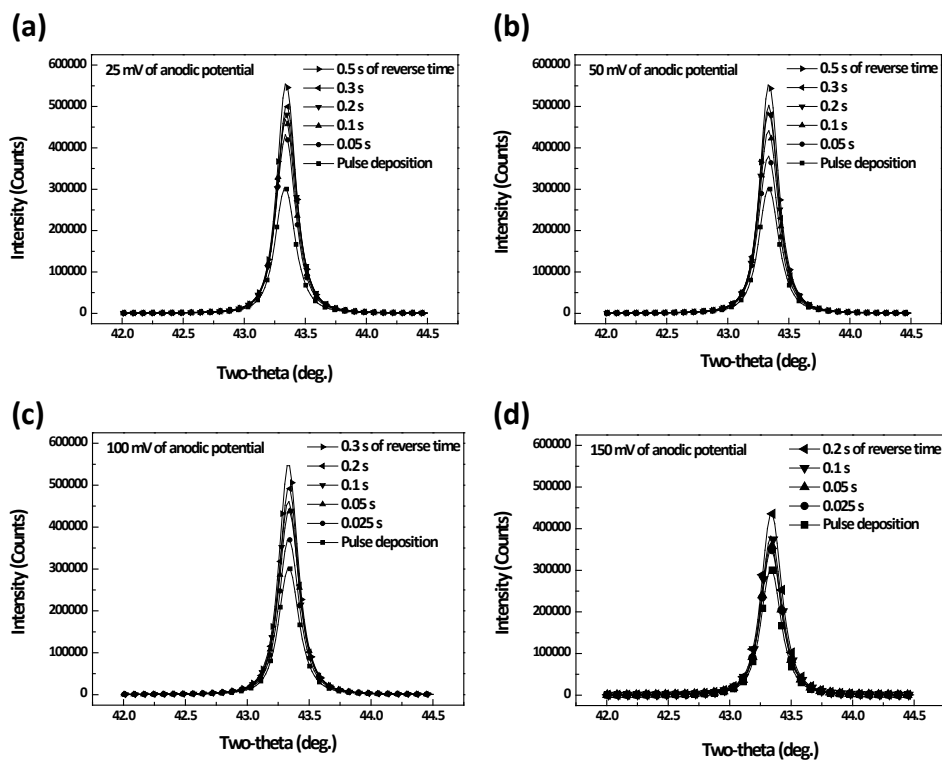
Fig. 4.3. XRD patterns of Cu films deposited with (a) 25 mV, (b) 50 mV, (c) 100 mV, and (d) 150 mV of anodic potentials.

(a)

(b)
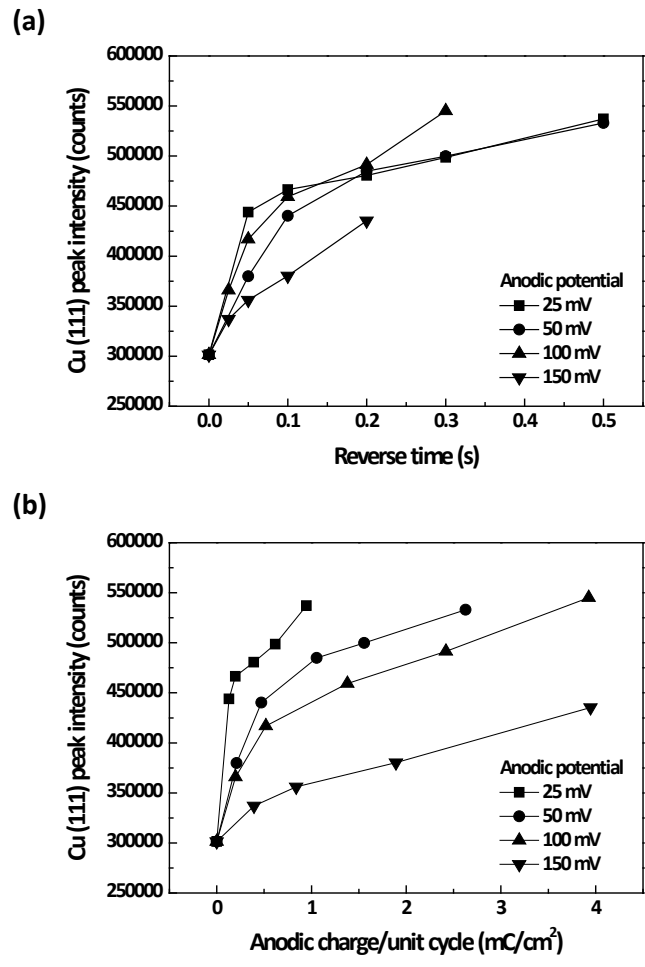
Fig. 4.4. (a) Cu (111) peak intensities of each XRD patterns as a function of the anodic potential and reverse time, and (b) re-plotted results with the anodic charge per unit cycle as the x-axis instead of the reverse time.
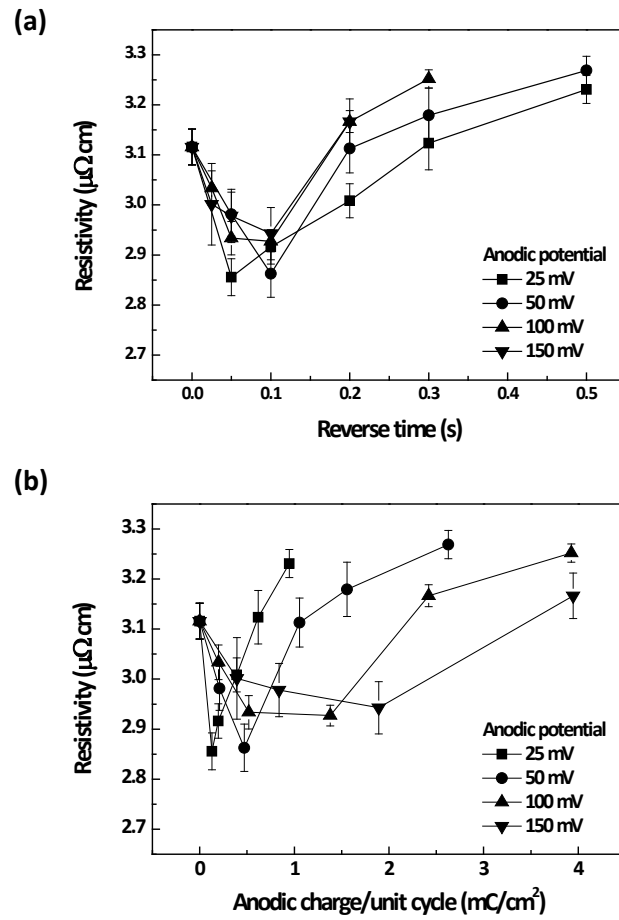
Fig. 4.5. The changes in the resistivity of Cu films according to the anodic potential and reverse time, and (b) re-plotted results with the anodic charge per unit cycle as the x-axis instead of the reverse time.

(a)

(b)
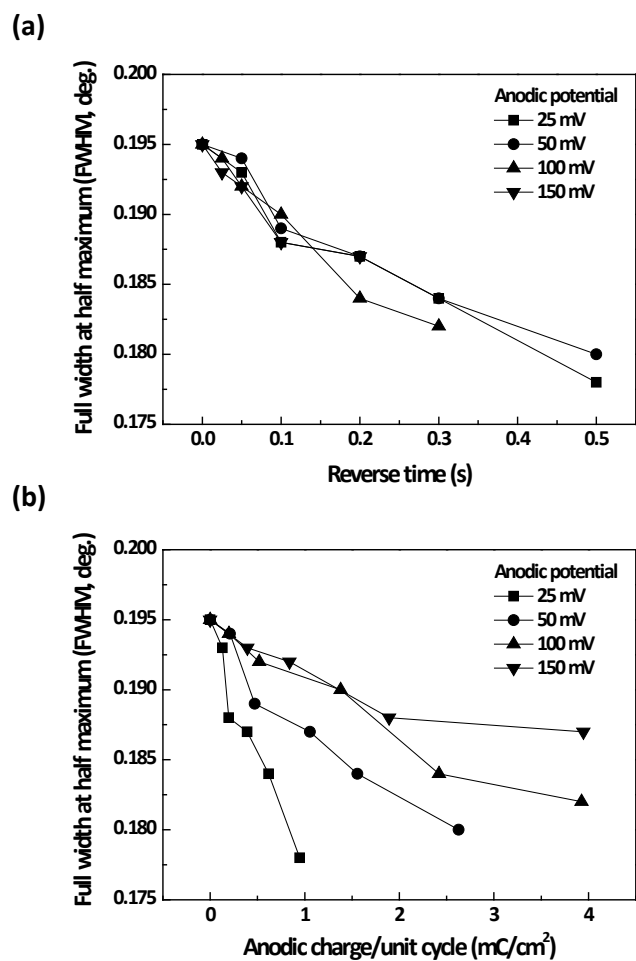
Fig. 4.6. (a) The behaviors of FWHM of Cu (111) peak from XRD patterns as a function of anodic potential and reverse time, and (b) re-plotted results with the anodic charge per unit cycle as the x-axis instead of the reverse time.
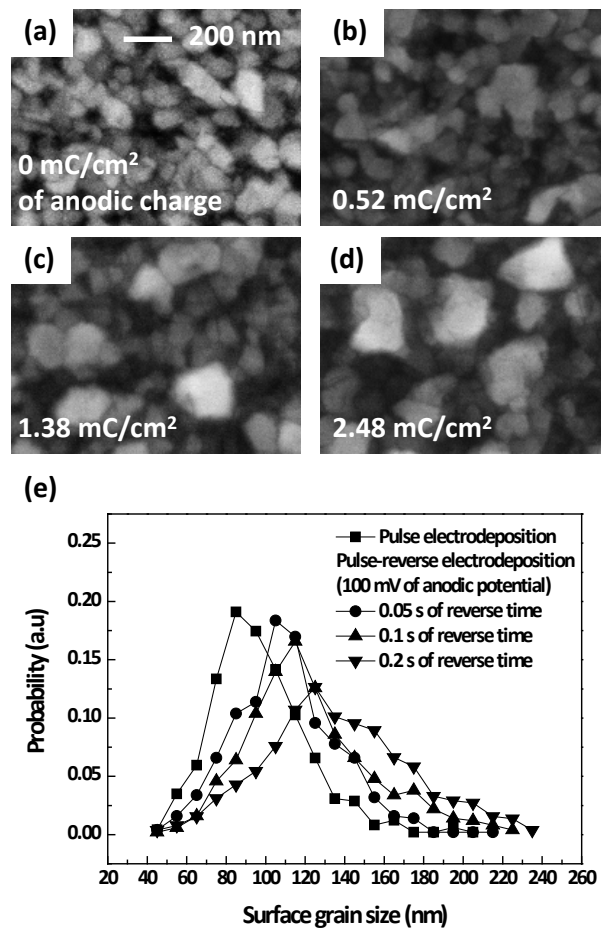
Fig. 4.7. BSE images of the Cu surface deposited by (a) pulse electrodeposition, and pulse-reverse electrodeposition with (b) 0.05 s, (c) 0.1 s, and (d) 0.2 s of reverse time, and (e) the distribution of surface grain size; the anodic potential was 100 mV with respect to OCP.
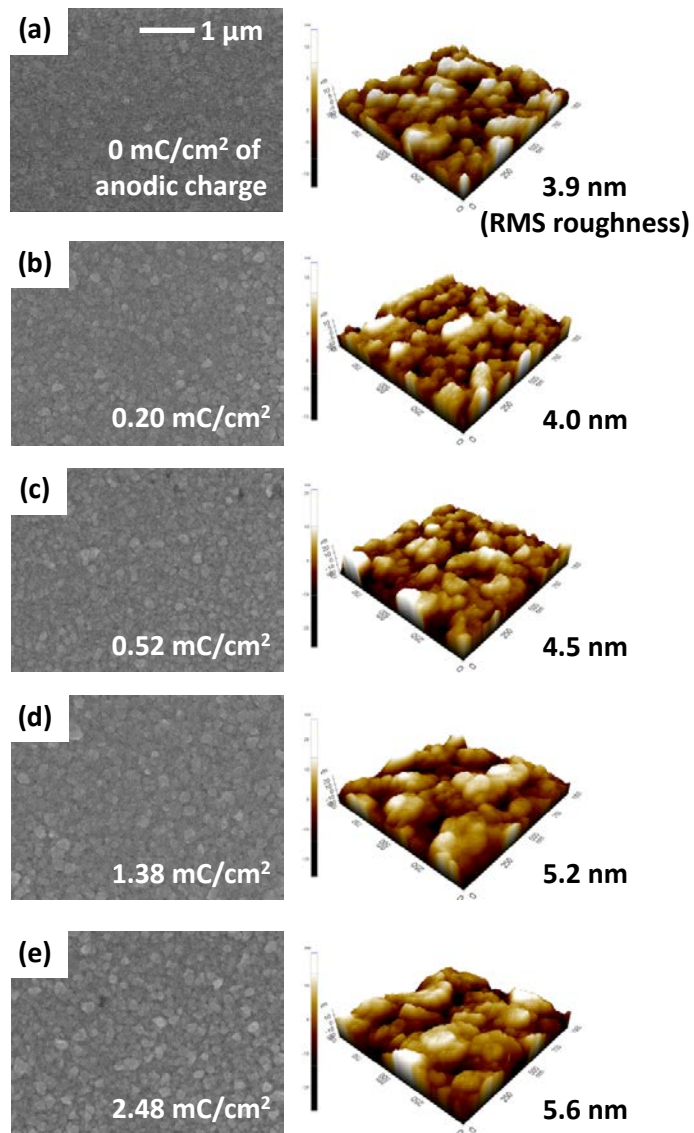
Fig. 4.8. Surface morphologies of Cu films deposited by (a) pulse electrodeposition, and pulse-reverse electrodeposition with (b) 0.05 s, (c) 0.1 s, (d) 0.2 s, and (e) 0.3 s of reverse time; the anodic potential was 100 mV (vs. OCP).
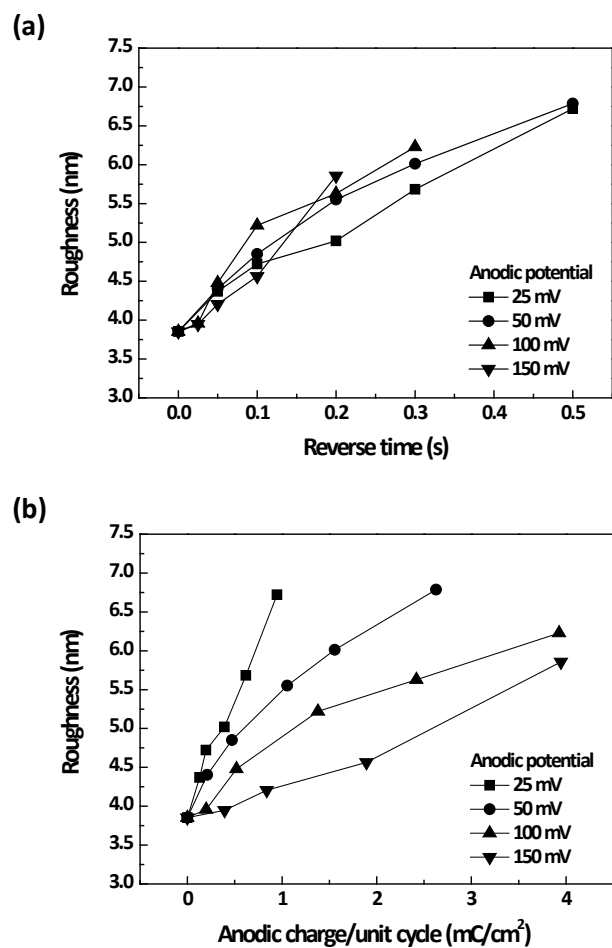
Fig. 4.9. (a) The changes in RMS surface roughness of Cu films according to the anodic potential and reverse time, and (b) re-plotted results with the anodic charge per unit cycle as the x-axis instead of the reverse time.
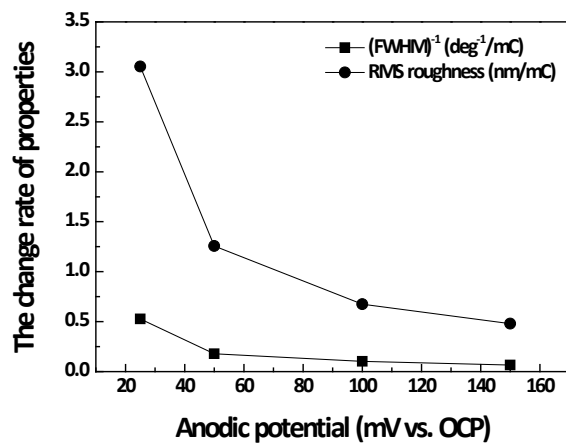
Fig. 4.10. The increasing rates of $(FWHM)^{-1}$ and surface roughness according to the anodic potential.

(a)

(b)
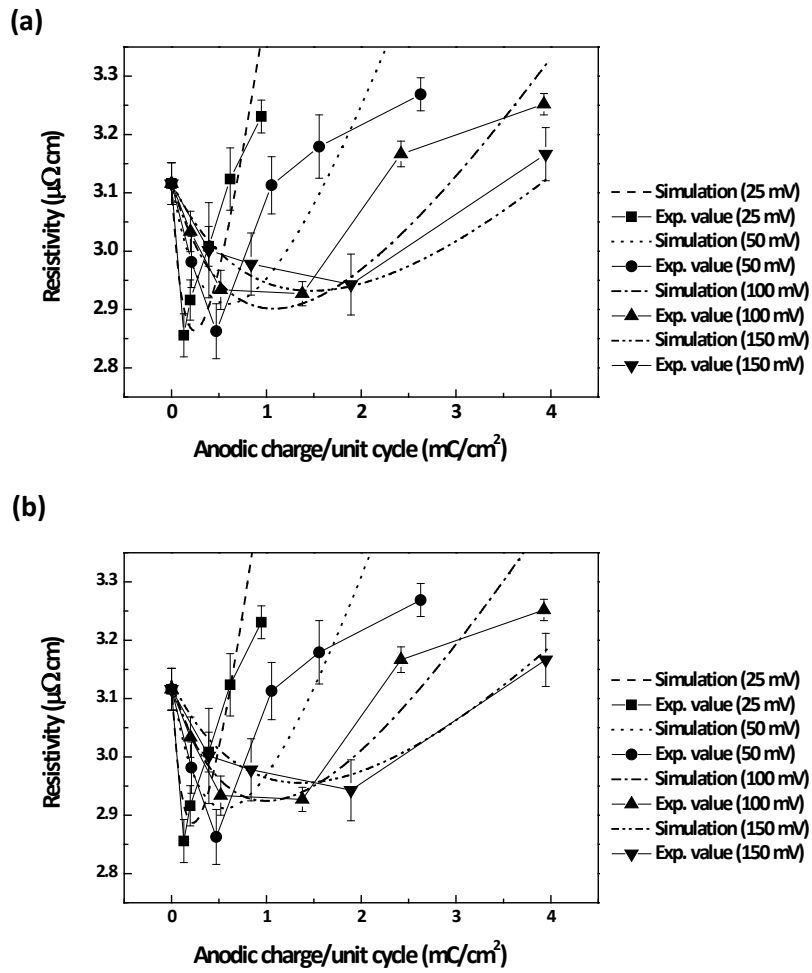
Fig. 4.11. The comparison of experimental and simulation results from changing only

(a) roughness factor (S) and (b) scattering parameter (p), respectively.

4-2. Pulse-reverse electrodeposited Cu films in the presence of additives

As mentioned above, the tolerance of Cu against the anodic step could be determined by the energy difference originating from the crystallographic orientation (surface energy) and the grain size (grain boundary energy) in the absence of the organic adsorbates. However, when organic additives, such as PEG-Cl$^-$ and SPS, are added into the electrolyte, this tolerance could depend on the kinds of adsorbates. Before clarifying the influences of the anodic step and organic additives on the film properties, LSV was attempted to investigate this change in the tolerance against the anodic potential, which is shown in Fig. 4.12(a). It can be seen that the anodic currents ascended in the following order: PEG-Cl$^-$, PEG-Cl$^-$-SPS, without additives, Cl$^-$, SPS, and SPS-Cl$^-$. This implies that the SPS-covered Cu could be preferentially dissolved by the anodic step as compared to PEG-Cl$^-$-covered Cu. The large anodic current in the case of PEG-Cl$^-$-SPS compared to the PEG-Cl$^-$ case in the potential range from 100 to around 280 mV indicates the preferential dissolution of SPS-covered Cu, followed by subsequent dissolution of PEG-Cl$^-$-covered Cu. This was also supported by the additional experiments varying initial potential of LSV as shown in Fig. 4.12(b), which

revealed an increase of anodic current in the potential range between around 100 and 280 mV as the initial potential was negatively shifted. Since the application of more negative potential reduced the stability of PEG-Cl$^-$, therefore, this current increment was ascribable to more adsorption of SPS. This sequential dissolution during LSV means that the selectivity of Cu dissolution could be determined by either the SPS or PEG-Cl$^-$ adsorbates, and the Cu covered by SPS could be preferentially dissolved relative to Cu covered by PEG-Cl$^-$.

Similar to the anodic behavior, the additives also alter the cathodic deposition as clearly indicated in previous studies.[13,28,32,34] Therefore, it might be more clear to use the dissolution ratio as a variable instead of the anodic charge, since it contains the effects of the additives on both the anodic and cathodic currents. The dissolution ratio can be defined by the equation (1.13). The definitions of the anodic and cathodic charges are the total amounts of passed electrons during the unit reverse and on-times, respectively. The dissolution ratio in the presence of PEG-Cl$^-$-SPS is depicted in Fig. 4.13, showing a monotonic increment of the dissolution ratio as the anodic potential and reverse time is increased. These values were employed to investigate the potential dependency of the film properties. Similar to the previous study, it was apparent that the usage of the dissolution ratio was much more effective in characterizing the anodic

step as opposed to reverse time.

The electrodeposited thin Cu film (~150 nm) mainly consisted of (111) orientation because of the highly-oriented Cu seed layer confirmed in the XRD patterns. The thickness of the Cu films were precisely controlled, thus the peak intensity corresponds to the amount of (111)-orientated Cu. The changes in the peak intensity according to the reverse times are exhibited in Fig. 4.14(a), and clearly indicate the gradual increment of the intensity as the dissolution ratio becomes large. When the dissolution ratio was adopted as the x-axis instead of reverse time, no apparent potential dependency was observed, except for a slightly faster increase in the case of 25 mV in contrast to the case without additives. This implies that the presence of the additives might offset the effect of surface energy from the crystal orientation. Based on these results, it is logical to suggest that the influence of the anodic step on the film properties should be understood in terms of the adsorbates and their effects.

The resistivities of the Cu films with various anodic steps are presented in Fig. 4.15(a), indicating the existence of the optimum reverse time showing the lowest resistivities which were in the range between 0.25 s and 0.1 s. In order to clarify the anodic potential dependency, the dissolution ratio was adopted instead of the reverse time. Fig. 4.15(b) represents the resistivity behavior according to the dissolution ratio,

revealing the dissolution ratios with the lowest resistivities, which are referred to as the optimum dissolution ratio. It was obvious that the optimum dissolution ratios were shifted to larger values as the anodic potential was increased. As mentioned above, the resistivity of a metal thin film is affected by various factors, such as phonons, grain size, surface roughness, and the concentration of impurities.[37-50] For the conditions examined in this study, the influence of phonons is unchanged. As for impurities, it was reported that the incorporation of organic additives was dependent on the cathodic current, the amounts of which were reduced by pulse-reverse electrodeposition.[75,93,94] The resistivity increment resulting from the influence of the impurities can be described by the following equation: $f = C \cdot 4 + N \cdot 7 + O \cdot 5.5 + S \cdot 9$, where f is the total effect of dopants ($\mu\Omega \cdot cm/atom\%$) on the resistivity increment; and C, N, O, and S are the atomic concentrations of incorporated carbon, nitrogen, oxygen, and sulfur atoms, respectively.[51] In the previous research with an identical additive combination, the concentration of carbon atoms was below 0.02 wt%, and the nitrogen and sulfur atoms were not detected based on the results from the elemental analyzer.[24] Thus, it was apparent that the impact of the impurities on the resistivity can be neglected. Therefore, it is natural to conclude that the grain size and surface roughness were the major factors for resistivity changes.

The grain size was estimated from the FWHM of the Cu (111) peak using Scherrer's equation, which gives that the reduction in the FWHM implies an increment of the grain size.[90,91] The FWHM values as a function of the anodic potential and reverse time are displayed in Fig. 4.16(a), demonstrating an initial reduction of grain size followed by re-growth. This was not sufficient to characterize the impact of pulse-reverse electrodeposition, therefore, the dissolution ratio was adopted again, and the results are shown in Fig. 4.16(b). As represented in Fig. 4.16(b), the application of more positive anodic potential showed the sluggish change of grain size, and the maximum values of FWHM were also shifted to lower values. In addition to this, the sizes of the surface grains were measured from BSE images, as can be seen in Figs. 4.17(a) to (d), which supports the aforementioned behavior of grain size estimated from the FWHM. The average sizes of the surface grains were 73.4 nm from pulse electrodeposition, and 65.6, 86.7, and 96.4 nm from pulse-reverse electrodeposition, with 0.05, 0.2, and 0.3 s of reverse time, respectively. The size distributions are depicted in Fig. 4.17(e).

In the case of additive-free electrolyte, the grain size was gradually increased with more anodic charge (e.g. the minimum grain size was seen at 0 mC of anodic charge). In contrast, in the presence of the additives, the minimum grain size was distinctively observed at a non-zero anodic charge. This was ascribable to the effects of the anodic

step and the additives. The addition of the organic additives generally reduces the grain size, which was confirmed in the previous results (pulse electrodeposition: 97.8 nm without additives16 vs. 73.4 nm with additives). The anodic step seemed to enhance this grain size reduction, consequently resulting in the smallest grain size at a certain dissolution ratio. In Fig. 4.18, it was observed that FWHM of the Cu film deposited in the electrolyte containing only SPS-Cl$^-$ was lower compared to Cu film deposited with PEG-Cl$^-$. Since the inverse of FWHM implied the grain size, the grain size of Cu film deposited in the electrolyte containing only SPS-Cl$^-$ was significantly larger than that containing only PEG-Cl$^-$. It was already confirmed that the Cu grains covered by a relatively large amount of SPS could be preferentially dissolved as compared to PEG-Cl$^-$, which is shown in Fig. 4.12. Combining these two results enables us to suggest that the larger grains growing with relatively more SPS could be preferentially dissolved during the anodic step because of selective dissolution, finally resulting in a reduction of total grain size. The magnitude of the selectivity could be governed by the anodic potential, so a lower anodic potential could considerably increase the selectivity even more, which led to a shift of the optimum dissolution ratio towards a lower value as the anodic potential decreased. In contrast, for dissolution ratios above the ratio showing the minimum grain size, it was observed that the grain size was monotonically

augmented again with accelerated rates and much lower anodic potential. This seemed to be due to the relatively large dissolution amount diminishing the effect of the additives. Therefore, the behavior of the grain size above the minimum value could be understood as in the additive-free condition. This was supported by the identical behaviors of the resistivity, grain size, and surface roughness between the cases with and without additives in the range over the optimum dissolution ratio. That is, there are two phenomena from the anodic step: (i) below the optimum dissolution ratio, where the selective dissolution of Cu covered by SPS occurs, and (ii) above the optimum dissolution ratio, where the diminishment of the additive effect occurs.

In regard to the resistivity, the reduction of grain size is an increasing factor that provides additional probability of electron scattering.[37-46] However, the behaviors of the grain size, represented in Figs. 4.16 and 4.17, enable us to expect the exact opposite trend to the experimental results shown in Fig. 4.15. Therefore, it can be concluded that the grain size is a minor factor in determining the resistivity in the case of the electrolyte with additives.

The representative FESEM and AFM images of the Cu surfaces are presented in Fig. 4.19, and reveal that the surface was not roughened significantly with respect to lower reverse time values until 0.1 s, above which a severe increase in surface roughness can

be seen. In the results without additives, the surface was monotonically roughened with increasing anodic charge, which is dissimilar to this result. The values of RMS roughness are shown in Fig. 4.20(a) and (b), demonstrating the optimum reverse time and dissolution ratio with the lowest surface roughness. The anodic potential dependency was clearly observed with the dissolution ratio again. In Fig. 4.21, the surface roughness of Cu film deposited in electrolyte containing only SPS-Cl⁻ was much larger than that with PEG-Cl⁻. Similar to grain size behavior, anodic steps below the optimum dissolution ratio resulted in the reduction of surface roughness by the selective dissolution of Cu covered by SPS. Note that the optimum dissolution ratios showing the lowest resistivity were exactly identical to the ratios with the lowest roughness and smallest grains. The selectivity of the lower anodic potential was much larger; consequently, there were much steeper changes in the surface roughness. It was also logical to deduce that the reincrement of the roughness over the optimum dissolution ratio was attributed to the diminishment of additive effects by the relatively large amount of dissolution. Considering the roughness in terms of resistivity provides reasonable evidence that the resistivity of these films was mainly attributed to the surface roughness, because their tendencies depending on the dissolution ratio were nearly identical in regard to the optimum dissolution ratios and their rates of change. It

is well-known that rough surfaces result in the increment of resistivity due to increased scattering of electrons.[37-50] This is also supported by the fact that roughness could be a decisive factor in determining the resistivity when RMS roughness is over 4 - 5 nm (with 150 nm of film thickness) with additive-free electrolyte.

On the basis of these results, it was clearly confirmed that pulse-reverse electrodeposition in the presence of organic additives led to a 14% reduction of resistivity at the optimum dissolution ratio compared to the optimum condition of pulse electrodeposition. The types of adsorbates were found to play the important roles in the selectivity of the anodic step. It was observed that SPS-covered Cu was much more preferentially dissolved relative to PEG-Cl$^-$-covered Cu. Since the adsorption of SPS increases the surface roughness and the grain size, selective dissolution could result in a reduction of these qualities below the optimum dissolution ratio. Over the optimum, the relatively large amount of dissolution seems to offset the effect of additives, leading to the ensemble behavior with additive-free electrolyte. Since the advantage of pulse-reverse electrodeposition in the absence and presence of organic additives in the aspect of properties is clearly confirmed, the superfilling performance based on the impact of anodic step on the competitive adsorption between PEG-Cl$^-$ and SPS should be clarified. The investigation on the impacts of anodic step on both adsorption state

and superfilling performance is introduced in the next chapter.

(a)

(b)
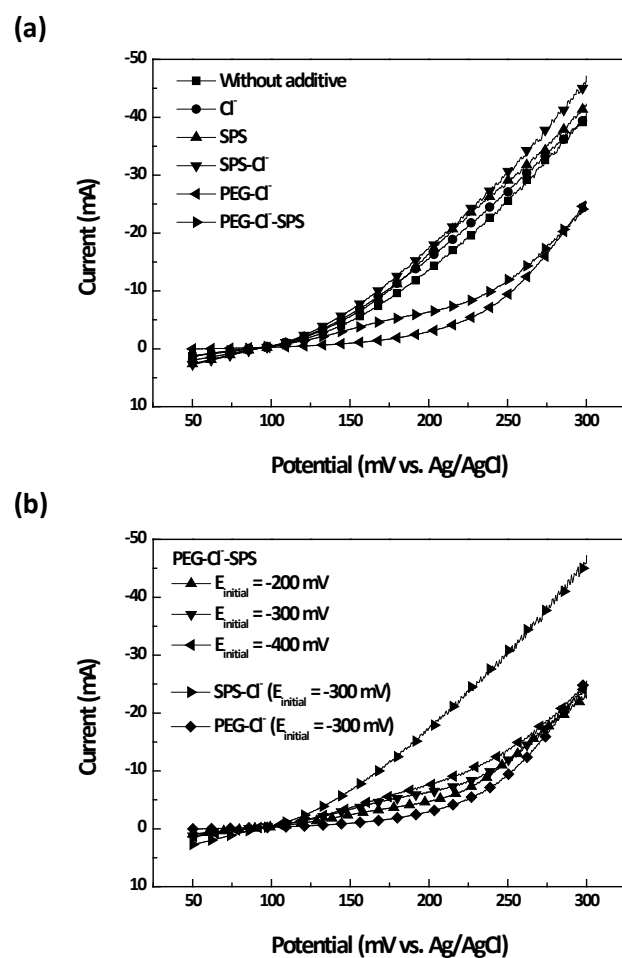
Fig. 4.12. (a) LSV exhibiting the anodic currents in the electrolytes without additives, and containing Cl⁻, SPS, SPS-Cl⁻, PEG-Cl⁻, and PEG-Cl⁻-SPS, and (b) LSV with various initial potentials in PEG-Cl⁻-SPS-added electrolyte.
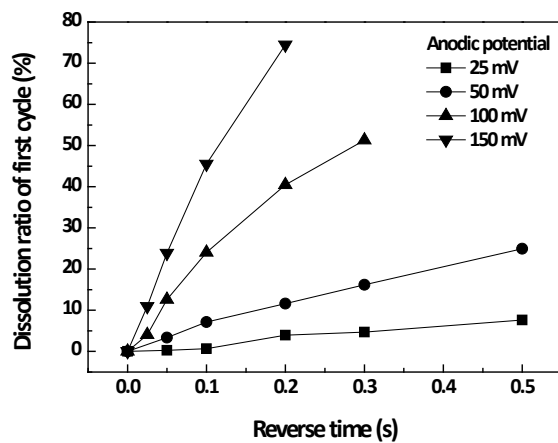
Fig. 4.13. Dissolution ratios with various conditions of anodic step in the presence of

PEG-Cl⁻-SPS.
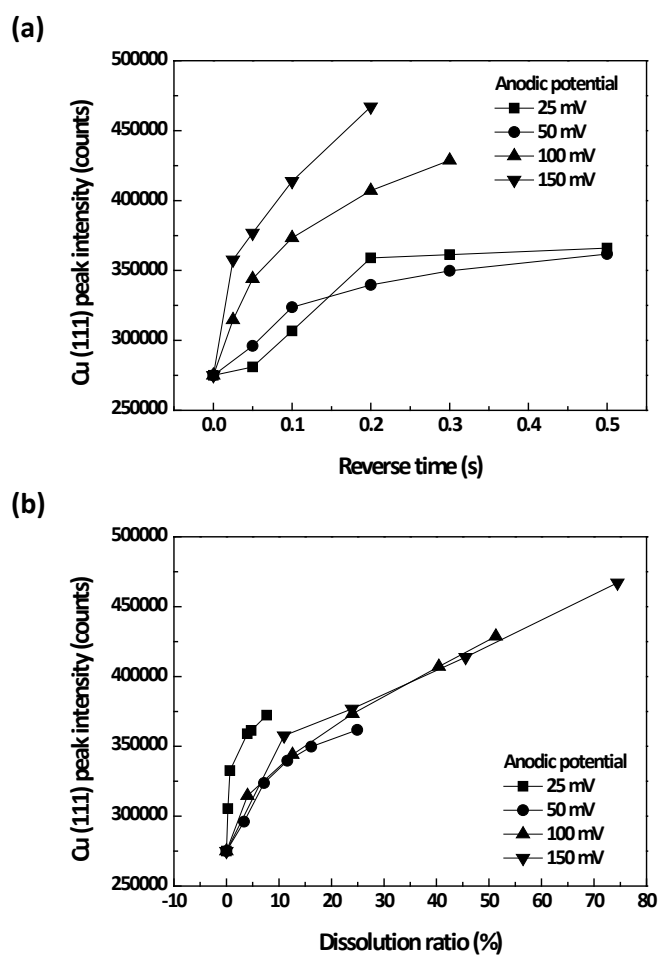
Fig. 4.14. (a) Cu (111) peak intensities according to the reverse time and anodic potential, and (b) re-plotted results with the dissolution ratio as the x-axis instead of the reverse time.
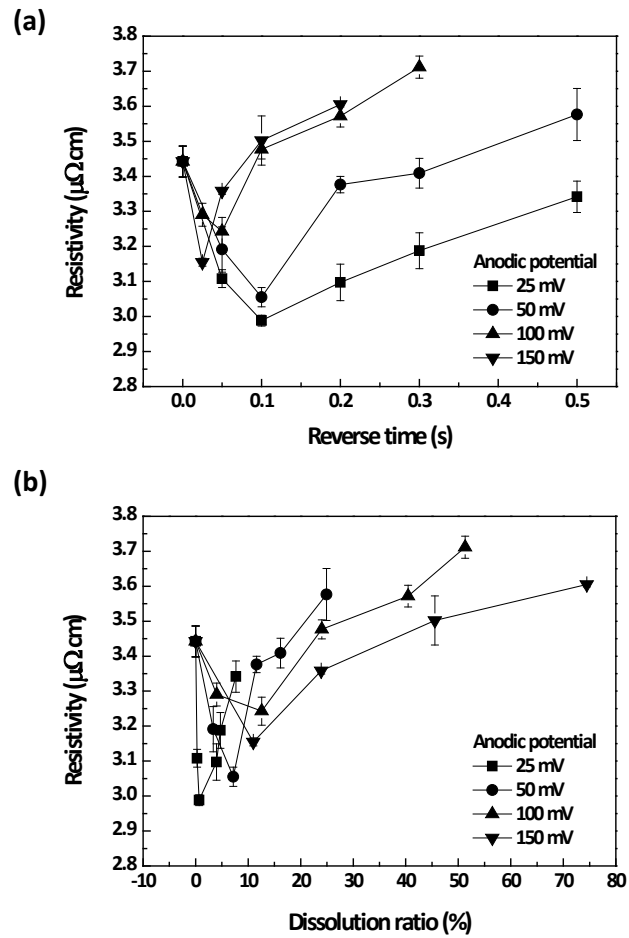
Fig. 4.15. (a) The behavior of resistivity as a function of anodic potential and reverse time, and (b) re-plotted results with the dissolution ratio as the x-axis instead of the reverse time.
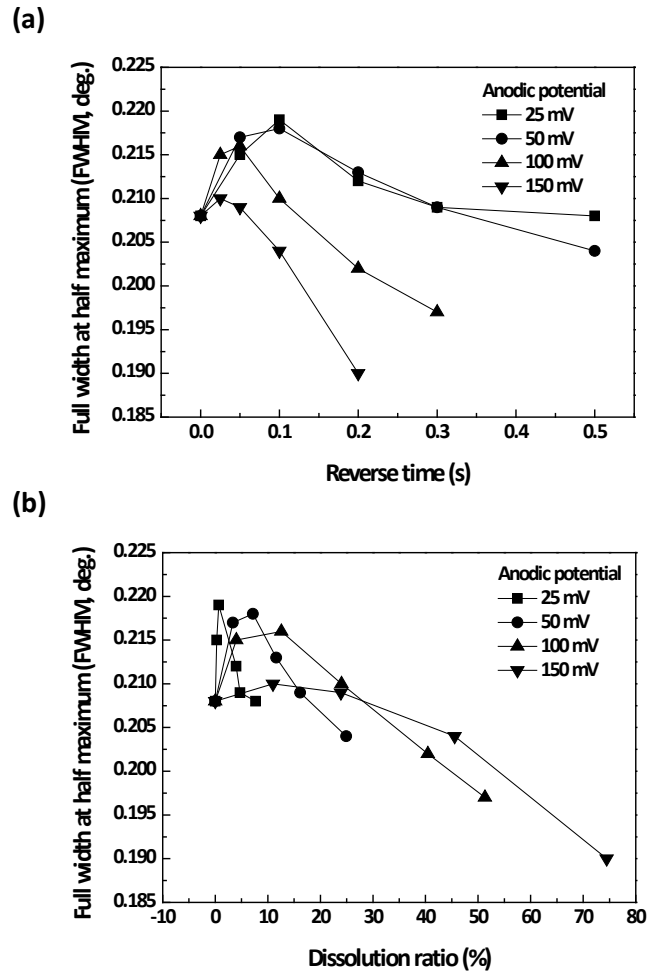
Fig. 4.16. (a) The changes in FWHM of Cu (111) peak according to the anodic potential and reverse time. and (b) re-plotted results with the dissolution ratio as the x-axis instead of the reverse time.
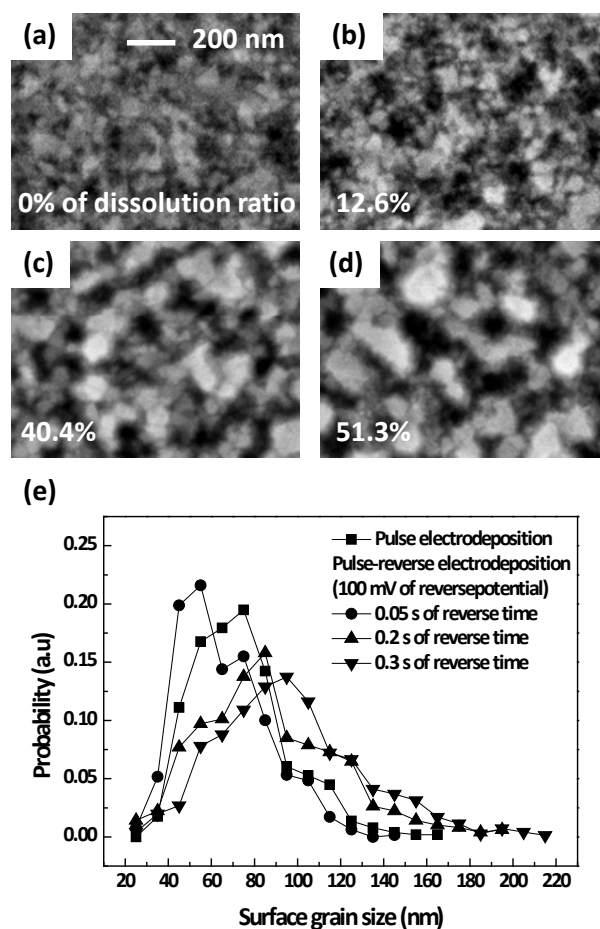
Fig. 4.17. BSE images of Cu films deposited by (a) pulse electrodeposition, and pulse-reverse electrodeposition with (b) 0.05 s, (c) 0.2 s, and (d) 0.3 s of reverse time, and (e) their size distributions of the surface grains; the anodic potential was 100 mV (vs.OCP).
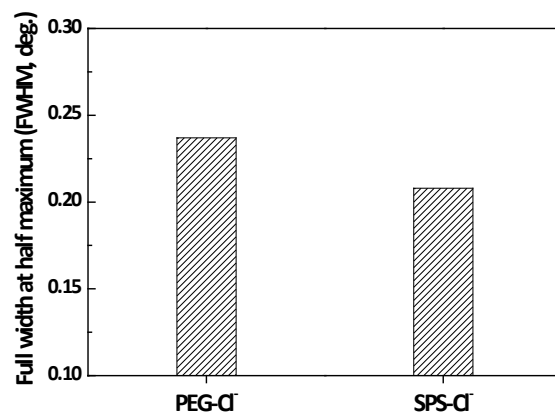
Fig. 4.18. FWHM of Cu (111) peak from Cu films deposited in the electrolyte containing only PEG-Cl$^-$ and SPS-Cl$^-$.

(a)
1 µm
0%: dissolution ratio
5.3 nm
(RMS roughness)

(b)
12.6%
5.1 nm

(c)
24.0%
6.7 nm

(d)
40.4%
10.3 nm

(e)
51.3%
11.0 nm
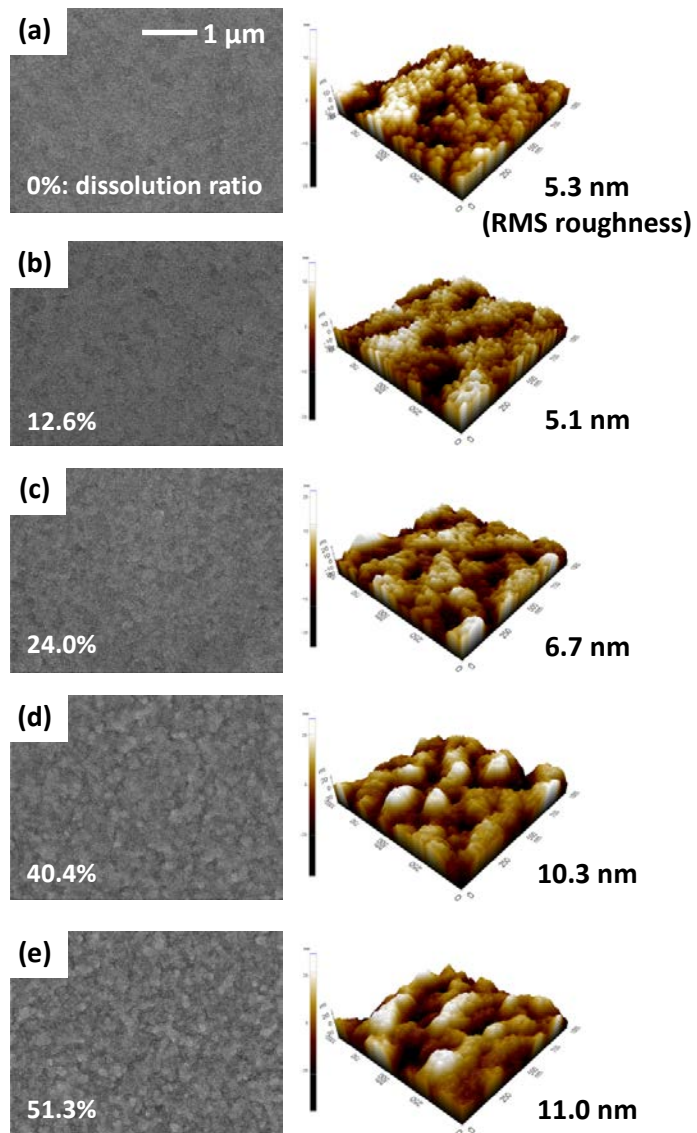
Fig. 4.19. Surface morphologies of Cu films deposited by (a) pulse electrodeposition, and pulse-reverse electrodeposition with (b) 0.05 s, (c) 0.1 s, (d) 0.2 s, and (e) 0.3 s of reverse time; the anodic potential was fixed at 100 mV (vs. OCP).

(a)

(b)
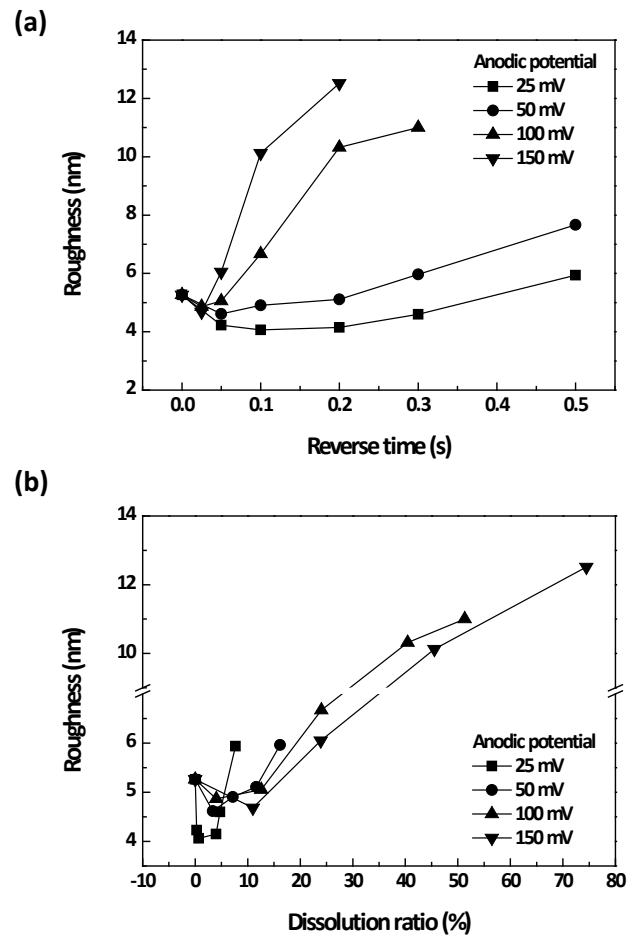
Fig. 4.20. (a) The behavior of RMS roughness according to the anodic potential and reverse time, and (b) re-plotted results with the dissolution ratio as the x-axis instead of the reverse time.
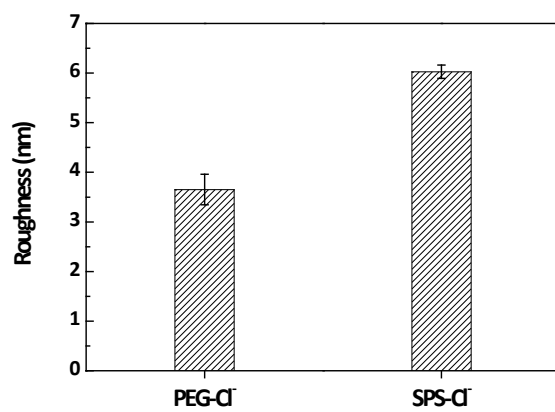
Fig. 4.21. Surface roughness of Cu films deposited in the electrolyte containing only

PEG-Cl⁻ and SPS-Cl⁻.

CHAPTER V

The impacts of anodic step on the adsorption of additives and superfilling

5-1. The effects of anodic step on the competitive adsorption of additives

The representative current profile of potentiostatic pulse-reverse electrodeposition in the presence of PEG-Cl⁻-SPS is shown in Fig. 5.1(a) (saw tooth-like line), which was from the iteration of -200 mV for 0.25 s and 50 mV for 0.1 s. The current peaks at every starting point of cathodic and anodic steps were from the charging and discharging of the double layer and the concentration changes of Cu ions near the electrode by repeated consumption and replenishment. To exclude the effects of double layer and concentration differences, the points at the ends of every cathodic step (denoted as stars in the figure) were collected and re-plotted to simplify the overall current profile.

The simplified current profile accumulated for 140 s is presented in Fig. 5.1(b). As shown in the figure, the cathodic current was sharply increased at the initial stage

followed by the saturation after 100 s. This behavior is very similar to the conventional chronoamperometric behavior of constant potential with PEG-Cl⁻-SPS. The increment of current was related to the displacement of preadsorbed PEG-Cl⁻ by SPS. To quantify this, the saturation current and time were defined from the tangential line, marked as (i) and (ii), respectively. at the contact point between the current profile and a straight line, which were marked as (i) and (ii), respectively. The initial displacement rate of SPS was defined as the initial slope of current increment, marked as (iii). All of the current profiles from constant potential and pulse-reverse electrodeposition were characterized in the same manner.

From the saturation currents measured from the cathodic current profiles, the surface coverage (θ) of SPS can be calculated using the following equation:[13]

$$i(\theta, \eta) = \frac{C_{Cu^{2+}}}{C_{Cu^{2+}}^{\infty}} [k_{PEG}(1 - \theta) + k_{SPS}\theta] \tag{4.1}$$

where $C_{Cu^{2+}}$ and $C_{Cu^{2+}}^{\infty}$ are the surface and bulk concentrations, and k_j is the adsorption rate constant of j species. The ratio of concentrations can be obtained from the ratio of deposition and limiting currents,[95]

$$\frac{C_{Cu^{2+}}}{C^{\infty}_{Cu^{2+}}} = 1 - \frac{i}{i_L} \qquad\qquad (4.2)$$

where i_L is the limiting current and i is the deposition current. In addition, the adsorption rate constant (k_j) could be measured from the chronoamperometry in the electrolyte only containing PEG-Cl⁻ or SPS (or SPS-Cl⁻ revealing the similar results). Combining two equations, the situations with only PEG-Cl⁻ (θ=0) or SPS (θ=1) can be described by the following equations which were from equations (4.1) and (4.2):

$$i_{PEG-Cl^-} = \left(1 - \frac{i_{PEG-Cl^-}}{i_L}\right) k_{PEG-Cl^-} \qquad\qquad (4.3)$$

$$i_{SPS} = \left(1 - \frac{i_{SPS}}{i_L}\right) k_{SPS} \qquad\qquad (4.4)$$

where i_{PEG-Cl^-} and i_{SPS} are the currents from the chronoamperometries in the electrolytes only containing PEG-Cl⁻ and SPS, and it provides the adsorption rate constant as the function of measured current and the limiting current. To calculate this, the chronoamperometries with various overpotentials were performed, and the current profiles and average currents were displayed in Figs. 5.2(a) and (b). Taking the aforementioned equations together, the surface coverage of SPS can be expressed using the terms of currents:

$$\theta = \frac{\left(\dfrac{i(\theta,\eta)}{i_L - i(\theta,\eta)} - \dfrac{i_{PEG-Cl^-}}{i_L - i_{PEG-Cl^-}}\right)}{\left(\dfrac{i_{SPS}}{i_L - i_{SPS}} - \dfrac{i_{PEG-Cl^-}}{i_L - i_{PEG-Cl^-}}\right)} \qquad (4.5)$$

where $i(\theta,\eta)$ is the experimentally measured current from the constant potential and pulse-reverse electrodeposition. i_{PEG-Cl^-} and i_{SPS} were employed from Fig. 5.2(b) and i_L of these experimental conditions was 26.6 mA measured from linear sweep voltammetry. Unfortunately, since the limiting current was changed by the conditions of pulse-reverse electrodeposition, the surface coverage from pulse-reverse electrodeposition could not be exactly calculated. Therefore, the cathodic potential was only determined by this calculation, and the saturation current was investigated with various conditions of pulse-reverse electrodeposition.

  Prior to pulse-reverse electrodeposition, the constant potential deposition with various cathodic potentials was performed to determine the cathodic potentials of pulse-reverse electrodeposition based on the surface coverage of SPS, and the current profiles are exhibited in Fig. 5.3. As the overpotential was increased, the increasing rate of current at the initial stage and the saturation current were ascended. The increment of current was originated from the displacement of preadsorbed PEG-Cl⁻ by SPS, as mentioned

1 1 8

above. The initial displacement rates according to the overpotential are represented in

Fig. 5.4(a) indicating the acceleration of the displacement with higher overpotential.

On the contrary, the saturation time was not linearly dependent on the inverse of

displacement rate as displayed in Fig. 5.4(b). This was originated from the changes in

the saturation current, corresponding to the saturation coverage of SPS. The saturation

current and surface coverage of SPS are shown in Figs. 5.5(a) and (b). Although the

displacement rate was monotonically increased with higher overpotential, the surface

coverage of SPS at the saturation was also increased, lengthening the saturation time.

In Fig. 5.5(b), it was observed that the surface coverage of SPS was increased with

more negative potential. This was ascribed to the reduction of stability of PEG-Cl$^-$.

When more negative potential was applied, the electrode surface and Cl$^-$ were repelled

each other because of the electrostatic repulsion force. Since Cl$^-$ acts as the adsorption

site of PEG, the adsorption strength of PEG-Cl$^-$ was decreased. Based on the changes

of surface coverage of SPS at the saturation, the cathodic potentials of -100, -150, and -

200 mV (vs. OCP) were determined the conditions for pulse-reverse electrodeposition

because the saturation surface coverages 0.28, 0.43, and 0.62 representing lower,

intermediate, and higher surface coverage of SPS. In the case of the potential over -200

mV, the impact of mass transport of Cu ions dominated the electrodeposition system,

therefore, the experimental potentials were determined below -200 mV. Contrary to the

saturation coverage, the surface coverage of SPS at the initial stage was almost

identical in the range between 0.04 and 0.11 regardless of deposition conditions. Since

the concentration of PEG (i.e. surfactant) at the interface between the electrolyte and

the atmosphere was much higher than the inside of electrolyte, the relatively large

amount of PEG-Cl⁻ layer initially adsorbed on the Cu surface when Cu RDE passed

through the interface. This did not certainly depend on the conditions of constant

potential or pulse-reverse electrodeposition because applying the potentials was

enacted after dipping of Cu RDE.

The cathodic current profiles of pulse-reverse electrodeposition according to the

anodic potentials and reverse times were represented in Fig. 5.6. Overall, the initial

displacement rates (i.e. initial slope of current increment) of SPS were increased with

more positive anodic potential and longer reverse time regardless of the cathodic

potential. On the contrary, the saturation current was differently affected by the

cathodic potential, anodic potential, and reverse time. Particularly, in the case of more

positive anodic potential (i.e. 100 mV), the saturation current was relatively low even

the current was much more rapidly increased at the early stage. The saturation currents

from constant potential deposition with -200, -150, and -100 mV of cathodic potentials

were 15.51, 6.26, and 1.94 mA, respectively as shown in Fig. 5.3. Comparing these

values to the saturation currents of pulse-reverse electrodeposition, it can be found that

the changes in the values were depended on the cathodic potential, anodic potential,

and reverse time. Detail relationship between the saturation current and the conditions

of pulse-reverse electrodeposition will be discussed afterward.

 For more precise understanding of the relationship between anodic step and the

competitive adsorption of additives, the potential step chronoamperometry was

performed. In addition, since the cathodic current profiles were obtained by the

aforementioned simplification method, it could be verified by potential step

chronoamperometry whether the actual adsorption state of organic additives was

represented or not. Fig. 5.7(a) shows one of the results; the constant potential of -200

mV was interrupted by applying 100 mV of anodic potentials for 1 s at different

moments of 50, 100, 200, and 300 s from the beginning. Since the surface coverage of

SPS was continuously increased through the displacement, the potential step

chronoamperometry with varying the moments of applying the anodic step provides

the relationship between the anodic step and SPS coverage. It was clearly observed that

the currents after the anodic step were abruptly increased in the case of applying the

anodic step at 50 and 100 s. However, the currents after the anodic step were decreased

in the case of 200 and 300 s. The degree of current increment was much higher with lower surface coverage of SPS (earlier interruption at 50 s), and the current decrement was intensified with higher surface coverage (latest interruption at 300 s). Similar results at different anodic potential were presented in Fig. 5.7(b). The anodic potential was reduced to 25 mV, and the revere time was increased from 1 s to 7 s, which gives identical anodic charge to the case of 100 mV shown in Fig. 5.7(a). It is obvious that the increment in the current after the anodic step was reduced with lower anodic potential. On the basis of these results, it is needed to conclude that the competitive adsorption and displacement between the additives are obviously affected by the anodic potential. In addition, the simplified cathodic current profiles shown in Fig. 5.6 are figured out to be sufficient to describe the actual state of additive adsorption because the tendency of current change by pulse-reverse electrodeposition observed in Fig. 5.6 was identical to these potential step chronoamperometries.

Going back to Fig. 5.6, the initial displacement rates of SPS during pulse-reverse electrodeposition according to the cathodic/anodic potentials and reverse time were measured from the slope of current increments in Fig. 5.6. The behavior of initial displacement rates according to the reverse time, the cathodic and anodic potentials are exhibited in Fig. 5.8. Conclusively, the initial displacement rate was accelerated by the

anodic step, and it was intensified with more positive potential and longer reverse time. Comparing the results according to the cathodic potential, it was also observed that the initial displacement rate was in order of -200 mV > -150 mV > -100 mV, which is consistent with the results of constant potential deposition shown in Fig. 5.3. The saturation time was plotted according to the reverse time at different conditions, and the results are presented in Fig. 5.9. The figure indicates that the saturation times became short with higher initial displacement rate.

The enhanced initial displacement by the anodic step is due to several reasons. In order to investigate the effect during the cathodic step, pulse-reverse electrodeposition with varying the on-time were performed. The cathodic potential and on-time were changed from -100 mV to -200 mV and from 0.25 s to 1.5 s, respectively. The anodic potential and reverse time were fixed at 50 mV and 0.1 s. The simplified current profiles are exhibited in Fig. 5.10 indicating that pulse-reverse electrodeposition with longer on-time causes in the slowdown of the displacement. The exact values of displacement rate are shown in Fig. 5.11, measured from the initial slope of current increment in Fig. 5.10. Since the displacement rate of preadsorbed PEG-Cl⁻ layer by SPS was decreased as more on-time was applied, thus, the acceleration of displacement rate by pulse-reverse electrodeposition seemed to be the result of anodic step, not the

cathodic step. In the case of the anodic step, several reactions happen, such as dissolution of metallic Cu to hydrated Cu^+ and Cu^{2+} or Cu^+-SPS complex and 2MPS $\rightarrow$ SPS + $2e^-$, and the detachment of SPS or PEG-Cl^- through the lift-off.[12,74,96] As shown in Fig. 5.7, the increase in the current step lasted over several hundreds of second. This means that the instantaneous modification of surface state such as the formation of Cu^+-SPS or 2MPS $\rightarrow$ SPS + $2e^-$ or temporal increment of Cu ion concentration may have negligible effects. Therefore, the main reason for the enhanced displacement rate was related to the faster detachment of PEG-Cl^-. In previous researches, it was reported that the adsorbed PEG-Cl^- is much stable at more positive potential because of the electrostatic attraction between PEG-Cl^- and electrode. Therefore, it can be speculated that there are competing factors in determining the surface coverage of PEG-Cl^-; detachment by lift-off vs. stabilization by electrostatic attraction.

The changes in the surface coverage of additives during the anodic step were investigated with the chronoamperometry after the derivatization. The derivatization of PEG-Cl^- at various potentials for 10 s in the electrolyte containing 1.0 M H_2SO_4, 88 µM PEG, and 1 mM Cl^- was performed, followed by the chronoamperometry in the additive-free electrolyte consisted of 0.25 M $CuSO_4$ and 1.0 M H_2SO_4. As shown in

Fig.5.12, the slower current increment after the derivatization at more positive potential was observed, and it implies stronger adsorption of PEG-Cl⁻ in the range of potential examined. On the contrary, the lift-off of adsorbed PEG-Cl⁻ layer occurs as well, which was confirmed by LSV in the electrolyte containing 0.25 M CuSO$_4$, 1.0 M H$_2$SO$_4$, 88 μM PEG, and 1 mM Cl⁻ (Fig. 5.13). The starting potentials of LSV were intentionally varied for more precise understanding. The scan rate of LSV was 100 mV/s, which was considerably faster than ordinary LSV. The LSV results with 300 and 1000 rpm of RDE rotating speed are presented in Figs. 5.13(a) and (b) indicating that the current in the range between 50 and -300 mV was increased when LSV was started at more positive potential. Especially, the current increment was noticeable when the starting potential was over 100 mV. Since the identical results were observed regardless of rotating speed, this was not originated from the impact of Cu ion concentration. Therefore, it can be suggested that the detachment of PEG-Cl⁻ through lift-off certainly occurred during the anodic step. On the basis of two electrochemical analyses, it is natural to suggest that there were two competing effects of anodic step as has been previously mentioned; (i) the enhancement of adsorbed PEG-Cl⁻ and (ii) the detachment of PEG-Cl⁻ through lift-off. The former one dominated in the anodic potential range less than 100 mV, while the later happens at over 100 mV. However, the

results of pulse-reverse electrodeposition as previous introduced were from the anodic potential less than 100 mV, therefore, the influences of SPS should be additionally considered to explain the changes in the initial displacement.

The impact of SPS was investigated by using the potential step chronoamperometry after the derivatization of PEG-Cl$^-$. The derivatization was performed by dipping Cu RDE into the electrolyte containing 1.0 M H_2SO_4, 88 μM PEG, and 1 mM Cl$^-$ for 30 s. After the derivatization, the chronoamperometry was carried out in the electrolyte composed of 0.25 M $CuSO_4$, 1.0 M H_2SO_4, 1 mM Cl$^-$ without and with 50 μM SPS. As revealed in Fig. 5.14(a) in the absence of SPS, the current after the anodic step was rather decreased. This was identical to previous result observed in Fig. 5.12. On the contrary, when SPS is added into the electrolyte (Fig. 5.12(b)), the current was remarkably increased after the anodic step. The degree of current increment was enhanced with more positive potential. Since the current increment after the anodic step was only observed with SPS addition, the main reason for the promotion of displacement could be originated from the additional SPS adsorption on Cu surface where PEG-Cl$^-$ was detached.

The changes of saturation current measured from Figs. 5.6 and 5.10 are displayed in Figs. 5.15 and 5.16, and the tendency of saturation current was summarized in Table.

5.1. from the figures and table, it was found that the saturation current was increased with lower anodic potential and shorter reverse time, while it was reduced with higher anodic potential and longer reverse time as compared to constant potential deposition. Considering the lower surface coverage of SPS at more positive cathodic potential, it can be concluded that the surface coverage of SPS at its saturated state tends to be reduced when the anodic step is applied. The degree of decrease in the saturation current was intensified by higher cathodic potential, higher anodic potential, and longer reverse time. Dissimilar to the initial displacement rate, the electrode surface was covered by considerably large amount of SPS. Therefore, the reactions accompanied with both the electrons and SPS should be considered to explain this behavior. During the anodic step, both the change such as $2MPS \rightarrow SPS + 2e^-$ and the detachment of MPS, SPS, or Cu^+-SPS complex possibly took place. However, it was hard to separate each contribution on the behavior of surface coverage using the electrochemical analyses. The supplemental experiments are needed to exactly figure out this phenomenon.

In summary, the influence of pulse-reverse electrodeposition on the competitive adsorption between PEG-Cl$^-$ and SPS was investigated in detail. In order to easily compare the current profiles with various pulse-reverse electrodepositions, the

simplification method was introduced, and its validity was confirmed by potential step chronoamperometries. From the simplified current profiles, it was observed that the application of anodic step accelerated the displacement of preadsorbed PEG-Cl$^-$ layer by SPS, and the extent of displacement was increased as the anodic potential became more positive or the reverse time lengthened. It was speculated that this enhancement of displacement was due to the detachment of PEG-Cl$^-$ layer through lift-off, followed by additional SPS adsorption. On the contrary, the saturation current showed the different tendency to the initial displacement rate. The application of more positive potential and longer reverse time reduced the saturation current. Unfortunately, the main cause of this behavior remained to be investigated. In the next section, the superfilling performance of pulse-reverse electrodeposition was investigated, and it was attempted to explain the performance change based on these electrochemical analyses.

Table 5.1. The Behaviors of Saturation Current According to the Cathodic Potential,

Anodic Potential, and Reverse Time

E_{anodic} / $E_{cathodic}$	25 mV	50 mV	100 mV
-200 mV	↑	↓	↓
-150 mV	↑	↑ (0.1 s)* → ↓	↑ (0.05 s)* → ↓
-100 mV	↑	↑	↑ (0.1 s)* → ↓

*The reverse time where the tendency of the saturation current was changed.
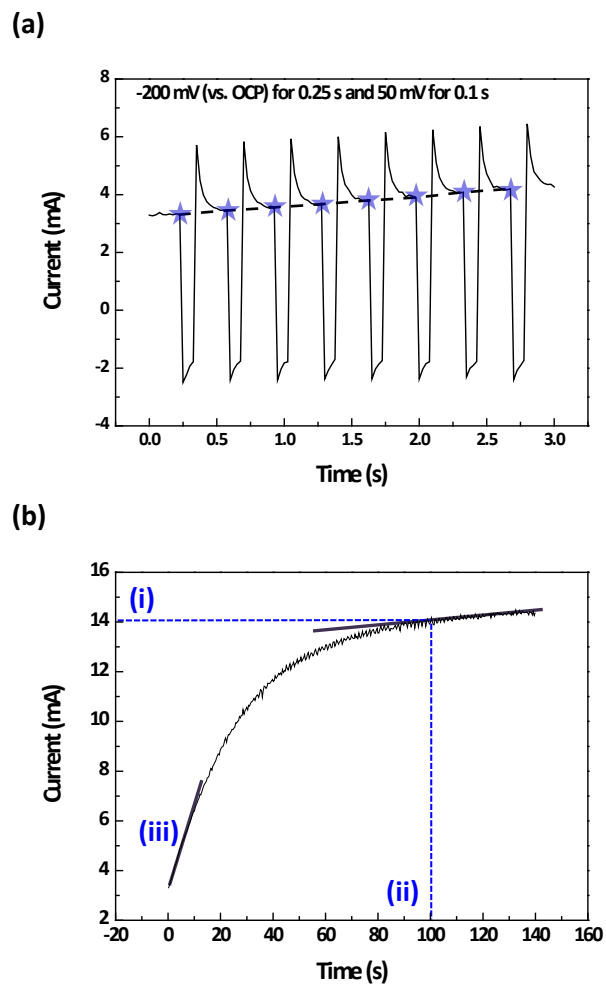
Fig. 5.1. (a) The representative current profile of pulse-reverse electrodeposition (black line) and the simplified current profile (straight line) by collecting the final values in the on-time (stars) for 3 s and (b) for 140 s with the definitions of (i) saturation current, (ii) saturation time, and (iii) initial displacement rate of SPS.

(a)

(b)
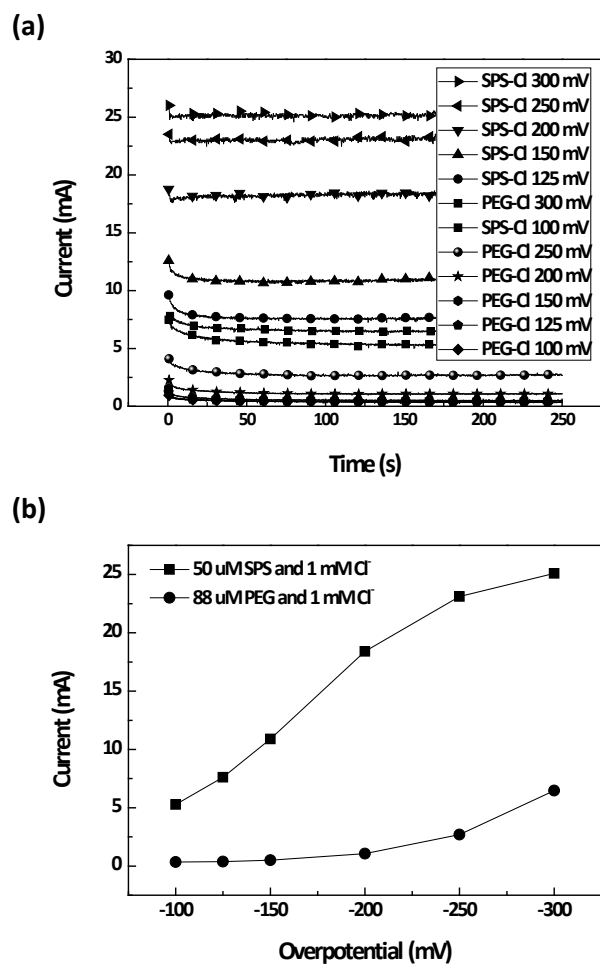
Fig. 5.2. (a) Chronoamperometries in the electrolyte containing PEG-Cl⁻ or SPS-Cl⁻ with changing the overpotential, and (b) the average current with overpotential dependence.
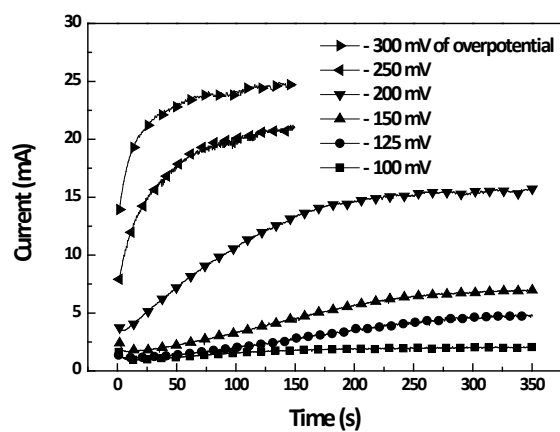
Fig. 5.3. The current profiles of constant potential deposition as the function of overpotential; the electrolyte contained PEG-Cl⁻-SPS.
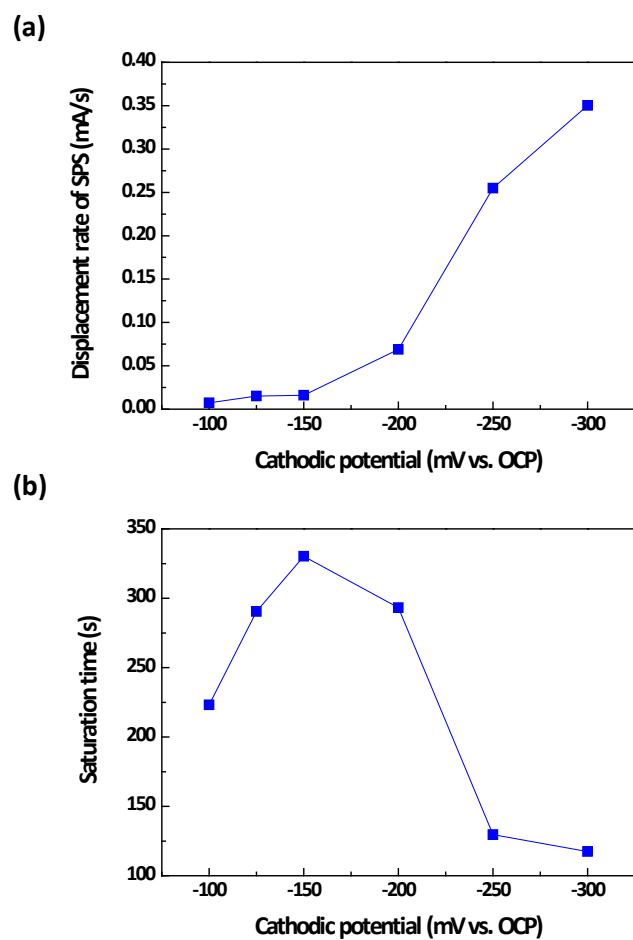
Fig. 5.4. (a) Initial displacement rate of SPS and (b) saturation time measured from Fig.

5.3.

(a)

(b)
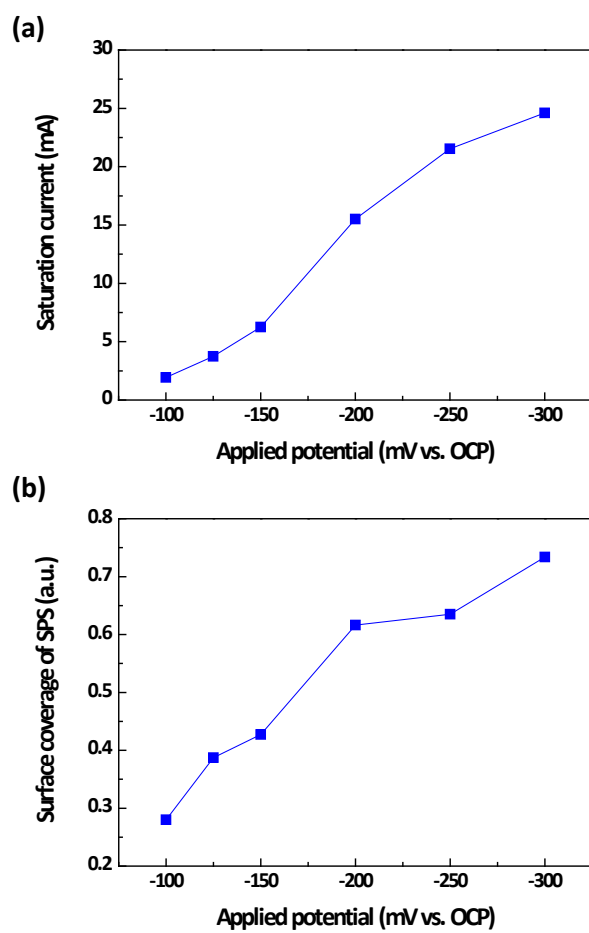
Fig. 5.5. (a) Saturation current measured from Fig. 5.3, and (b) the surface coverage of

SPS calculated from the saturation current represented in (a).
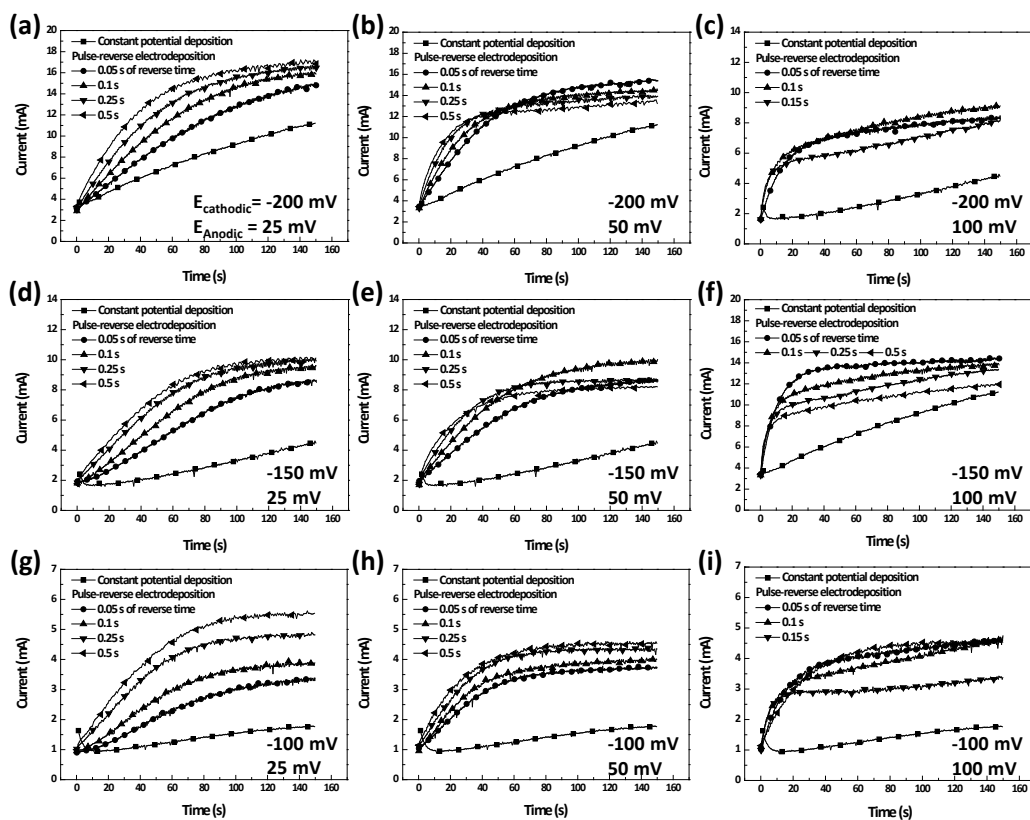
Fig. 5.6. The simplified current profiles of pulse-reverse electrodeposition with -200 mV of cathodic potential and (a) 25 mV, (b) 50 mV, and (c) 100 mV of anodic potential, -150 mV of cathodic potential and (d) 25 mV, (e) 50 mV, and (f) 100 mV of anodic potential, and -100 mV of cathodic potential and (g) 25 mV, (h) 50 mV, and (i) 100 mV of anodic potential.

(a)

(b)
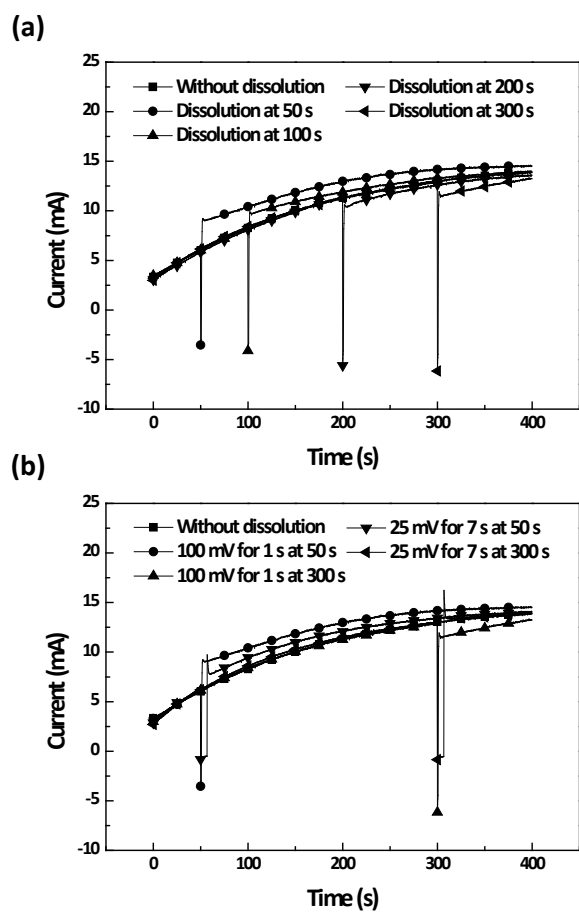
Fig. 5.7. Potential step chronoamperometries with applying (a) 100 mV of anodic potential for 1 s at 50 s, 100 s, 200 s, and 300 s, and (b) 25 mV of anodic potential at 50 s and 300 s for 7 s; the cathodic potential was fixed at -200 mV (vs. OCP).
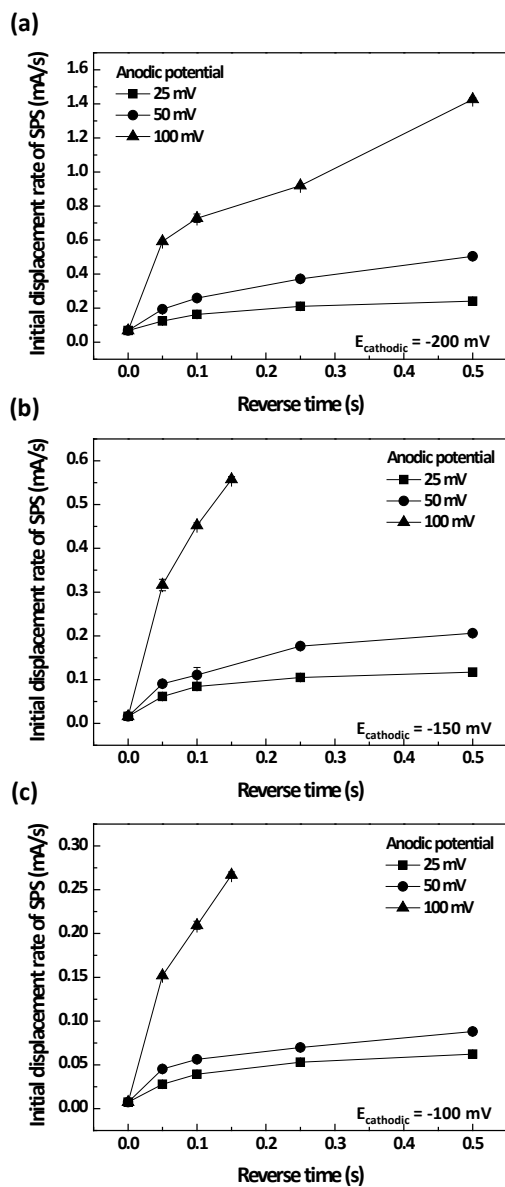
Fig. 5.8. Initial displacement rates of SPS as the function of the anodic potential and reverse time with (a) -200 mV, (b) -150 mV, and (c) -100 mV of cathodic potential; all of values were measured from Fig. 5.6.
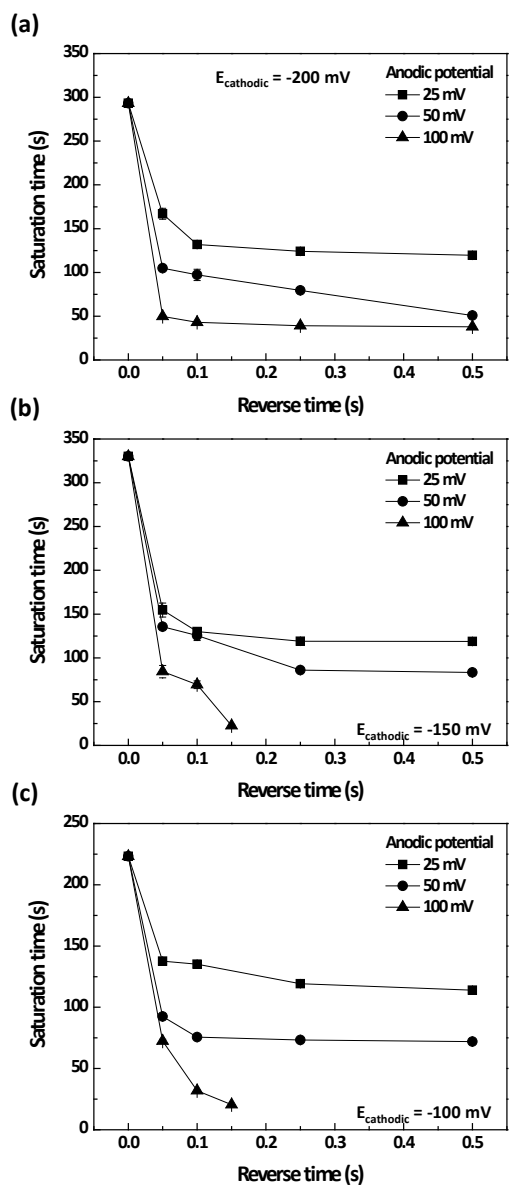
Fig. 5.9. The changes in the saturation times according to the anodic potential and reverse time with (a) -200 mV, (b) -150 mV, and (c) -100 mV of cathodic potential; all of values were measured from Fig. 5.6.

(a)

(b)

(c)
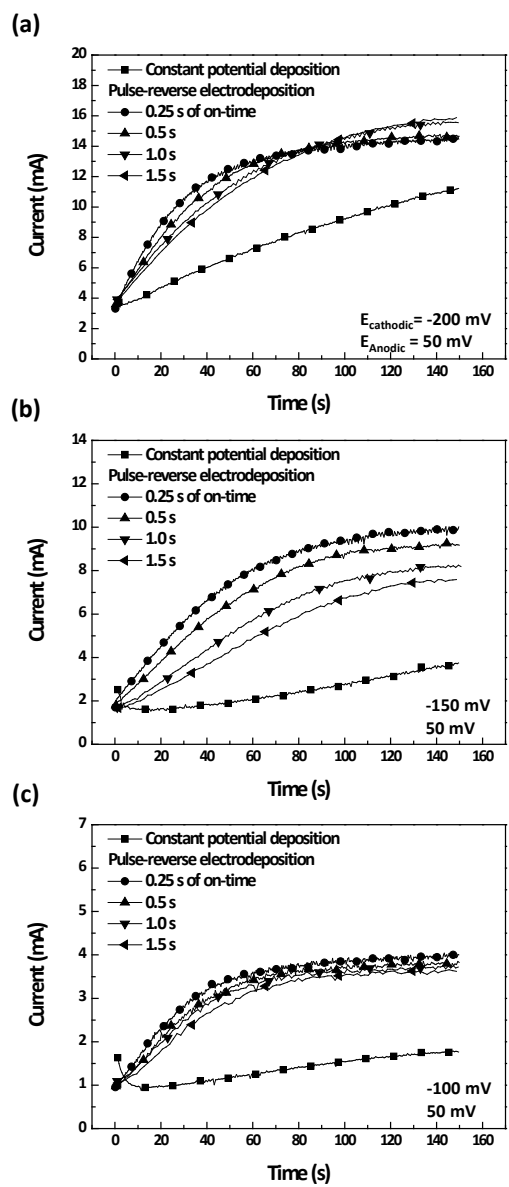
Fig. 5.10. The current profiles of pulse-reverse electrodeposition with (a) -200 mV, (b) -150 mV, and (c) -100 mV of cathodic potential; the anodic potential and reverse time were fixed at 50 mV and 0.1 s, and the on-time was varied from 0.25 s to 1.5 s.
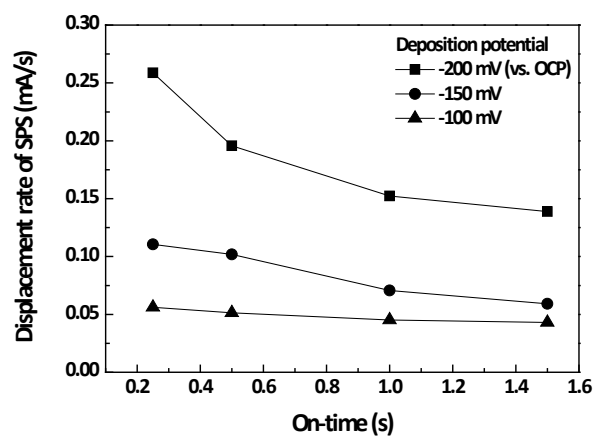
Fig. 5.11. Initial displacement rates of SPS according to the cathodic potential and on-time; all of the values were measured from Fig. 5.10.
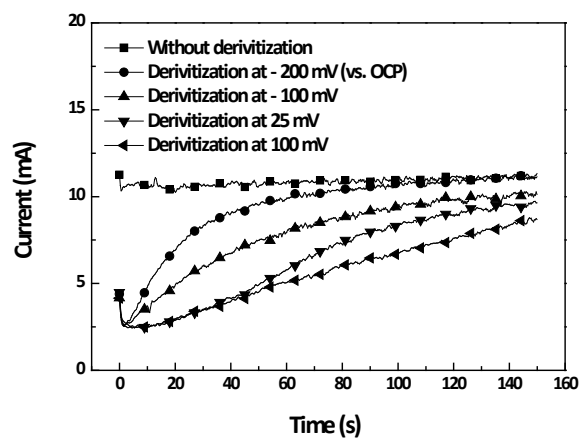
Fig. 5.12. Chronoamperometries with -200 mV (vs. OCP) of cathodic potential after the derivatization of PEG-Cl⁻ at various potentials.

(a)

(b)
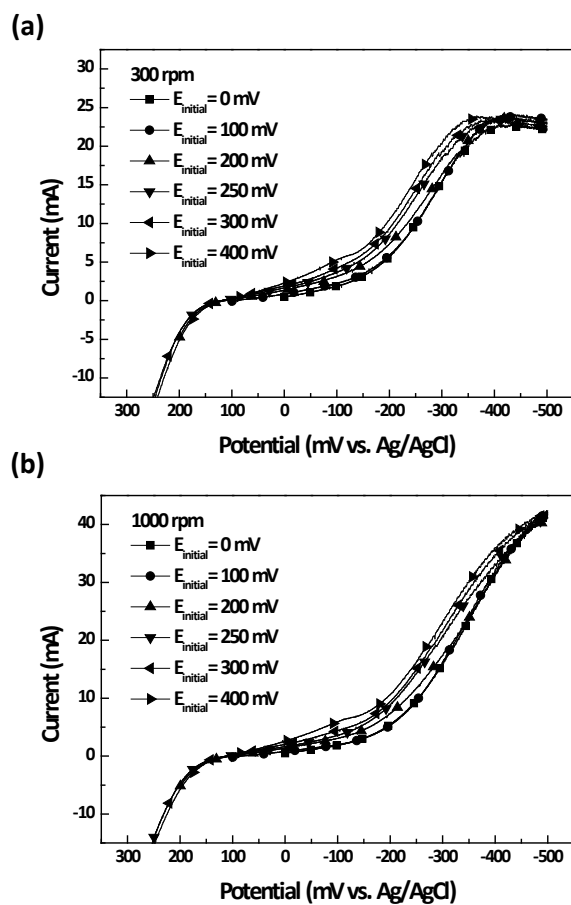
Fig. 5.13. LSV in the electrolyte only containing PEG-Cl⁻ with various initial potential; the rotating speeds of Cu RDE were (a) 300 rpm and (b) 1000 rpm, and the scan rate was fixed to 100 mV/s.

(a)

(b)
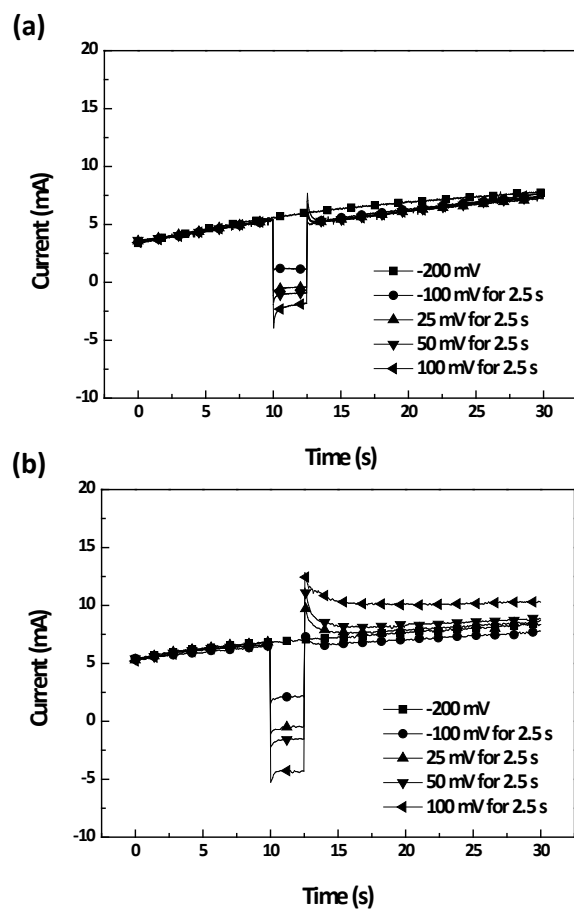
Fig. 5.14. Potential step chronoamperometries (a) in the absence of additives, and (b) in the presence of SPS-Cl⁻ after the derivatization of PEG-Cl⁻.

(a)

(b)

(c)
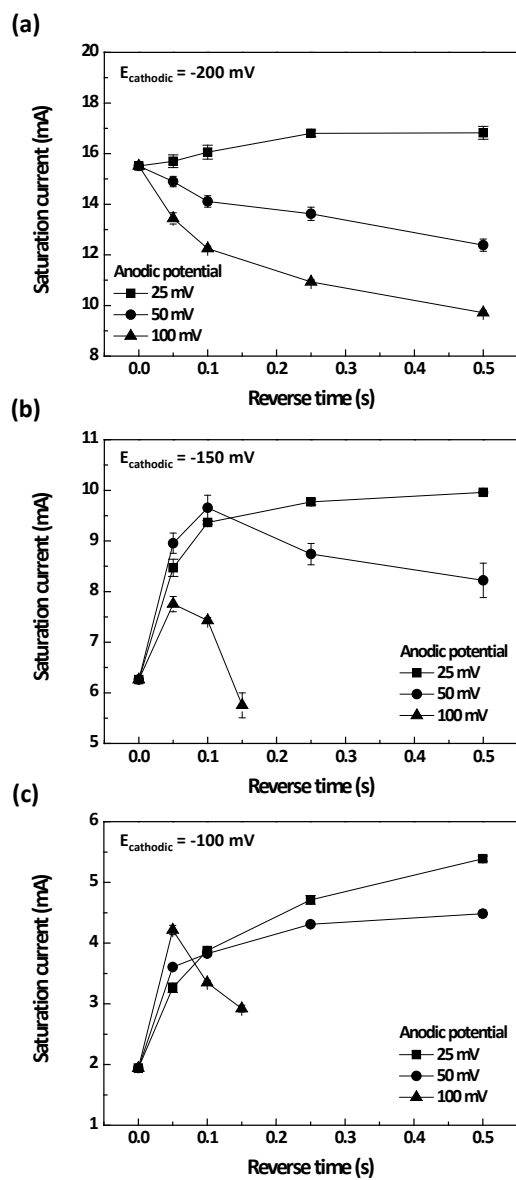
Fig. 5.15. The changes in the saturation current as the function of anodic potential and reverse time with (a) -200 mV, (b) -150 mV, and (c) -100 mV of cathodic potential; all of the values were measured from Fig. 5.6.
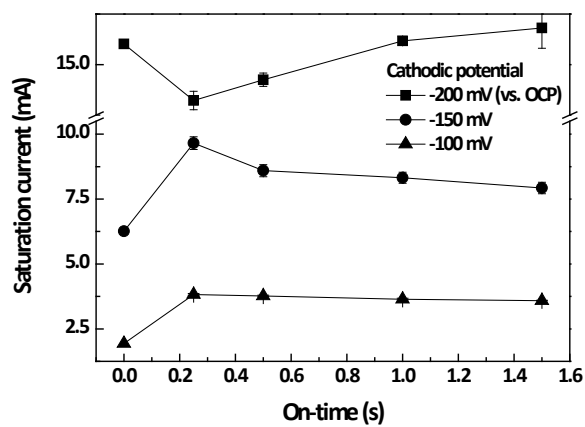
Fig. 5.16. The saturation current with various cathodic potential and on-time; all of the values were measured from Fig. 5.10.

5-2. The effects of anodic step on the superfilling performance

In order to clarify the impacts of the anodic step on the superfilling performance, pulse-reverse electrodeposition was performed with various anodic potentials and reverse times. In previous section, it was confirmed that the anodic step accelerated the displacement of preadsorbed PEG-Cl⁻ by SPS. Since the superfilling of Cu is the results from the adsorption and accumulation of SPS at the bottom of trench by the area reduction, the changes in the surface coverage of SPS at the initial stage of electrodeposition can modify the superfilling performance.

The representative deposition profiles with various anodic conditions are shown in Fig. 5.17. The deposition amount was fixed at 250 mC/cm^2, therefore, the height of Cu from the bottom could represent the superfilling performance. As observed in the figure, the height from the anodic step with relatively short reverse time was higher compared to the case of constant potential deposition. The average heights according to the anodic potential and reverse time are shown in Fig. 5.18(a), which which were measured at over 20 trenches. The optimum reverse times showing the relatively high thickness were observed, and these values were in the range between 0.025 s and 0.1 s. When the dissolution ratio is employed as the x-axis instead of reverse time, the

optimum dissolution ratios were also highlighted as displayed in Fig. 5.18(b). It was also revealed that the optimum dissolution ratio was slightly shifted to relatively large values with more positive anodic potential.

The reasons for the revelation of optimums and its shift according to the anodic potential can be found from the surface roughness. To achieve the superfilling without any void formation, the bottom-up (i.e. the deposition rate with the normal direction to the bottom surface) should overcome the closure of trench top by the surface roughness. That is, the impacts of organic additives competed with the surface roughness for obtaining successful superfilling. Therefore, it can be naturally surmised that the formation of rough surface is not suitable for the superfilling, and the optimum reverse time can be originated from the competition between the effects of additives and surface roughness.

In Chapter IV, it was confirmed that the surface roughness was significantly increased with relatively high dissolution ratio, and the increasing rate of surface roughness depended on the anodic potential. The application of more positive anodic potential exhibited relatively slow increase in the surface roughness. To confirm the effect of the surface roughness, the dissolution ratios were compared when the bottom thickness (Fig. 5.18(b)) and the surface roughness (Fig. 4.20(b)) of pulse-reverse

electrodeposition are identical to the results of constant potential deposition after the optimum dissolution ratio. The comparison results are displayed in Fig. 5.19, revealing the similar trend between surface roughness and the thickness at the bottom. Therefore, it can be concluded that the reduction of superfilling performance above the optimum dissolution ratio is originated from the surface roughness.

More information on the superfilling characteristics was obtained from the evolution of deposit profiles according to the deposition amount. Among various conditions of pulse-reverse electrodeposition, 25 mV of anodic potential and 0.05 s of reverse time were adopted, which exhibited the most superior bottom-up performance. The changes in the deposition profiles from constant potential deposition and the representative pulse-reverse electrodeposition according to the deposition amount are depicted in Figs. 5.20(a) to (h), and the average thicknesses at the center of trenches are summarized in Fig. 5.20(i). It was observed that the thicknesses were almost similar and the conformal deposition was progressed with the deposition amount below 150 mC/cm^2. This implies that the accumulation of SPS was not remarkably produced in this region. On the other hand, the bottom-up filling was observed over 200 mC/cm^2 of deposition amount, and the pulse-reverse electrodeposition exhibited faster bottom-up compared to constant potential deposition. The local acceleration of Cu deposition at the bottom

corresponded to the accumulation degree of SPS, therefore, it can be concluded that pulse-reverse electrodeposition exerted quick accumulation of SPS compared to constant potential deposition.

This phenomenon was also observed from the deposition profile at the corner of low-aspect-ratio trenches. Similar to the thickness from the bottom of high-aspect-ratio trenches, the corner of wide trench could be used for the investigation on the accumulation of SPS. The deposit profiles from constant potential and pulse-reverse electrodeposition are shown in Fig. 5.21. It can be found that the constant potential deposition exhibited only round profiles at the corners, however, the pulse-reverse electrodeposition formed the sharp diagonal profiles meaning more concentration of Cu deposition at the corner. The lengths of diagonal arrows marked in Figs. 5.21(c) to (f) are 90, 96, 125, and 119 nm, respectively, even though the thicknesses at the top of trenches were 102 nm for (c) and (d) (i.e. constant potential deposition), 89 nm for (e) and (f) (i.e. pulse-reverse electrodeposition). The point that the pulse-reverse electrodeposition resulted in more deposition at the corner of trench with relatively low thickness of Cu at the top naturally suggested that pulse-reverse electrodeposition produced high accumulation of SPS more quickly compared to constant potential deposition as analogous to Fig. 5.20.

From now on, the reason why the pulse-reverse electrodeposition can improve the superfilling performance is discussed. There are the factors from pulse-reverse electrodeposition to influence on the superfilling characteristics such as the promotion of displacement between preadsorbed PEG-Cl$^-$ and SPS, the replenishment of Cu ions inside the trench during the reverse time, and the selective dissolution of Cu at the side walls. The effect of changes in the Cu ion concentration can be excluded because the deposition potential was too low to develop the considerable concentration gradient within 40 s of deposition time. In addition, the selective dissolution at the side wall was also negligible because the similar thickness of Cu at the side wall was observed regardless of filling conditions. Therefore, it can be carefully speculated that the improvement of superfilling is related to the promotion of displacement between PEG-Cl$^-$ and SPS which was introduced in the previous section.

In previous CEAC prediction, it was reported that the superfilling could occur with the sufficient surface coverage of SPS and the incubation period showing conformal profile could be observed. The incubation of superfilling originating from insufficient coverage of SPS was clearly confirmed in Fig. 5.20 indicating the conformal profiles with the deposition amount less than 150 mC/cm^2. That is, the initial displacement of SPS is important to exert successful and rapid superfilling, and it became more

significant when the time for superfilling is reduced due to the small dimension of filling features. Therefore, it is naturally concluded that pulse-reverse electrodeposition reduced the incubation period through promoting the displacement, and it finally improves the superfilling performance. The more concentrated deposition at the corner of low-aspect-ratio with pulse-reverse electrodeposition was also understood by the shortening of incubation period.

On the basis of these results, it can be concluded that the acceleration of displacement between two organic additives with pulse-reverse electrodeposition has an advantage in the aspect that the superfilling phenomenon appeared at the initial stage of electrodeposition. It was originated from the rapid accumulation of large amount of SPS at the bottom of trench. As observed in Chapter IV, the resistivity with low dissolution ratio was lower than pulse electrodeposition with the optimum condition, therefore, the merit in the aspect of film property was also obtained by the pulse-reverse electrodeposition.
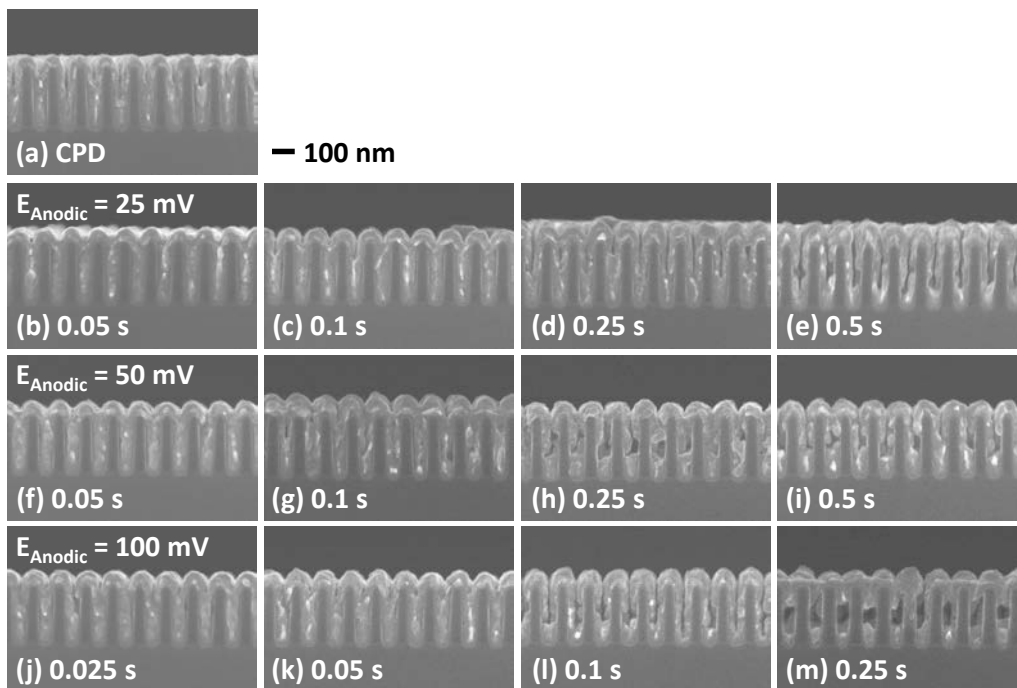
Fig. 5.17. The profiles of Cu deposited by (a) constant potential deposition, and pulse-reverse electrodeposition with 25 mV of anodic potential and (b) 0.05 s, (c) 0.1 s, (d) 0.25 s, (e) 0.5 s of reverse time, 50 mV of anodic potential and (f) 0.05 s, (g) 0.1 s, (h) 0.25 s, (i) 0.5 s of reverse time, and 100 mV of anodic potential and (j) 0.025 s, (k) 0.05 s, (l) 0.1 s, and 0.25 s of reverse time.

(a)

(b)
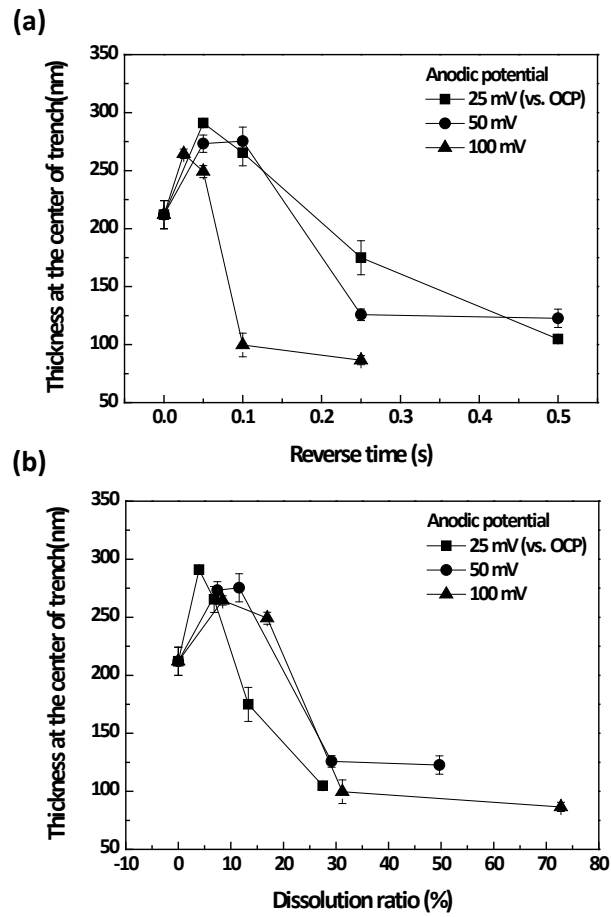
Fig. 5.18. (a) The changes in the thickness of Cu at the center of trench according to the reverse time, and (b) the re-plotted results with the dissolution ratio as the x-axis instead of reverse time.
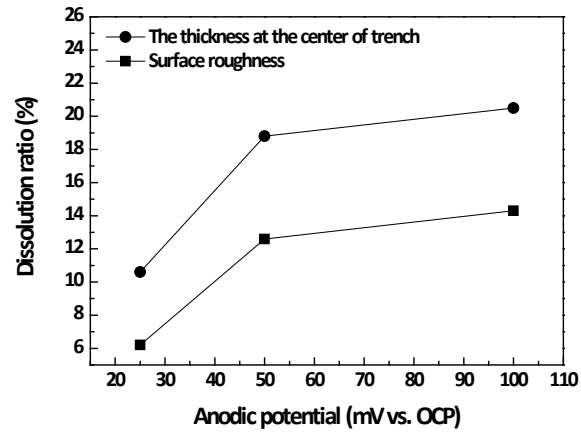
Fig. 5.19. The dissolution ratios when the surface roughness (Fig. 4.20(b)) and the thickness at the center of trench (Fig. 5.18(b)) with pulse-reverse electrodeposition are identical to the results of constant potential deposition.
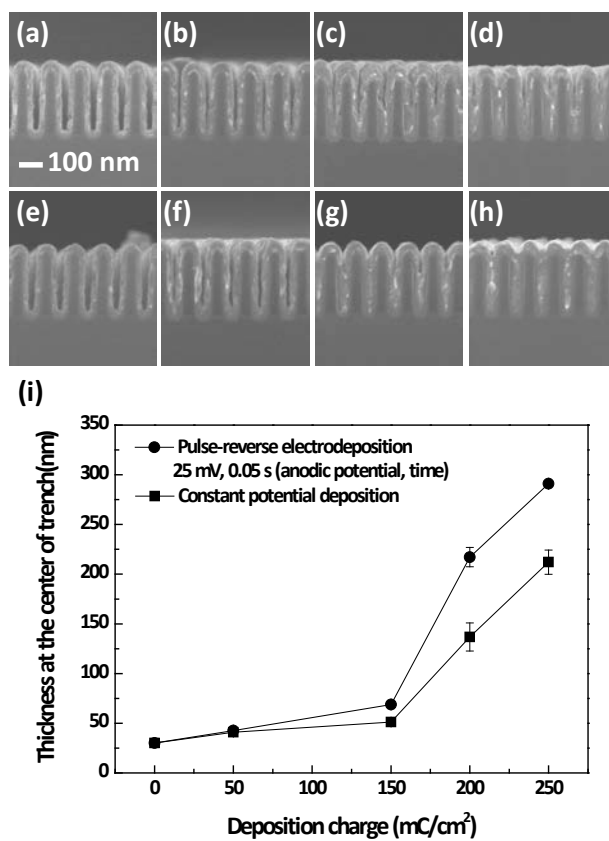
Fig. 5.20. The deposition profiles of Cu by means of constant potential deposition with

(a) 50 mC/cm^2, (b) 150 mC/cm^2, (c) 200 mC/cm^2 and (d) 250 mC/cm^2, and pulse-

reverse electrodeposition with (e) 50 mC/cm^2, (f) 150 mC/cm^2, (g) 200 mC/cm^2, and (h)

250 mC/cm^2, and (i) the thickness of Cu at the center of trenches measured from the

images.
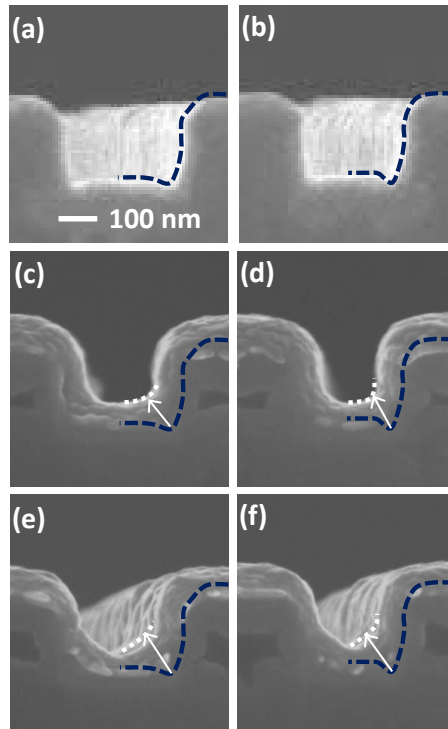
Fig. 5.21. The profiles of trenches with (a) 290 nm and (b) 260 nm of width, and the

deposition profile of Cu by constant potential deposition at the trenches with (c) 290

nm and (d) 260 nm of width, and by pulse-reverse electrodeposition at the trenches

with (e) 290 nm and (f) 260 nm of width. The depth of the trench was 240 nm, and the

deposition amount was fixed to 200 mC/cm^2.

CHAPTER VI

Conclusions

The continuous reduction of Cu interconnection dimensions raises the problems related to the interconnection properties and the difficulty in the superfilling. The modification of organic additives, the application of new material, and the changes in the waveform of current or potential can be the candidates to resolve these issues. Among various candidates, the modification of potential or current waveform was investigated in this study with the aspect of Cu property and superfilling performance.

Pulse electrodeposition was found to reduce the electrical resistivity and more develop (111) crystal orientation compared to constant potential deposition. This was originated from the grain growth during the off-time, which was totally different to self-annealing. However, the grain growth was retarded with the organic additives which strongly adsorbed on Cu surface reducing the energy differences.

The anodic step in the pulse-reverse electrodeposition considerably affected the film properties such as the grain size, crystallinity, and surface roughness. The dissolution during the anodic step also reflected the energy differences, and the anodic potential determined the degree of reflection. The competition of surface roughness and grain

size caused the optimum anodic charge showing the lowest resistivity, which was also lower than the optimum of pulse electrodeposition. On the contrary, when the organic additives are introduced, the selective dissolution was determined by the kinds of adsorbates. That is, Cu covered by SPS-Cl⁻ was much easily dissolved compared to Cu covered by PEG-Cl⁻. Dissimilar to the results without additives, the electrical resistivity of Cu film was determined by the surface roughness. At the optimum dissolution ratio, the electrical resistivity of Cu film deposited by pulse-reverse electrodeposition was considerably lower compared to pulse electrodeposition. On the basis of the results, it was obviously confirmed that pulse-reverse electrodeposition exhibited the significant advantage in the aspect of film properties, therefore, the superfilling performance of pulse-reverse electrodeposition was also investigated.

Superfilling of Cu was strongly related to the adsorption of organic additives and their accumulation according to the area reduction. Prior to gap-filling, the impacts anodic step on the competitive adsorption was investigated, and it was observed that the anodic step accelerated the displacement of preadsorbed PEG-Cl⁻ layer by SPS and its degree was increased with more positive anodic potential and longer reverse time. Based on this, pulse-reverse electrodeposition was applied to Cu superfilling, and it was confirmed that pulse-reverse electrodeposition exhibited superior superfilling

performance compared to constant potential deposition at the trench with 55 nm of width.

  In conclusion, pulse and pulse-reverse electrodeposition has various merits compared to constant potential deposition. Especially, pulse-reverse electrodeposition showed the improvement of Cu properties as well as excellent superfilling performance. Therefore, it can be concluded that pulse and pulse-reverse electrodeposition enables us to achieve Cu interconnection with high speed, high integrity and superior reliability.

References

1. P. C. Andricacos, C. Uzoh, J. O. Dukovic, J. Horkans, H. Delihianni, *IBM J. Res. Dev.*, **42**, 567 (1998).

2. ITRS, *International Technology Roadmap for Semiconductors*, **2007**, Interconnect.

3. ITRS, *International Technology Roadmap for Semiconductors*, **2009**, Interconnect.

4. ITRS, *International Technology Roadmap for Semiconductors*, **2011**, Interconnect.

5. M. T. Bohr, Proc. *IEEE IEDM Tech. Dig.*, 241 (1995).

6. S. P. Muraka, *Microelectron. Eng.*, **29**, 37 (1997).

7. G. Schneider, D. Hamback, B. Niemann, B. Kaulich, J. Susini, N. Hoffmann, and W. Hasse, *Appl. Phys. Lett.*, **78**, 1936 (2001).

8. B. Zhao, H. Kim, and Y. Shimogaki, *Jpn. J. Appl. Phys.*, **44**, L1278 (2005).

9. P. M. Vereecken, R. A. Binstead, H. Deligianni, P. C. Andricacos, *IBM J. Res. Dev.*, **49**, 3 (2005).

10. T. P. Moffat, J. E. Bonevich, W. H. Huber, A. Stanishevsky, D. R. Kelly, G. R. Stafford, and D. Josell, *J. Electrochem. Soc.*, **147**, 4524 (2000).

11. A. C. West, S. Mayer, and J. Reid, *Electrochem. Solid-State Lett.*, **4**, C50 (2001).

12. S. -K. Kim and J. J. Kim, *Electrochem. Solid-State Lett.*, **7**, C98 (2004).

13. T. P. Moffat, D. Wheeler, M. D. Edelstein, and D. Josell, *IBM J. Res. Dev.*, **49**, 19 (2005).

14. S. -K. Kim, D. Josell, and T. P. Moffat, *J. Electrochem. Soc.*, **153**, C826 (2006).

15. J. W. Gallaway, M. J. Willey, and A. C. West, *J. Electrochem. Soc.*, **156**, D287 (2009).

16. J. P. Healy, D. Pletcher, and M. Goodenough, *J. Electronal. Chem.*, **338**, 167 (1992).

17. A. C. West, S. Mayer, and J. Reid, *Electrochem. Solid-State Lett.*, **4**, C50 (2001).

18. A. Frank and A. J. Bard, *J. Electrochem. Soc.*, **150**, C244 (2003).

19. M. Kang and A. A. Gewirth, *J. Electrochem. Soc.*, **150**, C426 (2003).

20. S. K. Cho, S. -K. Kim, and J. J. Kim, *J. Electrochem. Soc.*, **152**, C330 (2005).

21. B. Bozzini, L. D'Urzo, V. Romanello, and C. Mele, *J. Electrochem. Soc.*, **153**, C254 (2006).

22. M. Tan, C. Guymon, D. R. Wheeler, and J. N. Harb, *J. Electrochem. Soc.*, **154**, D78 (2007).

23. C. E. Taubert, D. M. Kolb, U. Memmert, and H. Meyer, *J. Electrochem. Soc.*, **154**, D293 (2007).

24. S. K. Cho, M. J. Kim, H. -C. Koo, O. J. Kwon, and J. J. Kim, *Thin Solid Films*, **520**, 2136 (2012).

25. J. P. Healy, D. Pletcher, and M. Goodenough, *J. Electronal. Chem.*, **338**, 155 (1992).

26. Z. V. Feng, X. Li, and A. A. Gewirth, *J. Phys. Chem. B*, **107**, 9415 (2003).

27. W. -P. Dow, M. -Y. Yen, W. -B. Lin, and S. -W. Ho, *J. Electrochem. Soc.*, **152**, C769 (2005).

28. M. L. Walker, L. J. Richter, and T. P. Moffat, *J. Electrochem. Soc.*, **154**, D277 (2007).

29. W. Wang and Y. -B. Li, *J. Electrochem. Soc.*, **155**, D263, (2008).

30. M. E. H. Garrido and M. D. Pritzker, *J. Electrochem. Soc.*, **156**, D175 (2009).

31. D. Josell, D. Wheeler, W. H. Huber, J. E. Bonevich, and T. P. Moffat, *J. Electrochem. Soc.*, **148**, C767 (2001).

32. T. P. Moffat, D. Wheeler, S. -K. Kim, and D. Josell, *J. Electrochem. Soc.*, **153**, C127 (2006).

33. D. Josell, T. P. Moffat, and D. Wheeler, *J. Electrochem. Soc.*, **154**, D208 (2007).

34. T. P. Moffat, D. Wheeler, S. -K. Kim, and D. Josell, *J. Electrochem. Soc.*, **153**, C127 (2006).

35. T. P. Moffat, D. Wheeler, and D. Josell, *J. Electrochem. Soc.*, **151**, C262 (2004).

36. M. J. Willey and A. C. West, *J. Electrochem. Soc.*, **154**, D156 (2007).

37. A. F. Mayadas and M. Shatzkes, *Phys. Rev. B*, **1**, 1382 (1970).

38. R. Rosenberg, A. F. Mayadas, and D. Gupta, *Surf. Sci.*, **31**, 566 (1972).

39. S. M. Rossnagel and T. S. Kuan, *J. Vac. Sci. Technol. B*, **22**, 240 (2004).

40. R. C. Munoz, J. Mol. *Catal. A-Chem.*, **228**, 163 (2005).

41. J. J. Plombon, E. Andideh, V. M. Dubin, and J. Maiz, *Appl. Phys. Lett.*, **89**, 113124 (2006).

42. H. Marom, M. Ritterband, and M. Eizenberg, *Thin Solid Films*, **510**, 62 (2006).

43. J. M. Camacho and A. L. Oliva, *Thin Solid Films*, **515**, 1881 (2006).

44. J. -W. Lim and M. Isshiki, *J. Appl. Phys.*, **99**, 094909 (2006).

45. J. M. Purswani and D. Gall, *Thin Solid Films*, **516**, 465 (2007).

46. T. Sun, B. Yao, A. P. Warren, V. Kumar, S. Roberts, K. Barmak, and K. R. Coffey, *J. Vac. Sci. Technol. A*, **26**, 605 (2008).

47. T. Osaka, N. Yamachika, M. Yoshino, M. Hasegawa, Y. Negishi, and Y. Okinaka, *Electrochem. Solid-State Lett.*, **12**, D15 (2009).

48. Y. Ke, F. Zahid, V. Timoshevskii, K. Xia, D. Gall, and H. Guo, *Phys. Rev. B*, **79**, 144306 (2009).

49. T. Sun, B. Yao, A. P. Warren, K. Barmak, M. F. Toney, R. E. Peale, and K. R. Coffey, *Phys. Rev. B*, **81**, 155434 (2010).

50. R. Henriquez, S. Cancino, A. Espinosa, M. Flores, T. Hoffmann, G. Kremer, J. G.

Lisoni, L. Moraga, R. Morales, S. Oyarzun, M. A. Suarez, A. Zuniga, and R. C. Munoz, *Phys. Rev. B*, **82**, 113409 (2010).

51. C. -F. Chen and K. -C. Lin, *Jpn. J. Appl. Phys.*, **41**, 1981 (2002).

52. C. M. Tan and A. Roy, *Mater. Sci. Eng. R*, **58**, 1 (2007).

53. S. Vaidya and A. K. Shinha, *Thin Solid Films*, **75**, 253 (1981).

54. D. Kwon, H. Park, and C. Lee, *Thin Solid Films*, **475**, 58 (2005).

55. H. L. Cho and J. G. Lee, *Mat. Res. Soc. Symp. Proc.*, **564**, 353 (1999).

56. W. Lee, H. Cho, B. Cho, J. Kim, Y. -S. Kim, W. -G. Jung, H. Kwon, J. Lee, P. J. Reucroft, C. Lee, and J. Lee, *J. Electrochem. Soc.*, **147**, 3066 (2000).

57. S. Strehle, S. Menzel, A. Jahn, U. Merkel, J.W. Bartha, and K. Wetzig, *Microelectron. Eng.*, **86**, 2396 (2009).

58. S. C. Chang, J. M. Shieh, K. C. Lin, B. T. Dai, T. C. Wang, C. F. Chen, M. S. Feng, Y. H. Li, and C. P. Lu, *J. Vac. Sci. Technol. B*, **19**, 767 (2001).

59. B. K. Purushothaman, P. W. Morrison, Jr., and U. Landau, *J. Electrochem. Soc.*, **152**, J33 (2005).

60. J. -C. Puippe and F. Leaman, *Theory and Practice of Pulse Plating*, AESF (1986).

61. C. H. Seah, S. Mridha, and L. H. Chan, *J. Mater. Process. Technol.*, **114**, 233 (2001).

62. N. Tantavichet and M. D. Pritzker, *J. Electrochem. Soc.*, **149**, C289 (2002).

63. S. -C. Chang, J. -M. Shieh, B. -T. Dai, and M. -S. Feng, *J. Vac. Sci. Technol. B*, **20**, 2295 (2002).

64. M. S. Chandrasekar and M. Pushpavanam, *Electrochim. Acta*, **53**, 3313(2008).

65. U. Emekli and A. C. West, *Electrochim. Acta*, **54**, 1177 (2009).

66. L. Lu, Y. Shen, X. Chen, L. Qian, and K. Lu, *Science*, **304**, 422 (2004).

67. M. Dao, L. Lu, Y. F. Shen, and S. Suresh, *Acta Mater.*, **54**, 5421 (2006).

68. L. Lu, X. Chen, X. Huang, and K. Lu, *Science*, **323**, 607 (2009).

69. M. S. Chandrasekar and M. Pushpavanam, *Electrochim. Acta*, **53**, 3313 (2008).

70. A. C. West, C. -C. Cheng, and B. C. Baker, *J. Electrochem. Soc.*, **145**, 3070 (1998).

71. M. Georgiadou and D. Veyret, *J. Electrochem. Soc.*, **149**, C324 (2002).

72. J. -J. Sun, K. Kondo, T. Okamura, S. J. Oh, M. Tomisaka, H. Yonemura, M. Hoshino, and K. Takahashi, *J. Electrochem. Soc.*, **150**, G355 (2003).

73. K. Kondo, T. Yonezawa, D. Mikami, T. Okubo, Y. Taguchi, K. Takahashi, and D. P. Barkey, *J. Electrochem. Soc.*, **152**, H173 (2005).

74. M. Hayase and M. Nagao, *J. Electrochem. Soc.*, **156**, D198 (2009).

75. M. -Y. Cheng, K. -W. Chen, T. -F. Liu, Y. -L. Wang, and H. -P. Feng, *Thin Solid Films*, **518**, 7468 (2010).

76. B. V. Sarada, C. L. P. Pavithra, M. Ramakrishna, T. N. Rao, and G. Sundararajan, *Electrochem. Solid-State Lett.*, **13**, D40 (2010).

77. S. K. Cho, M. J. Kim, T. Lim, O. J. Kwon, and J. J. Kim, *J. Vac. Sci. Technol. B*, **29**, 011004 (2011).

78. L. Hufmann, R. Ecke, S. E. Schulz, and T. Gessner, *Microelectron. Eng.*, **88**, 705 (2011).

79. S. S. Kim, Mater thesis, Seoul National University (2007).

80. M. J. Kim, S. K. Cho, and J. J. Kim, *ECS Trans.*, **16**(22), 87 (2009).

81. S. Rashkov, D. S. Stoichev, and I. Tomov, *Electrochim. Acta*, **17**, 1955 (1972).

82. S. M. Rossnagel and T. S. Kuan, *J. Vac. Sci. Technol. A*, **20**, 1911 (2002).

83. T. Hara, H. Toida, and Y. Shimura, *Electrochem. Solid-State Lett.*, **6**, G98 (2003).

84. P. Sonnweber-Ribic, P. Gruber, G. Dehm, and E. Arzt, *Acta Mater.*, **54**, 3863 (2006).

85. M. Stangl, M. Liptak, A. Fletcher, J. Acker, J. Thomas, H. Wendrock, S. Oswald, and K. Wetzig, *Microelectron. Eng.*, **85**, 534 (2008).

86. S. Lagrange, S. H. Brongersma, M. Judelewicz, A. Saerens, I. Vervoort, E. Richard, R. Palmans, and K. Maex, *Microelectron. Eng.*, **50**, 449 (2000).

87. H. Lee, S. S. Wong, and S. D. Lopatin, *J. Appl. Phys.*, **93**, 3796 (2003).

88. M. Stangl and M. Militzer, *J. Appl. Phys.*, **103**, 113521 (2008).

89. T. Osaka, N. Yamachika, M. Yoshino, M. Hasegawa, Y. Negishi, and Y. Okinaka, *Electrochem. Solid-State Lett.*, **12**, D15 (2009).

90. B. E. Warren, *X-ray Diffraction*, Dover publications, New York (1990).

91. B. D. Cullity and S. R. Stock, *Elements of X-ray Diffraction*, Prentice Hall, New Jersey (2001).

92. Y. Ke, F. Zahid, V. Timoshevskii, K. Xia, D. Gall, and H. Guo, *Phys. Rev. B*, **79**, 144306 (2009).

93. H. P. Feng, M. Y. Cheng, Y. L. Wang, S. C. Chang, Y. Y. Wang, and C. C. Wan, *Thin Solid Films*, **498**, 56 (2006).

94. D. Josell, S. H. Brongersma, and Z. Tokei, *Annu. Rev. Mater. Res.*, **39**, 231 (2009).

95. A. J. Bard and L. R. Faulkner, *Electrochemical methods, Fundamentals and Application*, 2nd ed., John Wiley & Sons (2001).

96. M. Hayase and K. Otsubo, *J. Electrochem. Soc.*, **157**, D628 (2010).

국문 초록

구리 배선의 크기 감소는 배선의 특성 저하와 도금을 이용한 수퍼필링의 어려움과 같은 문제를 제기하였다. 특히 배선의 특성 관점에서 전기 저항 증가와 일렉트로마이그레이션에 따른 결함 발생이 가장 큰 이슈이다. 본 연구에서는, 펄스와 펄스-리벌스 전해 도금을 이용하여 구리 박막의 물성 및 수퍼필링 특성 향상을 시도하였다.

펄스 전해 도금은 구리 전착이 진행되는 온타임과 개방 회로 전압를 인가하는 오프타임으로 구성되며, 피크 전압, 온타임과 오프타임의 길이가 중요한 변수이다. 오프 타임을 변화시켜가면서 구리 박막을 전착한 결과를 바탕으로 오프 타임 동안 그레인의 성장이 일어나는 것을 밝혔으며, 이는 결정성의 향상과 전기적 저항의 감소를 가져왔다. 오프 타임 동안의 그레인 성장은 결정면의 종류와 그레인의 크기에 따라 결정되는 표면 에너지와 그레인 경계 에너지의 차이에 의한 결과로 생각된다. 충분한 오프 타임을 인가하여 구리 박막을 전착한 경우, 정전압 도금에 비해 68% 높은 (111) 결정성과 22% 낮은 저항을 얻을 수 있었다. 하지만, 구리 수퍼필링에 사용되는 유기 첨가제를 전해질에 첨가한 경우, 오프타임 동안의 그레인 성장이 급격히 줄어드는 것을 알 수 있었으며, 이는 유기 첨가제가 구리

표면에 강하게 흡착하여 그레인의 에너지를 변화 시키기 때문이다. 따라서 구리 박막의 특성을 좀더 향상시키기 위해 앞서 연구된 펄스 전해 도금에 구리 용해가 일어나는 양극 과정을 추가한 펄스-리벌스 전해 도금을 도입하였다.

 펄스-리벌스 전해 도금의 양극 과정과 유기 첨가제 각각의 영향을 알아보기 위해 첨가제의 유무와 용해 과정의 양극 전압, 리벌스 타임의 길이에 따른 박막 특성 변화를 확인하였다. 첨가제가 없는 경우의 박막 특성 변화에서 펄스 전해 도금과 마찬가지로 열역학적 에너지 차이에 따른 선택적인 용해가 일어남을 알 수 있었다. 선택적 용해는 양극반응의 전압에 따라 변화하였으며, 이는 다양한 박막 특성의 변화 속도를 결정하였다. 즉, 상대적으로 높은 양극 전압의 인가는 구리 용해의 선택성을 저해하였으며, 이는 양극 반응의 증가에 따라 그레인의 크기 및 표면 거칠기가 천천히 변화하는 결과를 가져왔다. 펄스-리벌스 전해 도금의 경우, 펄스 도금과 달리 구리 박막의 전기적 저항은 표면 거칠기와 그레인의 크기의 경쟁에 따라 결정되었으며, 이 결과, 가장 낮은 저항을 나타내는 최적 조건이 존재하였다. 첨가제가 없는 경우, 최적 조건에서 펄스 전해도금 대비 9% 낮은 저항을 나타내었다. 하지만 구리 수퍼필링을 위한 첨가제가 전해질에 공급된 경우, 용해의 선택성은 표면 그리고 그레인 경계 에너지가 아닌

흡착질에 의해 결정되었다. SPS로 덮힌 구리가 PEG-Cl⁻이 흡착한 구리에 비해 훨씬 쉽게 용해되는 것을 확인하였다. 또한, 첨가제가 있는 경우, 박막의 저항은 표면 거칠기에 크게 관계함을 알 수 있었으며, 최적 조건 역시 표면 거칠기에 의해 결정되었다. 펄스 전해 도금 대비, 첨가제가 있는 경우의 펄스-리벌스 전해 도금 역시 구리 박막의 저항을 14% 감소시켰다. 위의 결과는 펄스-리벌스 전해 도금을 이용하여 전착된 구리가 전기 전도성 측면에서 큰 장점이 있는 것을 의미하기 때문에, 펄스-리벌스 전해 도금을 구리 수퍼필링에 적용해 보았다.

 수퍼필링의 특성은 유기 첨가제의 흡착과 트렌치 바닥에서 면적 감소에 따른 첨가제의 축적에 의해 결정된다. 따라서 펄스-리벌스 전해 도금을 수퍼필링에 적용하기 전에 양극 과정이 SPS와 PEG-Cl⁻의 경쟁 흡착에 어떠한 영향을 미치는지 확인하였다. 양극 과정이 선흡착된 PEG-Cl⁻을 빠르게 SPS로 치환하는 것을 확인하였고, 상대적으로 긴 리벌스 타임과 높은 양극 전압이 인가될 때 가속화 정도가 증가하는 것을 알 수 있었다. 구리의 수퍼필링은 첨가제의 흡착에 기인한 결과이므로 첨가제 치환반응의 가속화는 수퍼필링 특성을 변화시킬 수 있다. 따라서 양극 과정의 조건과 수퍼필링 특성의 관계에 대해 알아 보았다. 그 결과, 55 nm의 폭을 가지는 트렌치에서 정전압 도금에 비해 펄스-리벌스 전해 도금이 훨씬 우수한

수퍼필링 특성을 나타내는 것을 확인하였다. 또한, 낮은 종횡비를 가지는 트렌치의 모서리 부분에서도 펄스-리벌스 전해 도금이 훨씬 빠른 구리의 전착을 나타내는 것을 알 수 있었다. 이와 같은 결과는 첨가제 치환 반응의 가속화로 인한 SPS의 농도 증가에 기인한 결과로 해석된다.

 박막 특성 및 수퍼필링의 특성 향상을 고려해보면, 전압 파형의 변화, 즉 펄스 및 펄스-리벌스 전해 도금은 현재 구리 배선공정에서 이슈가 되는 다양한 문제를 해결할 후보로 생각된다. 이는 더욱 빠르고 신뢰성 높은 전자 소자의 형성을 가능하게 해줄 것으로 예측할 수 있다.

주요어: 구리, 배선, 펄스 전해 도금, 펄스-리벌스 전해 도금, 박막 특성, 수퍼필링

학　번: 2007-21174

Appendix-Superfilling of Cu-Ag

I. Introduction

As mentioned in Chapter I, damascene process has been widely used for fabricating Cu interconnection, and the concerns originated from the reduction of interconnection dimension are issued.[1] In the aspect of electromigration and mechanical stress, the introduction of secondary metal to Cu is one of the candidates for resolving this issue.[2-5] Since the co-deposited secondary metal provides the additional probability of electron scattering, the reduction of electrical conductivity is an inevitable corollary. Therefore, the secondary metal should be precisely chosen by considering the conductivity when Cu and secondary metal are co-deposited. Among various metals, Ag-containing Cu film showed the lowest resistivity of about 2.4 $\mu\Omega$·cm which was comparable to pure Cu.[6] On the other hand, the electrical resistivity of other bimetallic films such as Cu-Co, Cu-Mg, and Cu-Ag, ranged between 3.2 and 6.4 $\mu\Omega$·cm.[6]

In general, Cu-Ag films have been prepared by electron beam evaporation, electrodeposition in supercritical fluid, and the deposition from the melted stage in vacuum.[4,5,7,8] Regarding to the application in the fabrication of interconnection, low

temperature and wet-process of Cu-Ag co-deposition is the most appropriate and controllable. Therefore, the determination of the electrolyte was the most important aspect in developing the electrodeposition of Cu-Ag. General Cu electrodeposition was conducted in sulfuric acid-based electrolyte, which consistently contained halogen ions to achieve better film properties and superfilling. However, Ag could not be deposited with the halogen ions because the precipitation was easily formed by the spontaneous reaction between Ag and halogen ions in the electrolyte. Therefore, cyanide-based aqueous solution was chosen as a basic electrolyte instead of sulfuric acid-based electrolyte. In addition, it has been reported that the superfilling of Ag was enabled by the use of cyanide-based electrolyte.[9-11] By using this electrolyte, Cu-Ag film was successfully deposited by the electrodeposition, and it showed comparable resistivity to pure Cu after the annealing.[12] However, the bimetallic superfilling of Cu-Ag using electrodeposition and its mechanism are not investigated.

Superfilling of Ag or Au using KSeCN, $Pb(NO_3)_2$, $TlNO_3$, thiourea (TU), and benzotriazole (BTA) in cyanide-based electrolyte has been previously reported.[9-11] TU is the only additive known as a suppressor for Ag reduction, whereas the other additives act as accelerators for both Ag and Au electrodeposition. One of the distinctive characteristics of the Ag or Au superfilling in cyanide-based electrolyte is

the relatively faster surface diffusion of the accelerator compared to Cu superfilling in sulfuric acid-based electrolyte, implying high value of D/wv_0 for Ag or Au superfilling. This resulted in the reduction of superfilling performance, therefore, the additional additive which could retard the surface diffusion of accelerator should be introduced to improve the superfilling performance.

In this research, the superfilling of Cu-Ag was attempted with KSeCN and TU in cyanide-based electrolyte. Chronoamperometry with various concentrations of KSeCN and TU was carried out to clarify the effects of each additive. The changes in the superfilling phenomenon with various concentration of $KAg(CN)_2$ were investigated. The mechanism of Cu-Ag superfilling was clarified by tracing the atomic distribution of Cu and Ag within the filling feature. Finally, the properties of Cu, Cu-Ag, and Ag films were compared, which were deposited under the superfilling conditions.

II. Experimental

2-1. Superfilling of Cu-Ag

Superfilling of Cu-Ag was conducted with the three-electrode system consisted of the patterned wafer, Cu wire, and Ag/AgCl electrode as the working, counter and reference electrodes, respectively. The structure of the patterned wafer was Cu seed layer (60 nm, PVD) / Ta (7.5 nm, PVD) / TaN (7.5 nm, PVD) / SiO_2. The width of trench with Cu seed layer was in the range between 120 nm and 4.5 μm, and the depth was 400 nm. The electrolyte contained 0.3 M of CuCN, 0.6 M of KCN. The concentration of $KAg(CN)_2$ was changed from 0 to 10 mM. KSeCN and TU were additionally put into the electrolyte, and their concentrations were 5 μM and 0.1625 mM. The deposition potential was fixed at -1.3 V with respect to Ag/AgCl reference electrode. The superfilling was performed by a PAR 273A potentiostat (EG&G Princeton Applied Research Corporation).

The profile of gap-filling was inspected by field emission scanning electron microscope (FESEM, S-4800, Hitachi). The distribution of Cu and Ag at the corner of low-aspect-ratio trench was analyzed by FESEM (JSM-6701F, JEOL)-energy

dispersive X-ray spectrometer (EDS, INCA Energy, Oxford Instruments Analytical Ltd.). In addition, the distributions and the atomic contents of Cu and Ag inside the high-aspect-ratio trench were surveyed by transmission electron microscope (TEM, JEM-2100F, JEOL) after the sample preparation using focused ion beam (FIB, Nova 600 NanoLab, FEI).

2-2. Electrochemical analyses

  The chronoamperometry was performed with the Cu rotating disk electrode (RDE) having 0.1256 cm^2 of the active area. The rotating speed was fixed at 300 rpm. To clarify the role of each additive on either Cu or Ag reduction, the chronoamperometries were carried out in two kinds of electrolyte; (i) CuCN, KCN, (ii) CuCN, KCN, and $KAg(CN)_2$. The concentrations of KSeCN and TU were varied from 0 to 20 μM and 0 to 0.65 mM, respectively. The applied potential was kept to -1.3 V and the average current for 100 s was investigated.

2-3. Electrodeposition of Cu, Cu-Ag, and Ag films

The electrodeposition of Cu, Cu-Ag, and Ag films was also conducted in three-electrode system. Instead of patterned wafer, the planar substrate was employed as the working electrode, and its structure was Cu (PVD, 40 nm) / Ta (PVD, 7 nm) / Si. In the case of Cu and Cu-Ag electrodeposition, Cu wire was used as the counter electrode. On the contrary, Ag electrodeposition was performed with Ag wire. The deposition amounts for Cu, Cu-Ag, and Ag films were 380, 300, and 250 mC/cm^2 respectively. Cu-Ag film was deposited in the aqueous electrolyte containing 0.3 M CuCN, 0.6 M KCN, 5.0 mM KAg(CN)$_2$, 5 μM KSeCN, and 0.1625 mM TU by applying -1.3 V (vs. Ag/AgCl reference electrode). The electrodeposition of Cu film was carried out in the aqueous electrolyte including 0.25 M CuSO$_4$, 1.0 M of H$_2$SO$_4$, 88 μM polyethylene glycol (PEG, Mw=3,400), 1 mM NaCl, and 50 μM bis(3-sulfopropyl) disulfide (SPS) with applying -0.2 V (vs. Ag/AgCl reference electrode). Ag film was electrodeposited in the electrolyte containing 0.23 M KAg(CN)$_2$, 3.4 M KCN, and 5 μM KSeCN by applying -0.2 V (vs. open circuit potential). All of the electrodeposition was carried out using a PAR 273A potentiostat (EG&G Princeton Applied Research Corporation). The annealing was carried out at 350°C for 1 hr in N$_2$-atmosphere.

2-4. The characterization of film properties

The crystal information was investigated by X-ray diffraction (XRD, D8 Advance, Bruker). The grain sizes were calculated from the full width at half maximum (FWHM) of each peak from XRD patterns using Scherrer's formula. The surface morphology and RMS roughness were obtained by atomic force microscope (AFM, XE-150, Park Systems). The electrical conductivities of these films were calculated from the thickness and sheet resistance measured by FESEM and 4-point probe (CMT-SR1000N, Chang Min Tech Co.) respectively. The oxidation resistance was characterized from the resistivity changes before and after oxidation, and the oxidation was performed at 250°C for 30 min in the atmosphere. The mechanical hardness was measured by nanoindenter (MTS XP, MTS Systems Corporation).

III. Results and discussion

3-1. Superfilling of Cu-Ag and its mechanism

The representative profiles of electrodeposited Cu-Ag at various trenches are shown in Fig. 1. The successful superfilling without void formation inside the filling feature was clearly observed with TU and KSeCN, showing the apparent bumps and the convex deposits at the corners of low-aspect-ratio trenches. Under the condition in the absence of TU and KSeCN represented in Figs. 2(a) and (b), the rough surface and the voids inside the trenches were observed. On the other hand, each addition of TU (Figs. 2(c) and (d)) or KSeCN (Figs. 2(e) and (f)) improved the surface roughness, however, the voids and seams were formed. Especially, KSeCN reduced the overall uniformity although it improved the surface roughness. That is, the co-addition of TU and KSeCN is essential to obtain successful superfilling. As KSeCN is known as the accelerator to Ag electrodeposition, it can be speculated that the superfilling was produced by its accumulation according to the area reduction. In addition to that, TU improved the uniformity of Cu-Ag electrodeposition.

To determine the effects of TU and KSeCN, the deposition profiles at low-aspect-ratio

trenches with TU and the combination of TU and KSeCN were investigated as depicted

in Fig. 3. As can be seen in Figs. 3(a) and (b), TU slightly enhanced the deposition at

the corner of the trench. The profile in Fig. 3(b) was almost identical to the Au gap-

filling at the low-aspect-ratio trench. This implied that TU has the potential to produce

bottom-up filling. However, its effect was not sufficient to induce perfect superfilling

at the relatively narrow trenches as shown in Figs. 2(c) and (d). On the other hand, the

combination of TU and KSeCN interestingly resulted in the formation of remarkable

bumps (Fig. 3(c)) as well as convex profiles at the corners of the low-aspect-ratio

trench (Fig. 3(d)). These results enable us to surmise that there is an additional factor

retarding the surface diffusion of accelerators based on the fact that the continuous

growth of bumps and the formation of convex deposits could be obtained by highly

accumulated and stationary accelerators, originated from the area reduction at the

bottom of high-aspect-ratio trench and the corner of low-aspect-ratio trench.

 The electrochemical impacts of each adsorbate on Cu and Cu-Ag electrodeposition

can be clarified from the variations of average current measured from

chronoamperometry with varying the concentrations of TU and KSeCN, and the results

are shown in Fig. 4. It was apparent in Fig. 4(a) that TU did not make continuous

acceleration on both Cu and Cu-Ag electrodeposition regardless of KSeCN addition.

The average current with the addition of TU increased below 0.8125 mM, followed by the saturation. Considering this behavior based on CEAC model, the increment of TU surface coverage according to the area reduction could not produce the local acceleration of deposition rate. By contrast, it was observed in Fig. 4(b) that KSeCN continuously resulted in the acceleration of Cu-Ag reduction as the concentration of KSeCN increased even though the average current of Cu reduction was almost constant regardless of its concentration. This implied that KSeCN had no impact on Cu reduction, and its effect was limited to Ag. This suggested that the limited acceleration of KSeCN on Ag reduction can be strongly associated with the superfilling of Cu-Ag. Furthermore, this limited acceleration has the potential to change the distribution of Cu and Ag within the filling features because the degree of area reduction corresponding to the accumulation of KSeCN was different according to the location in the trench. The degree of area reduction at the bottom of trench was much higher compared to the top or side of trench. Therefore, relatively high concentration of KSeCN at the bottom can be expected, locally accelerating the electrodeposition with higher concentration of Ag.

From the results of deposit profile and electrochemical analyses, it can be speculated that the superfilling performance is also affected by the concentration of $KAg(CN)_2$

corresponding to the amount of co-deposited Ag because the main driving force of superfilling is the acceleration of KSeCN limited to Ag reduction. The deposition profiles with changing the concentration of $KAg(CN)_2$ are represented in Fig. 5, and the atomic concentration of Ag was measured from Cu-Ag films deposited on the non-patterned substrates. As represented in Fig. 5(a), superfilling of Cu without Ag failed, and voids could be observed at the top of the trench. Below 5 mM of $KAg(CN)_2$, the superfilling of Cu-Ag was successfully achieved using a combination of KSeCN and TU. At 10 mM, the gap-filling failed due to the irregular growth of Cu-Ag. It is important to highlight that a considerable bump was formed with 5 mM of $KAg(CN)_2$. In contrast, only vague bumps were observed with 2.5 mM, even though defect-free filling was obtained. The deposit profiles at the corner of low-aspect-ratio trenches were also changed by the concentration of $KAg(CN)_2$, as displayed in Fig. 6. Based on these results, it is clearly confirmed that the concentration of co-deposited Ag also affects the superfilling phenomenon through altering the effect of additives.

From the point that the acceleration of KSeCN was limited to Ag reduction, it can be speculated that the concentration of co-deposited Ag was changed by the extent of accumulated accelerators. Therefore, the atomic distributions of Cu and Ag provide the information on Cu-Ag superfilling.

The evolution of deposit profile at the corner of low-aspect-ratio trench was first predicted based on CEAC model with local acceleration of Cu-Ag electrodeposition at the corner induced by the accumulated KSeCN, and the schematic diagram of profile evolution is displayed in Fig. 7(a). As the electrodeposition progressed, the area at the corner was shrunken resulting in the accumulation of KSeCN. Since KSeCN continuously accelerated Ag reduction, the deposition rate was locally increased at the corner, consequently forming the convex profile. The prerequisite of the convex profile is to maintain the acceleration effect throughout the electrodeposition by confining adsorbed KSeCN, which might be originated from the co-adsorbed TU. Comparing the electrodeposition rate of Cu, Ag, and Cu-Ag on the planar surface (Fig. 8), the electrodeposition of Cu-Ag exhibited 16.6% and 15.0% of Cu and Ag deposition rate, respectively. Based on the consideration of dimensionless factor, D/wv_0, implying the superfilling ability, the surface diffusion of KSeCN should be strongly retarded to produce the similar superfilling ability. Since the continuous bump formation at the corner of the trench has not been reported in Cu and Ag superfilling, it was simply expected that the surface diffusion of KSeCN was reduced more than 5 times. In order to certify local acceleration of KSeCN, the atomic distribution of Cu and Ag was analyzed, and the results are represented in Fig. 7(b). It clearly indicated that the

deposition of Ag was concentrated at the corner although Cu was almost uniformly distributed in whole deposit. The Cu-Ag deposited with only TU addition was also inspected, however, both Cu and Ag were uniformly distributed as exhibited in Fig. 7(c). On the basis of this, it can be concluded that the accumulation of KSeCN according to the area reduction resulted in the evolution of convex profile with more Ag.

The investigation on the superfilling of Cu-Ag and the atomic distribution within the filling feature with relatively high-aspect-ratio was attempted by TEM. Successful superfilling without any void formation was also observed in Figs. 9(a) and (b). In addition, it was interesting that the deposits can be divided into three regions (▲, ●, and ◆) based on the brightness in dark field TEM images represented in Figs. 9(c) and (d). Note that the brightness of the regions was in order of ▲ < ● < ◆. Since the brightness in dark field image is depending on the atomic number, the contrast difference was the result from the distribution of Cu and Ag. The atomic number of Ag was higher than that of Cu, thus the relatively bright region could contain more Ag. In addition, it was important to highlight that the shape of boundary almost coincided with the interface where the line density was sharply changed in the CEAC prediction (Fig. 10). Therefore, this strongly suggested that the investigation on the three regions

with different brightness could provide considerable information on superfilling of Cu-Ag.

Line scanning of atomic distribution was attempted to precisely determine the distribution of Cu and Ag in three regions, and the results were represented in Fig 11. It was performed at four different locations which were marked in Fig. 11(a); each line crossed (i) only ◆, (ii) ▲, ●, and ◆, and (iii), (iv) ▲ (relatively thin), ●, and ◆ and Si. Since the contrast was almost constant along line (i), $K\alpha1$ intensities of Cu and Ag were not varied according to the positions as shown in Fig. 11(b) (upper left). On the contrary, the intensities were remarkably changed with the other lines covered the regions with different contrast. The interfaces between the regions were marked in Fig. 11(b); between ▲ and ●: red dotted, between ● and ◆: blue dotted, and between Si and ▲: black dotted lines. From line (ii) (upper right in Fig. 11(b)), it was confirmed that the region ▲ was fully composed of Cu meaning Cu seed layer deposited by physical vapor deposition prior to Cu-Ag electrodeposition. Ag peak observed at the interface between the regions ▲ and ● is originated from the displacement reaction before initiating the electrodeposition. In addition, it was ascertained that the region ◆ contained more Ag compared to the region ● (lower left and right), which was well-matched to the previous expectation from the contrast

difference. On the basis of the results, the enhancement of Ag electrodeposition was limited to inside of the trench where KSeCN was accumulated by the area reduction. That is, the superfilling of Cu-Ag followed CEAC model, and its driving force was came from the acceleration effect of KSeCN on Ag electrodeposition.

The evolution of deposition profile and the superfilling ability was depending on the ratio between the deposition rate and surface diffusion of adsorbed accelerator D/wv_0 as mentioned above. The simulations of deposition profile according to D/wv_0 are revealed in Fig. 10. In CEAC predictions, the inverse of line density corresponded to the local deposition rate, reflecting the degree of accelerator accumulation. As the surface diffusion became considerably rapid shown in the right of Fig. 10, the deposition rate was almost constant within the trenches. On the contrary, when the adsorbed accelerators are strongly confined, the deposition rate was locally enhanced at the center of the trench as shown in the left of Fig. 10. Comparing the boundary in Fig. 9(c) and these CEAC predictions, the boundary between the regions ◆ and ● was nearly identical to the interface where the line density in CEAC prediction was sharply changed (left two predictions in Fig. 10). Note that the regions with more Ag (◆) and less Ag (●) correspond to that with lower and higher line density, respectively. Since the considerable surface diffusion could result in the flat profile at the top of region

with higher line density as well as the continuous distribution of Cu and Ag, the domed profile at the top of region ● and the obvious division of Cu-Ag deposit with different Ag content supported that the surface diffusion of KSeCN was restrained. As mentioned above, the kinetics of Cu-Ag electrodeposition was much lower than that of Cu or Ag, therefore, the surface diffusion of KSeCN during Cu-Ag electrodeposition was more retarded compared to Cu and Ag. From the point that the region with relatively low line density contained more Ag implying high degree of KSeCN accumulation, it can be suggested that Cu-Ag superfilling greatly followed CEAC model.

The impact of the acceleration in the region ◆ should be also dependent on the position in the trench predicted by the line density change as displayed in Fig. 10. This is originated from the difference in the degree of accelerator accumulation. When the surface diffusion is strongly restrained, the accumulation degree can be continuously increased. From the left of Fig. 10, the acceleration, i.e. the inverse of line density, was increased from the bottom of trench, and it was maximized at the region where the distance between the growing surfaces from two side walls was minimized. After this, the acceleration was reduced again because the deposition area was extended. The validity of CEAC model to Cu-Ag superfilling can be determined by tracing the

content of Ag in the region ◆. The locations where the atomic concentrations of Cu

and Ag were inspected are marked in Fig. 12(a). Note that the points from 1 to 5 were

in the region ◆ and the point 6 and 7 were located in the region ●. The atomic

concentrations of Cu and Ag are represented in Fig. 12(b). As identical to the results of

line scanning, the region ◆ has more Ag compared to the region ●. The atomic

concentration of Ag in the region ● was in the range between 7.73 and 9.28 atom%

as shown in Fig. 12(b). These values were comparable to 7.9 atom% from Cu-Ag

electrodeposition on the planar surface meaning no impact of surface curvature. This

implied that the deposition from the top and side walls could be treated as similar to

the flat surface. In contrast, it was figured out that the atomic concentration of Ag was

dependent on the position in the region ◆, and it was in the range between 12.6 and

17.9 atom%. The content of Ag was increased from point 1 to 3, followed by the

decrease in the values from point 3 to 5. The schematic diagram indicating the atomic

distribution of Ag according to the locations is represented in Fig. 12(c). Since the

atomic concentration of Ag reflected the acceleration effect of KSeCN, it enabled us to

estimate the accumulation degree of accelerator as mentioned above. That is, the

maximized content of Ag at point 3 corresponded to the maximum acceleration by

KSeCN. Comparing the atomic distributions and the expectation from CEAC

prediction, it is natural to suggest that the acceleration effect changed by the degree of KSeCN accumulation was exactly identical to CEAC prediction. This leads us to finally conclude that Cu-Ag superfilling definitely follows CEAC model with low surface diffusion of adsorbed accelerator. In addition, it was interesting to note that the superfilling of Cu-Ag was achieved with the limited acceleration on the co-deposited Ag below 17.9 atom%, implying that the bimetallic superfilling does not need the both acceleration effects on two metal components. Based on this, the various bimetallic interconnections with bifunctionality such as Cu-Ni can be achieved with the limited acceleration of adsorbates on the one metal component.
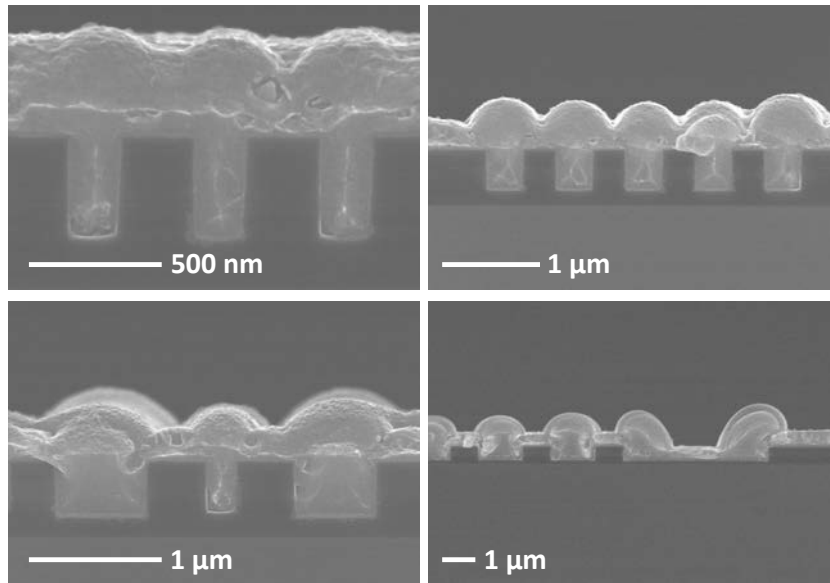
Fig. 1. The profiles of Cu-Ag deposited with KSeCN and TU at the trenches with various aspect ratios.
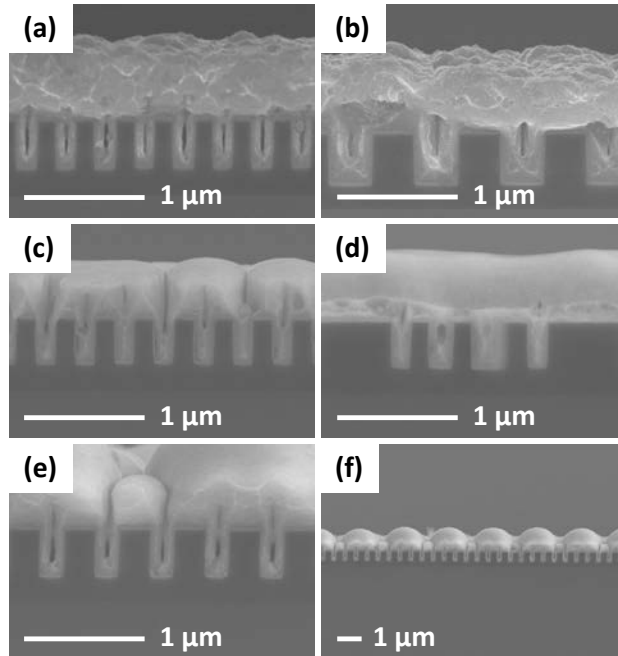
Fig. 2. The profile of Cu-Ag electrodeposited (a), (b) without additives, (c), (d) with

TU, and (e), (f) with KSeCN.
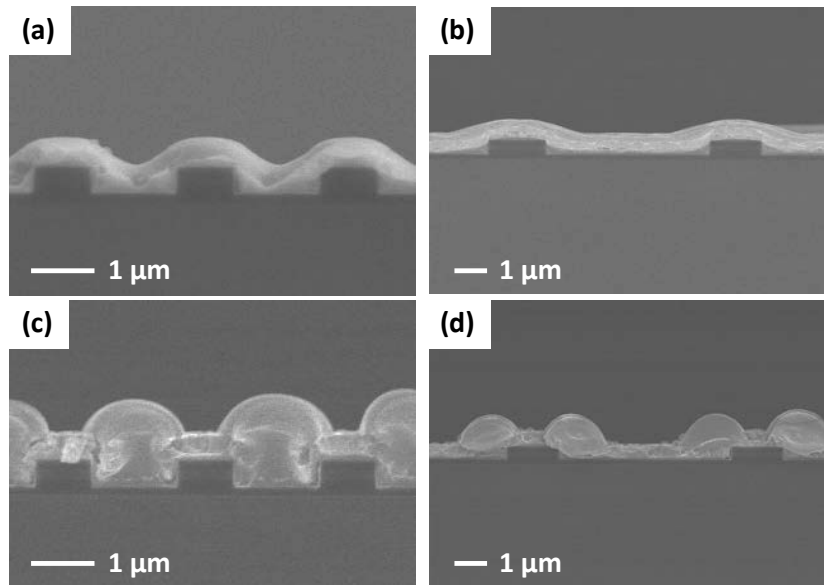
Fig. 3. The gap-filling profiles of Cu-Ag with (a), (b) 0.1625 mM TU, and (c), (d) 5 μM KSeCN and 0.1625 mM TU at the low-aspect-ratio trenches.
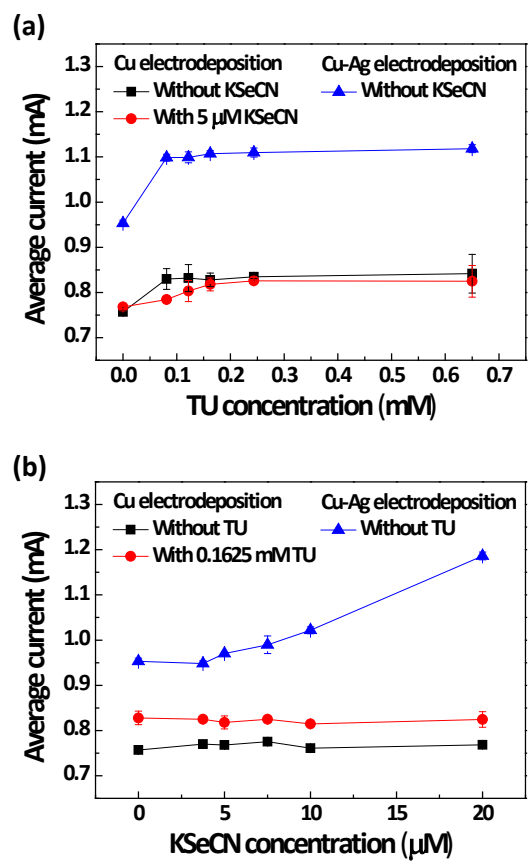
Fig. 4. The changes in the average current of chronoamperometry according to the concentrations of (a) TU and (b) KSeCN.
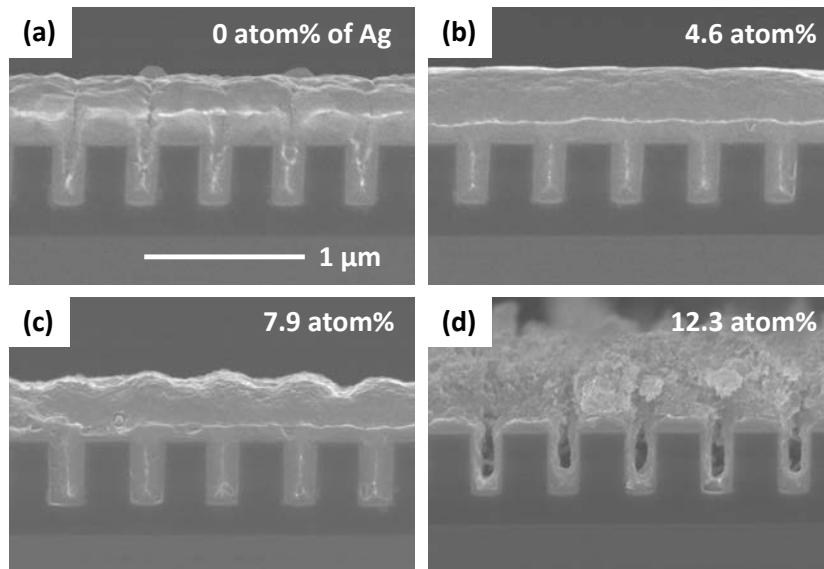
Fig. 5. The gap-filling profiles of Cu-Ag with (a) 0 mM, (b) 2.5 mM, (c) 5.0 mM, and

(d) 10.0 mM of $KAg(CN)_2$ in the presence of 5 μM KSeCN and 0.1625 mM TU; the

deposition amount was fixed at 400 mC/cm^2.
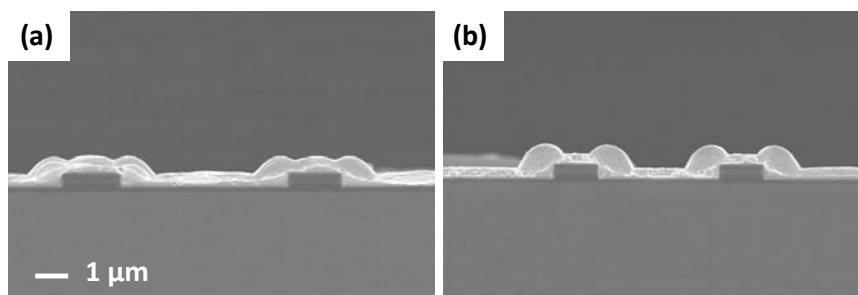
Fig. 6. The deposition profiles of Cu-Ag with (a) 2.5 mM, and (b) 5.0 mM of

KAg(CN)$_2$ in the presence of 5 μM KSeCN and 0.1625 mM TU.

(a)

(b)
Si
1 µm
Cu
Ag

(c)
Si
1 µm
Cu
Ag

■ : PVD Cu seed layer

■ : Cu-Ag

▨ : Cu-Ag (affected by accumulated KSeCN)
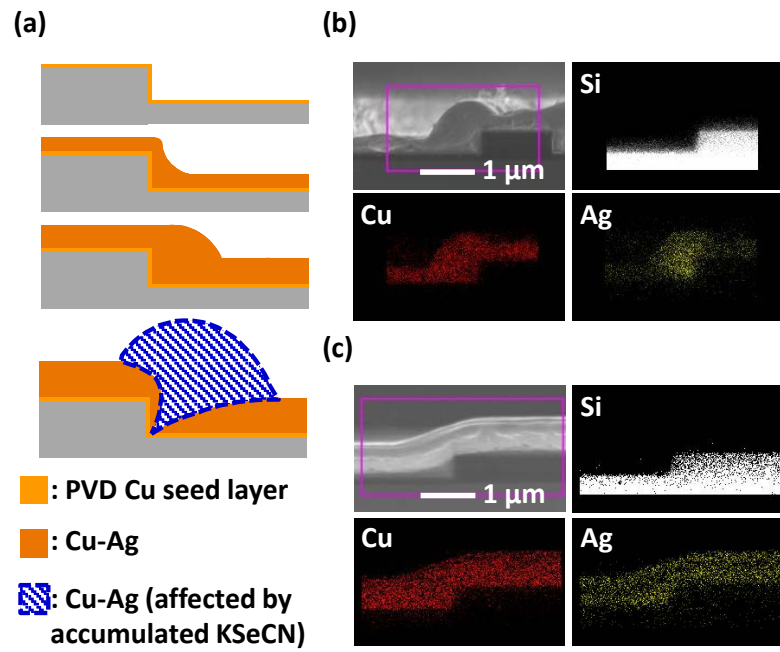
Fig. 7. (a) The prediction of deposition profile evolution at the corner of low-aspect-ratio trench and the distributions of Cu, Ag, and Si in the deposits with (b) KSeCN and TU, and (c) TU.
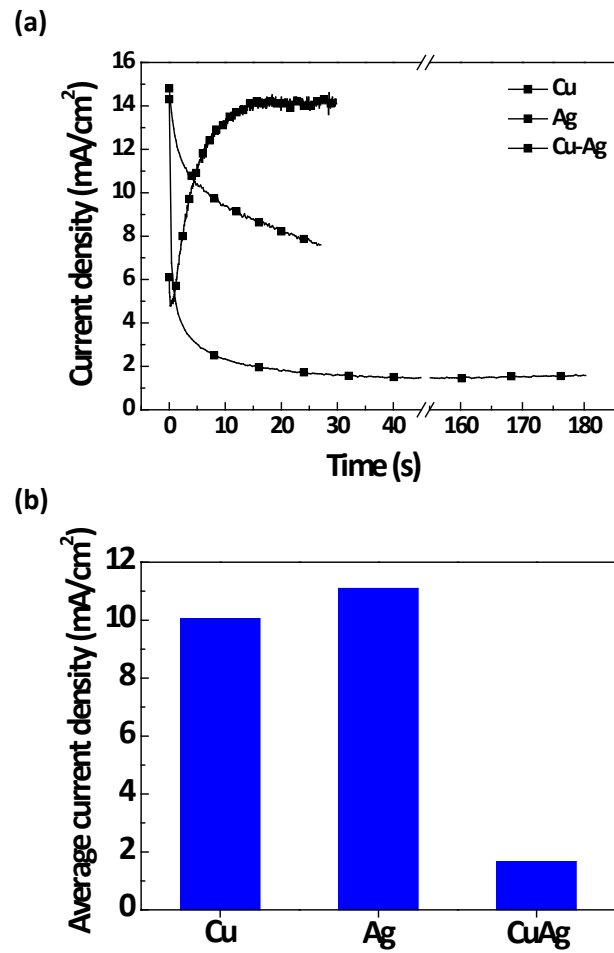
Fig. 8. (a) The current profiles of Cu, Cu-Ag, and Ag electrodeposition and (b) the average current densities.
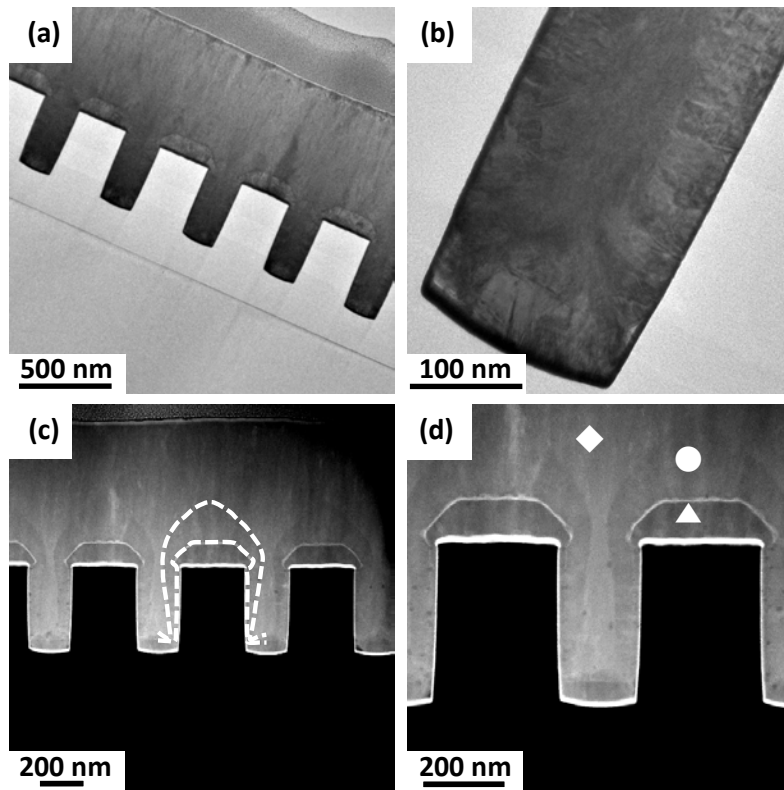
Fig. 9. (a), (b) Bright field and (c), (d) dark field TEM images of Cu-Ag in the trenches.
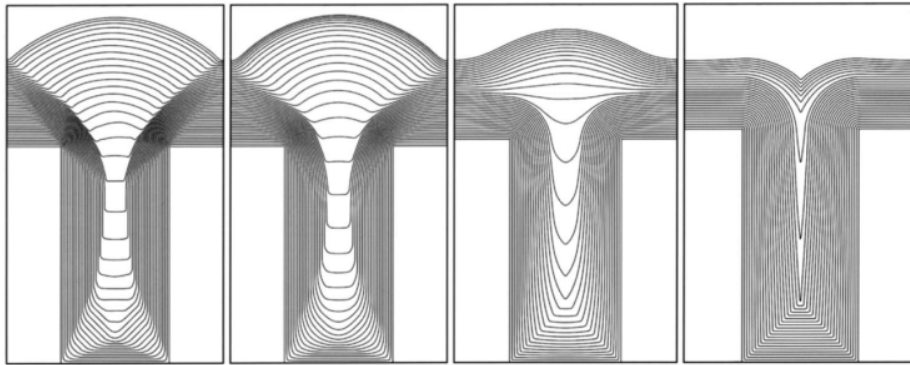
Fig. 10. CEAC predictions of Cu superfilling with various dimensionless diffusion coefficients D/wv_0 (left to right): 0.01, 0.1, 1, and 10.
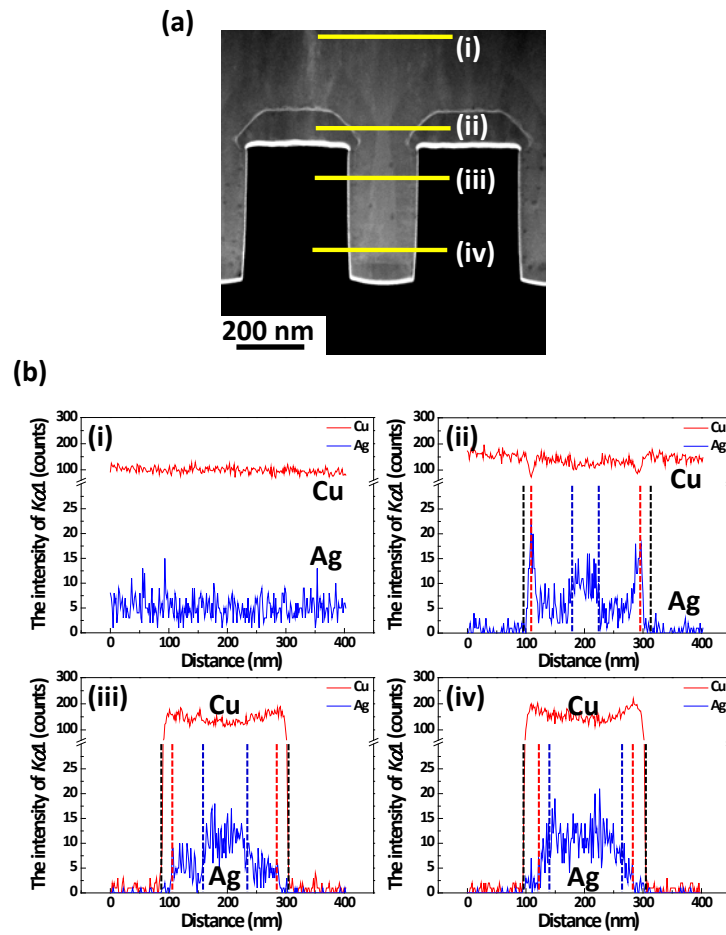
Fig. 11. (a) The positions of line profiling measurement by TEM EDS and (b) the distributions of Cu and Ag.

(a)

(b)

(c)
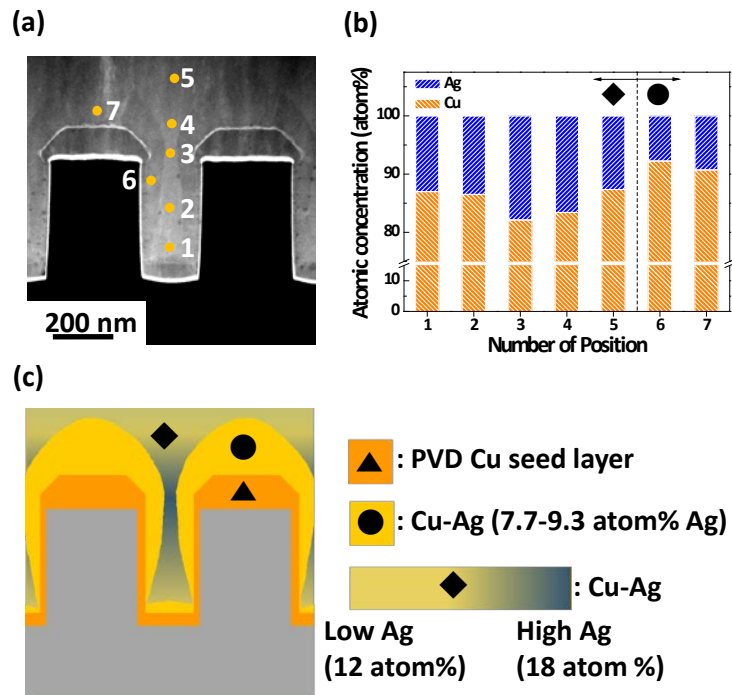
Fig. 12. (a) The positions of EDS measurement, (b) the atomic concentrations of Cu and Ag according to the positions, and (c) the schematic diagram of Cu and Ag distributions.

3-2. The characteristics of Cu-Ag film

From now on, the properties of Cu, Ag, and Cu-Ag films deposited on planar surfaces are introduced. It is hard to compare the properties of Cu, Ag, and Cu-Ag deposited within the trenches, therefore, the properties were investigated after the electrodeposition on planar substrate. Since the superfilling of Cu and Ag has been reported from previous researches, the electrodeposition was performed under the condition where the superfilling was achieved. The impact of annealing on the properties was also clarified. The detail conditions are introduced in experimental section.

XRD patterns of Cu, Cu-Ag, and Ag films before and after the annealing are depicted in Figs. 13(a) and (b), respectively. XRD patterns with the normal intensity instead of log scale are also represented in Figs. 14(a) and (b). It revealed that Cu and Ag films only consisted of (111) planes, and the intensities were increased after the annealing implying the grain growth. On the contrary, the four peaks corresponding to pure Ag, pure Cu and Ag-rich and Cu-rich Cu-Ag solid solutions were observed in the as-deposited Cu-Ag film (Fig. 15). From the peak position and Vegard's law, the composition of Ag-rich and Cu-rich Cu-Ag solid solutions were $Cu_{29}Ag_{71}$ and $Cu_{91}Ag_9$

even though thermodynamically allowed composition of Ag was below 0.08 atom% at

room temperature. It was speculated that the driving force of the solid solution

formation with higher degree of mixing than thermodynamically allowed miscibility

was the relatively high applied potential. That is, the results implied that the electrical

force could form the metastable state between Cu and Ag. It was reported that Cu-Ag

solid solution with uniform composition could be obtained by applying the mechanical

energies such as the ball milling and mechanical torsion to Cu-Ag films. From the

point that the considerable amount of pure Cu and Ag was deposited, the electrical

force, i.e. applied potential, was not enough to obtain the uniform solid solution. The

intensity of each peaks were considerably low compared to Cu and Ag films (Table 1).

It was originated from the inhibition of grain growth and development of each crystal

orientation by the co-deposition of Cu and Ag. In general electrodeposition, the

sluggish electrodeposition with low overpotential more developed the orientation with

relatively large grain size. Although the kinetics of Cu-Ag electrodeposition was the

slowest revealed in Fig. 8, the impact of co-deposition was dominant to reduce both the

development of orientation and the grain size. After the annealing, the peaks

corresponding to the Cu-Ag solid solutions disappeared and the intensity of both Cu

and Ag (111) peaks were enhanced. This change was ascribed to the segregation of Cu

and Ag and the grain growth during the annealing. The grain sizes of those films can be simply calculated by Scherrer's formula providing the relationship between full width at half maximum (FWHM) of each peak observed in XRD patterns and the average grain size. The calculated grain sizes were listed up in Table 2. It was confirmed that the grain size of Cu-Ag film was much smaller than Cu or Ag films, and it was enlarged by the annealing process. The grains in Cu or Ag films also grew during the annealing, however, the degree of grain growth was the highest with Cu-Ag films. The surface morphologies of Cu, Cu-Ag, and Ag films and their average root-mean-square (RMS) roughness are represented in Fig. 16. The size of surface protrusion of the films were in order of Ag > Cu > Cu-Ag, corresponding to the behavior of grain size. Similar to grain size, its size was increased after the annealing. On the contrary, the tendency of RMS roughness shown in Fig. 16(g) was not identical to the grain size behavior. It was observed that Cu film has the lowest surface roughness among these films regardless of annealing. This was originated from the relatively large groove formation of Cu-Ag film. The size of surface protrusion is exactly reflected the grain size, however, the groove is not because it is composed of few grains. The electrical conductivity, oxidation resistance, and mechanical hardness of Cu, Cu-Ag, and Ag films were investigated and understood based on the grain size and crystal structure.

The electrical conductivity of Cu, Cu-Ag, and Ag films before and after the annealing is represented in Fig. 17. It was observed that the conductivity of as-deposited Cu-Ag films was relatively low compared to Cu or Ag, however, it was increased to comparable values to Cu or Ag after the annealing. The electrical conductivity of metal films is inversely depending on the probability of electron scattering related to phonon, grain boundary, surface roughness, and impurities. The impact of impurity with electrodeposited film is not major factor to determine the electrical conductivity in general. In addition, the surface roughness can be treated as the minor factor when the thickness of film is over few hundred nanometers because the impact of the surface roughness on the resistivity is inversely depending on the thickness. That is, the effect of surface roughness is diminished as the film thickness is increased. In the aspect of phonon, it was related to intrinsic property also depending on the temperature and the kind of metal, which can be found from the difference of the bulk conductivities of Ag and Cu. Based on Mayadas-Shatzkes equation, the enlargement of grains is the increasing factor of electrical conductivity. From Table 2, the grain sizes of as-deposited and annealed Cu and Ag films were almost similar, the electrical conductivity difference between Cu and Ag can be found from the characteristics of phonon. Regarding to Cu-Ag film, both impacts from phonon and grain size affected

the electrical conductivity regardless of annealing. In detail, since the conductivity of

annealed Cu-Ag film with enlarged grains was comparable to Cu or Ag, which showed

97.9% of Cu and 88.3% of Ag conductivities, the major factor determining the

resistivity of as-deposited film was the grain size. On the basis of these results, it can

be suggested that the demerit of Cu-Ag in the aspect of electrical property is not

considerable, although the most important problem of bimetallic film consisting of Cu

and secondary metal is the severe deterioration of conductivity. Since the resistance

against electromigration of Cu-Ag higher than monometallic Cu or Ag, therefore, it can

be highlighted that the realization of Cu-Ag interconnection without severe decrease in

the conductivity maintains the advantage and makes up for the weakness compared to

Cu interconnection.

The oxidation resistance was measured from the resistivity change before and after

the oxidation ($\rho_{after\ oxidation}/ \rho_{before\ oxidation}$). The oxidation was performed at 250°C in the

atmosphere, thus, the grain growth could be progressed similar to the impact of

annealing, which can be observed in Fig. 18 revealing the reduction of resistivity after

the oxidation, especially as-deposited Cu-Ag film. Therefore, the annealed films are

suitable in order to compare the oxidation resistance, and the results are shown in Fig.

18. It was confirmed that the resistivity of Cu-Ag and Ag films were not increased

implying no oxidation. On the contrary, 14% of resistivity of Cu film was ascended by the oxidation at the surface. As can be seen in Fig. 19, the surface of Cu-Ag film was composed of more Ag compared to the concentration inside the film. This was originated from the displacement reaction after the electrodeposition. The reduction potential of Ag is more positive than Cu, thus the displacement reaction is spontaneous. In addition, the atomic concentration of Cu-Ag film after the annealing was increased at the surface, which was ascribed to the Ag segregation to the surface through the grain boundaries. Therefore, high oxidation resistance of Cu-Ag film is ascribed to the surface with considerable large amount of Ag. The additional advantage of Cu-Ag interconnection can be found in the oxidation resistance.

The mechanical hardness of these films was finally investigated by nanoindentation. The bulk hardness of Cu is 1.47 times higher than that of Ag, therefore, it can be easily expected that Cu film has much higher hardness compared to Ag.[16] In the case of Cu-Ag film, the impact of Ag co-deposition reduced the grain size as explained above, thus, it could increase the mechanical hardness through both precipitation and grain boundary hardening mechanisms, which can be described by Hall-Petch relation.[17,18] The measured hardness of as-deposited film is represented in Fig. 20. Same to the expectation, the hardness of these films is in order of Cu-Ag > Cu > Ag. Cu-Ag film

showed 15.9% and 222.9% higher hardness compared to Cu and Ag films, respectively.

Table 1. The Peak Intensities Measured from XRD Patterns Before and After Annealing.

Peak intensity (counts)		Ag (111)	Ag-rich Cu-Ag	Cu-rich Cu-Ag	Cu (111)	Cu (200)
Cu film	As-deposited	n.a.	n.a.	n.a.	65033	n.a.
	Annealed				344459	
Cu-Ag film	As-deposited	1446	64	13173	10531	n.a.
	Annealed	30326	n.a.	n.a.	141637	250
Ag film	As-deposited	108349	n.a.	n.a.	3325	n.a.
	Annealed	111991			4651	

Table 2. The Grain Sizes of Cu, Cu-Ag, and Ag Films Calculated using Scherrer's Formula from the Peaks Observed in XRD Patterns.

Grain size (nm)		Ag (111)	Ag-rich Cu-Ag	Cu-rich Cu-Ag	Cu (111)
Cu film	As-deposited	n.a.	n.a.	n.a.	36.1
	Annealed				73.5
Cu-Ag film	As-deposited	9.8	12.2	21.2	26.8
	Annealed	32.4	n.a.	n.a.	59.9
Ag film	As-deposited	40.0	n.a.	n.a.	n.a.
	Annealed	86.0			
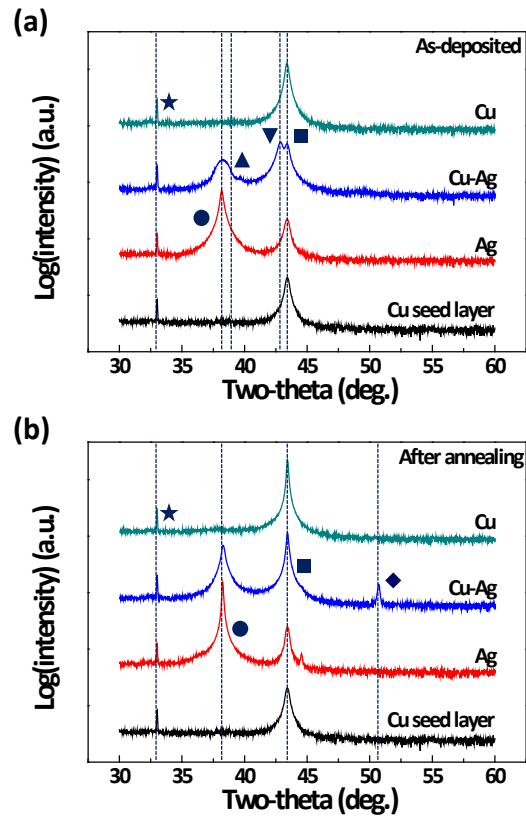
Fig. 13. XRD patterns of Cu, Cu-Ag, and Ag films deposited with the conditions of superfilling (a) before and (b) after the annealing (★: Si substrate, ●: Ag (111), ▲: Ag-rich Cu-Ag, ▼: Cu-rich Cu-Ag, ■: Cu (111), ◆: Cu (200)).
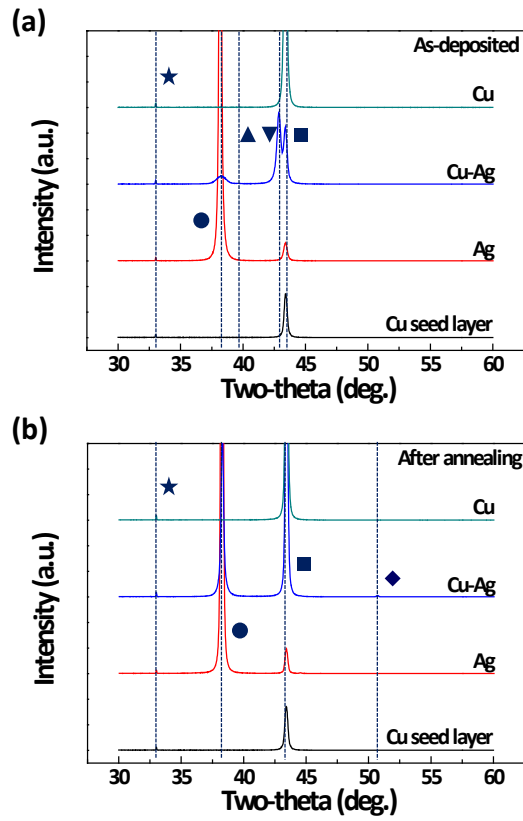
Fig. 14. XRD patterns of (a) as-deposited and (b) annealed Cu, Cu-Ag, and Ag films; with the normal intensity as the y-axis instead of log scale.
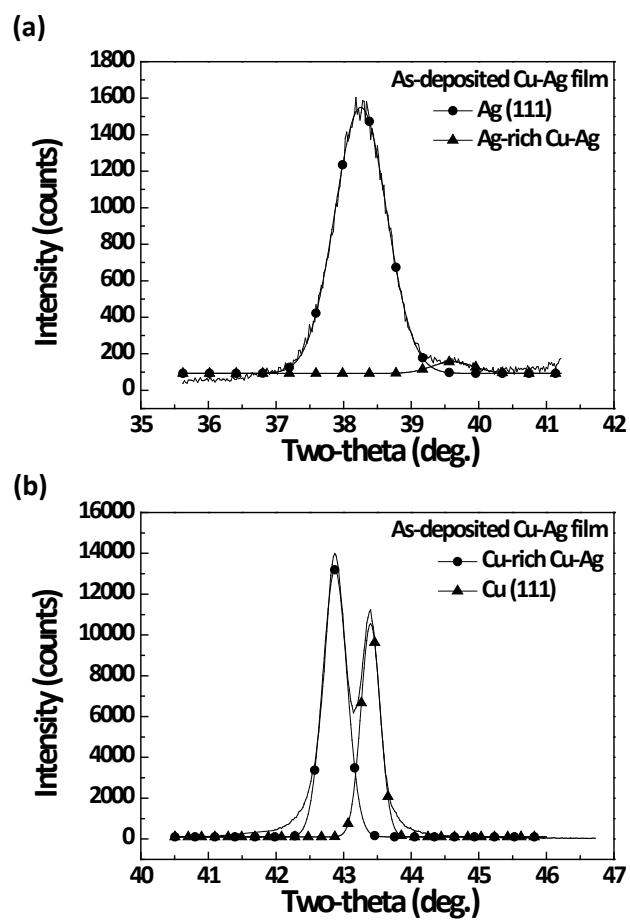
Fig. 15. The deconvolution of peaks corresponding to (a) pure Ag and Ag-rich Cu-Ag

and (b) pure Cu and Cu-rich Cu-Ag.
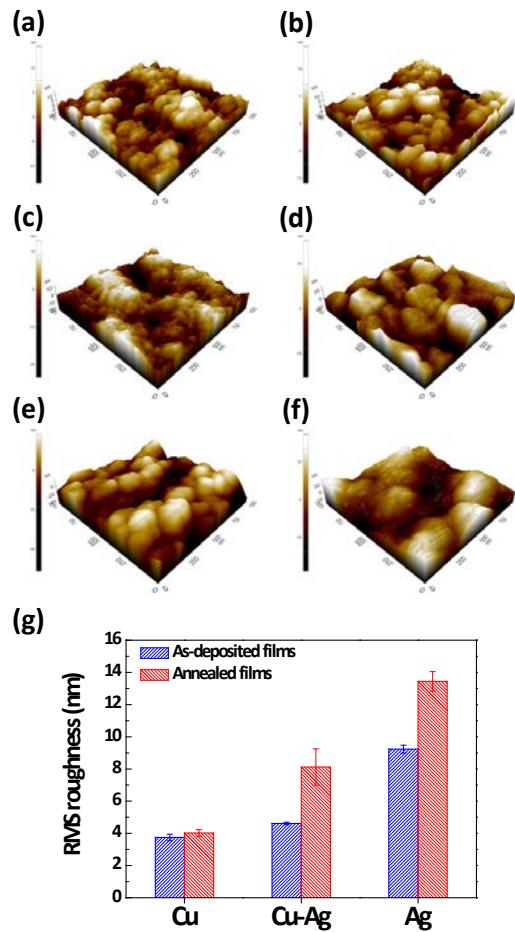
Fig. 16. Surface morphologies of (a) as-deposited and (b) annealed Cu, (c) as-deposited and (d) annealed Cu-Ag, (e) as-deposited and (f) annealed Ag, and (g) root-mean-square roughness.
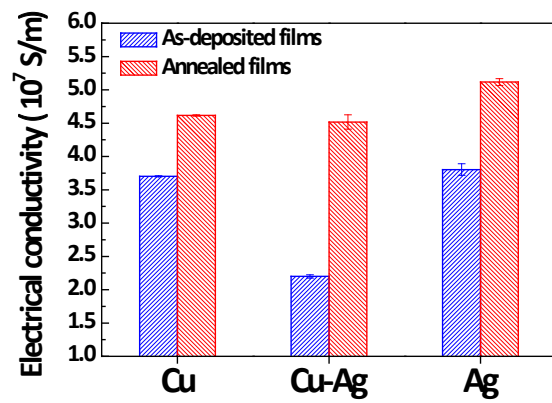
Fig. 17. Electrical conductivities of as-deposited and annealed Cu, Cu-Ag, and Ag films.
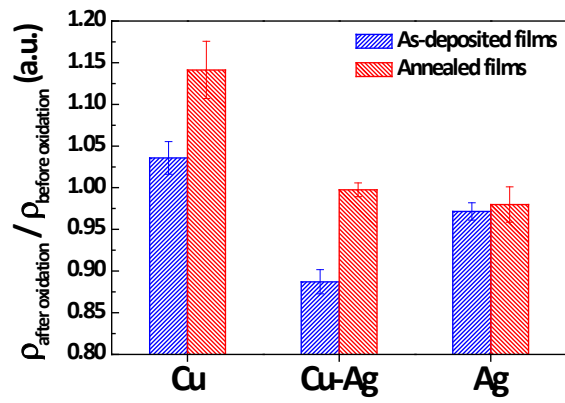
Fig. 18. Oxidation resistance of as-deposited and annealed Cu, Cu-Ag, and Ag films.

(a)

(b)
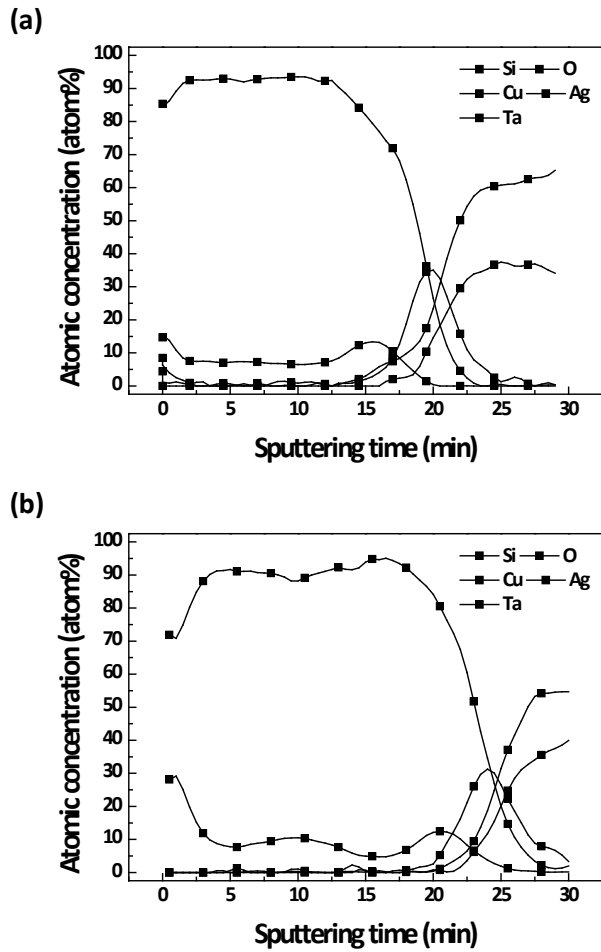
Fig. 19. The depth profiles of (a) as-deposited and (b) annealed Cu-Ag films measured

by AES. The sputtering rate was 16.2 nm/min with respect to SiO_2.
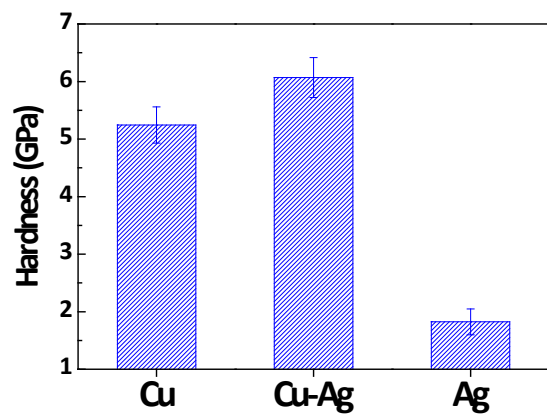
Fig. 20. The average hardness of as-deposited Cu, Cu-Ag, and Ag films.

IV. Conclusion

In summary, Cu-Ag superfilling for the fabrication of interconnection was successfully achieved by the electrodeposition. From the electrochemical analyses and the investigation on the atomic distribution of Cu and Ag, superfilling of Cu-Ag was clearly explained by CEAC model. Even though the acceleration was limited to Ag of which maximum atomic composition was only 17.9 atom%, the bimetallic superfilling was obtained. Regarding the fabrication of multifunctional nanostructures containing more than two metals, this research provides the one of strategies, which is the superfilling of previously patterned features. Using Damascene process and superfilling technique, the array of multifunctional materials can be easily achieved, that is, the targeted position of deposition can be accurately determined by the patterning of the desired substrates. In the aspect of Cu-Ag film properties, it was observed that Cu-Ag film exhibited superior oxidation resistance and mechanical hardness without severe reduction of electrical conductivity compared to pure Cu. Since the one of the current issues in the metal interconnection was the electromigration failure, therefore, Cu-Ag interconnection expected to be more resistive against the electromigration could be a candidate to solve this problem.

However, the environmental problem caused by using cyanide-based electrolyte still remains, therefore, the researches on the superfilling of Cu-Ag in the environmentally friendly electrolytes should be proceeded.

V. References

1. ITRS, International Technology Roadmap for Semiconductors, 2011, Interconnect.

2. H. L. Cho and J. G. Lee, *Mat. Res. Soc. Symp. Proc.*, **564**, 353 (1999).

3. W. Lee, H. Cho, B. Cho, J. Kim, Y. -S. Kim, W. -G. Jung, H. Kwon, J. Lee, P. J. Reucroft, C. Lee, and J. Lee, *J. Electrochem. Soc.*, **147**, 3066 (2000).

4. B. Zhao, H. Kim, and Y. Shimogaki, *Jpn. J. Appl. Phys.*, **44**, L1278 (2005).

5. B. Zhao, T. Momose, and Y. Shimogaki, *Jpn. J. Appl. Phys.*, **45**, L1296 (2006).

6. K. Barmak, A. Gungor, A. D. Rollett, C. Cabral Jr., and J. M. E. Harper, *Mat. Res. Soc. Symp. Proc.*, **721**, 51 (2002).

7. K. Barmak, A. Gungor, A. D. Rollett, C. Cabral Jr., and J. M. E. Harper, *Mater. Sci. Semicond. Process*, **6**, 175 (2003).

8. J. Lin and L. Meng, *J. Alloy. Compd.*, **454**, 150 (2008).

12. T. P. Moffat, B. Baker, D. Wheeler, J. E. Bonevich, M. Edelstein, D. R. Kelly, L. Gan, G. R. Stafford, P. J. Chen, W. F. Egelhoff, and D. Josell, *J. Electrochem. Soc.*, **149**, C423 (2002).

13. B. C. Baker, M. Freeman, B. Melnick, D. Wheeler, D. Josell, and T. P. Moffat, *J. Electrochem. Soc.*, **150**, C61 (2003).

14. E. J. Ahn and J. J. Kim, Electrochem. Solid-State Lett., 7, C118 (2004).

15. M. J. Kim, H. J. Lee, S. H. Yong, O. J. Kwon, S.-K. Kim, and J. J. Kim, J. Electrochem. Soc., 159, D253 (2012).

16. H. Huang, F. Spaepen, *Acta Mater.*, **48**, 3261 (2000).

17. K. Han, A. A. Vasquez, Y. Xin, and P. N. Kalu, *Acta Mater.*, **51**, 767 (2003).

18. F. Misják, P. B. Barna, A. L. Tóth, T. Ujvári, I. Bertóti, and G. Radnóczi, *Thin Solid Films*, **516**, 3931 (2008).

CURRICULUM VITAE
Myung Jun Kim

Electronics Processing Research Laboratory

School of Chemical and Biological Engineering

Seoul National University, Seoul 151-744, KOREA

Personal Information

Name:	Myung Jun Kim	
Date of Birth:	January 3, 1985	
Place of Birth:	Daegu, Korea	
Nationality:	Republic of Korea	
Sex:	Male	

Office Address

Institute of Chemical Processes

Seoul National University

San 56-1, Shillim-dong, Kwanak-gu

Seoul 151-744, Korea

Tel: +82-2-880-1576

E-mail: kmj4717@snu.ac.kr

EDUCATION

Doctor of Philosophy (March 2007 ~ present)

School of Chemical and Biological Engineering, Seoul National University

Advisor: Prof. Jae Jeong Kim

Thesis: "The influences of pulse and pulse-reverse electrodeposition on the properties of Cu thin films and superfilling for the fabrication of Cu interconnection"

Batchelor of Engineering (March 2003 ~ February 2007)

School of Chemical and Biological Engineering, Seoul National University

PROFESSIONAL ACTIVITIES

April 2007 ~ present   Member, Korea Institute of Chemical Engineering

2009~2010   Student Member, Material Research Society, USA

September 2008 ~ present   Student Member, The Electrochemical Society, USA

AWARDS

February 21, 2012   Cheil Industries-Seoul National University Collaboration
                     Award of Excellence

LIST OF PUBLICATIONS (Myung Jun Kim)

-International Journal-

[1] Myung Jun Kim, Sung Ki Cho, Hyo-Chol Koo, Taeho Lim, Kyung Ju Park, and Jae Jeong Kim, "Pulse Electrodeposition for Improving Electrical Properties of Cu Thin Film", J. Electrochem. Soc., 157, D564-D569 (2010).

[2] Sung Ki Cho, Myung Jun Kim, Taeho Lim, Oh Joong Kwon, and Jae Jeong Kim, "Deposit profiles characterized by the seed layer in Cu pulse-reverse plating on a patterned substrate", J. Vac. Sci. Technol. B, 29, 011004 (2011).

[3] Sung Ki Cho, Myung Jun Kim, and Jae Jeong Kim, "MSA as a Supporting Electrolyte in Copper Electroplating for Filling of Damascene Trenches and Through Silicon Vias", Electrochem. Solid-State Lett., 14, D52-D56 (2011).

[4] Taeho Lim, Hyo-Chol Koo, Kwang Hwan Kim, Kyung Ju Park, Myung Jun Kim, Oh Joong Kwon, and Jae Jeong Kim, "Room-Temperature Electroless Deposition of CoB Film and its Application as In Situ Capping during Buffing Process", Electrochem. Solid-State Lett., 14, D95-D98 (2011).

[5] Kyung Ju Park, Hyo-Chol Koo, Taeho Lim, Myung Jun Kim, Oh Joong Kwon, and Jae Jeong Kim, "Evaluation of Stability and Reactivity of Cu Electroless Deposition Solution by In Situ Transmittance Measurement", J. Electrochem. Soc., 158, D541-D545 (2011).

[6] Myung Jun Kim, Hyo June Lee, Sang Heon Yong, Oh Joong Kwon, Soo-Kil Kim, and Jae Jeong Kim, "Facile Formation of Cu-Ag Film by Electrodeposition for the Oxidation-Resistive Metal Interconnect", J. Electrochem. Soc., 159, D253-D259 (2012).

[7] Sung Ki Cho, Myung Jun Kim, Hyo-Chol Koo, Oh Joong Kwon, and Jae Jeong Kim, "Low-resistivity Cu film electrodeposited with 3-N,N-dimethylamonodithiocarbamoyl-1-propanesulfonate for the application to the interconnection of electronic devices", Thin Solid Films, 520, 2136-2141 (2012).

[8] Taeho Lim, Hyo-Chol Koo, Kyung Ju Park, Myung Jun Kim, Soo-Kil Kim, and Jae Jeong Kim, "Optimization of Catalyzing Process on Ta Substrate for Copper Electroless Deposition Using Electrochemical Method", J. Electrochem. Soc., 159, D142-D147 (2012).

[9] Kyung Ju Park, Myung Jun Kim, Taeho Lim, Hyo-Chol Koo, and Jae Jeong Kim, "Conformal Cu Seed Layer Formation by Electroless Deposition in Non-Bosch through Silicon Vias", Electrochem. Solid-State Lett., 15, D26-D28 (2012).

[10] Sung Ki Cho, Myung Jun Kim, Hyo-Chol Koo, Soo-Kil Kim, and Jae Jeong Kim, "An Empirical Relation between the Plating Process and Accelerator Coverage in Cu Superfilling", Bull. Korean Chem. Soc., 33, 1603-1607 (2012).

[11] Myung Jun Kim, Taeho Lim, Kyung Ju Park, Sung Ki Cho, Soo-Kil Kim, and Jae Jeong Kim, "Characteristics of Pulse-Reverse Electrodeposited Cu Thin Films I. Effects of the Anodic Step in the Absence of an Organic Additive", J. Electrochem. Soc., 159, D538-D543 (2012).

[12] Myung Jun Kim, Taeho Lim, Kyung Ju Park, Oh Joong Kwon, Soo-Kil Kim, and Jae Jeong Kim, "Characteristics of Pulse-Reverse Electrodeposited Cu Thin Films II. Effects of Organic Additives", J. Electrochem. Soc., 159, D544-D548 (2012).

[13] Myung Jun Kim, Sang Heon Yong, Hyun Seok Ko, Taeho Lim, Kyung Ju Park, Oh Joong Kwon, and Jae Jeong Kim, "Superfilling of Cu-Ag Using Electrodeposition in Cyanide-based Electrolyte", J. Electrochem. Soc., 159, D656-D658 (2012).

[14] Taeho Lim, Kyung Ju Park, Myung Jun Kim, Hyo-Chol Koo, and Jae Jeong Kim, "Real-time Observation of Cu Electroless Deposition Using OCP Measurement Assisted by QCM", J. Electrochem. Soc., 159, D724-D729 (2012).

[15] <u>Myung Jun Kim</u>, Kyung Ju Park, Taeho Lim, Seung Hoe Choe, Taekyung Yu, and Jae Jeong Kim, "One-Pot Synthesis of PdAu-Au Core-Shell Bimetallic Nanoparticles Using Electrodeposition ", J. Electrochem. Soc., 160, E1-E4 (2013).

[16] Seunghoe Choe, Myung Jun Kim, Hoe Chul Kim, Taeho Lim, Kyung Ju Park, Sung-Ki Cho, Soo-Kil Kim, and Jae Jeong Kim, "Seed Repair by Electrodeposition in Pyrophosphate Solution for Acid Cu Superfilling", J. Electrochem. Soc., submitted.

[17] <u>Myung Jun Kim</u>, Hoe Chul Kim, Soo-Hyun Kim, Seungmin Yeo, Oh Joong Kwon, and Jae Jeong Kim, "Direct electrodeposition of Cu on Ru-Al_2O_3 layer", in preparation.

[18] <u>Myung Jun Kim</u>, Kyung Ju Park, Taeho Lim, Oh Joong Kwon, and Jae Jeong Kim, "Fabrication of highly conductive and oxidation-resistive Cu-Ag interconnection using electrodeposition: the mechanism of superfilling and the properties of Cu-Ag film", in preparation.

[19] <u>Myung Jun Kim</u>, Taeho Lim, Kyung Ju Park, Soo-Kil Kim, and Jae Jeong Kim, "Pulse-reverse electrodeposition of Cu for metal interconnection: I. Effects of anodic steps on the competitive adsorption of the additives used for superfilling", in preparation.

[20] <u>Myung Jun Kim</u>, Taeho Lim, Kyung Ju Park, Soo-Kil Kim, and Jae Jeong Kim, "Pulse-reverse electrodeposition of Cu for metal interconnection: II. Enhancement of Cu superfilling and leveling", in preparation.

-Conference Proceedings-

(International)

[1] <u>Myung Jun Kim</u>, Sung Ki Cho, and Jae Jeong Kim, "Change in the film properties according to the various electroplating conditions", 214th Meeting of ECS, Hawaii, USA, October, 2008

[2] Jae Jeong Kim, Sung Ki Cho, Kyung Ju Park, <u>Myung Jun Kim</u>, and Hyo-Chol Koo, "Cu Filling in Through Silicon Via (TSV) using Electroless and Electroplating for 3D Interconnection", 215th Meeting of ECS, San Francisco, May, 2009

[3] <u>Myung Jun Kim</u>, Taeho Lim, Kyung Ju Park, Oh Joong Kwon, and Jae Jeong Kim, "Synthesis of Pd-Au Nanoalloys Using Electrodeposition", 218th Meeting of ECS, Las

Vegas, USA, October, 2010

[4] Hyo Jun Lee, <u>Myung Jun Kim</u>, Taeho Lim, Kyung Ju Park, Oh Joong Kwon, and Jae Jeong Kim, "Electrodeposition of Cu-Ag Film in Cyanide Based Electrolyte", 218th Meeting of ECS, Las Vegas, USA, October, 2010

[5] Taeho Lim, Kyung Ju Park, <u>Myung Jun Kim</u>, Oh Joong Kwon, and Jae Jeong Kim, "Investigation of Cu Electroless Deposition Mechanism by Open Circuit Potential", 220th Meeting of ECS, Boston, USA, October, 2011

[6] Sang Heon Yong, <u>Myung Jun Kim</u>, Jae Jeong Kim, Jun Young Park, and Oh Joong Kwon, "Investigation of Cu-Ag film electrodeposited in cyanide-based electrolyte", International Conference on Advanced Electromaterials (ICAE) 2011, Jeju, Korea, November, 2011

[7] <u>Myung Jun Kim</u>, Taeho Lim, Kyung Ju Park, and Jae Jeong Kim, "Pulse-reverse electrodeposition for improving the electrical property of Cu thin film", Gordon Research Conferences, Electrodeposition, Biddeford, University of New England, USA, July, 2012

[8] Kwang Hwan Kim, Taeho Lim, Kyung Ju Park, Hyo-Chol Koo, <u>Myung Jun Kim</u>, Oh Joong Kwon, and Jae Jeong Kim, "Cu Electroless Deposition on Ru Barrier", 222nd Meeting of ECS, Honolulu, USA, October, 2012

[9] Hyun Seok Ko, <u>Myung Jun Kim</u>, Jae Jeong Kim, and Oh Joong Kwon, "Fabrication of Cu-Ag Film Using Electrodeposition and Characterization of Its Properties", 222nd Meeting of ECS, Honolulu, USA, October, 2012

[10] Seunghoe Choe, <u>Myung Jun Kim</u>, Hoe Chul Kim, Taeho Lim, Anna Lee, Sang Hyun Jun, Kyung Nyung Woo, and Jae Jeong Kim, "Degradation of Additives and Its Influences on Copper Electrodeposition", 222nd Meeting of ECS, Honolulu, USA, October, 2012

[11] Kyung Ju Park, Taeho Lim, <u>Myung Jun Kim</u>, and Jae Jeong Kim, "Investigation of Reactions and Additive Effects in Electroless Deposition by In-Situ Transmittance Measurement", 222nd Meeting of ECS, Honolulu, USA, October, 2012

Translated into English

(domestic)

[12] <u>Myung Jun Kim</u>, Sung Ki Cho, and Jae Jeong Kim, "The Investigation on Cu electrodeposition for Cu damascene structure using direct and pulse current", 2008 Spring Meeting for Korean Institute of Chemical Engineers, April, 2008

[13] <u>Myung Jun Kim</u>, Sung Ki Cho, and Jae Jeong Kim, "Pulse electrodeposition for improving the properties of Cu thin films", 2009 Fall Meeting for Korean Institute of Chemical Engineers, October, 2009

[14] Kyung Ju Park, Taeho Lim, <u>Myung Jun Kim</u>, and Jae Jeong Kim, "Evaluation of Cu ELD solution using in situ transmittance measurement", 2010 Fall Meeting for Korean Institute of Chemical Engineers, October, 2010

[15] Taeho Lim, Hyo-Chol Koo, Kyung Ju Park, <u>Myung Jun Kim</u>, and Jae Jeong Kim, "Investigation of Copper Electroless Deposition Mechanism by Open Circuit Potential Measurement", The 18th Korean Conference on Semiconductors, February, 2011

[16] Kyung Ju Park, Hyo-Chol Koo, Taeho Lim, <u>Myung Jun Kim</u>, and Jae Jeong Kom, "in situ Transmittance Measurement for Monitoring of Solution Performance in Copper Electroless Deposition", The 18th Korean Conference on Semiconductors, February, 2011

[17] Seung Hoe Choe, <u>Myung Jun Kim</u>, Hoe Chul Kim, and Jae Jeong Kim, "Seed layer repairing in pyrophosphate-based electrolyte", 2011 Spring Meeting for Korean Institute of Chemical Engineers, April, 2011

[18] Taeho Lim, Kyung Ju Park, <u>Myung Jun Kim</u>, and Jae Jeong Kim, "Investigation of Cu Electroless Deposition Mechanism: Effect of Cu Oxide during Cu Electroless Deposition", 2011 Fall Meeting for Korean Institute of Chemical Engineers, October, 2011

[19] <u>Myung Jun Kim</u>, Taeho Lim, Kyung Ju Park, and Jae Jeong Kim, "The influences of the dissolution in pulse-reverse electrodeposition on the properties of Cu thin films", 2011 Fall Meeting for Korean Institute of Chemical Engineers, October, 2011

[20] Taeho Lim, Hyo-Chol Koo, Kyung Ju Park, <u>Myung Jun Kim</u>, Soo-Kil Kim, and Jae Jeong Kim, "Optimization of catalyzing process on Ta substrate for Copper electroless deposition using electrochemical method", The 19th Korean Conference on Semiconductors, February, 2012

[21] Kyung Ju Park, <u>Myung Jun Kim</u>, Taeho Lim, Hyo-Chol Koo, and Jae Jeong Kim,

"Conformal Cu seed layer formation by electroless deposition in high aspect ratio of non-bosch through silicon vias", The 19th Korean Conference on Semiconductors, February, 2012

[22] Hoe Chul Kim, Myung Jun Kim, Seung Hoe Choe, Taeho Lim, Kyung Ju Park, Kwang Hwan Kim, Hyeuk Jin Seo, Soo-Kil Kim, and Jae Jeong Kim, "Characteristics of electrodeposited Cu film with various additives", 2012 Spring Meeting for Korean Institute of Chemical Engineers, April, 2012

[23] Seunghoe Choe, Myung Jun Kim, Hoe Chul Kim, Oh Joong Kwon, and Jae Jeong Kim, "Direct electrodeposition and superfilling of Cu on Ru seed layer prepared by ALD", 2012 Fall Meeting for Korean Institute of Chemical Engineers, October, 2012

[24] Kwang Hwan Kim, Taeho Lim, Kyung Ju Park, Myung Jun Kim, and Jae Jeong Kim, "Cu electroless deposition in NH_2NH_2 based solution: Investigation of electrochemical behavior and Cu film growth phenomena", 2012 Fall Meeting for Korean Institute of Chemical Engineers, October, 2012

[25] Hoe Chul Kim, Myung Jun Kim, Seunghoe Choe, Hyeuk Jin Seo, Soo-Kil Kim, and Jae Jeong Kim, "Effects of benzotriazole and its derivatives on electrodeposited Cu film properties according to nitrogen atom numbers in azole group", 2012 Fall Meeting for Korean Institute of Chemical Engineers, October, 2012

-Patent-

Translated into English
(domestic)

[1] Jae Jeong Kim, Myung Jun Kim, and Oh Joong Kwon, "The fabrication method of Cu-Ag alloy coating and interconnection using electrodeposition", application number 10-2012-0052272